WASHINGTON UNIVERSITY

Department of Physics

Dissertation Examination Committee:
James H. Buckley, Chair
Ramanath Cowsik
Martin Israel
Henric Krawczynski
Demetrios Sarantites
Lee Sobotka

MULTI-WAVELENGTH OBSERVATIONS OF THE BLAZAR MARKARIAN 421

IN DECEMBER 2002 AND JANUARY 2003

by

Paul F. Rebillot, III

A dissertation presented to the
Graduate School of Arts and Sciences
of Washington University in
partial fulfillment of the
requirements for the degree
of Doctor of Philosophy

May 2006

Saint Louis, Missouri

UMI Number: 3223456

INFORMATION TO USERS

The quality of this reproduction is dependent upon the quality of the copy submitted. Broken or indistinct print, colored or poor quality illustrations and photographs, print bleed-through, substandard margins, and improper alignment can adversely affect reproduction.

In the unlikely event that the author did not send a complete manuscript and there are missing pages, these will be noted. Also, if unauthorized copyright material had to be removed, a note will indicate the deletion.

UMI®

UMI Microform 3223456

Copyright 2006 by ProQuest Information and Learning Company.

All rights reserved. This microform edition is protected against unauthorized copying under Title 17, United States Code.

Acknowledgements

I would first like to thank my advisor Jim Buckley, for all of his insight and encouragement through my graduate school career. I would like to thank Henric Krawczynski for his help in getting an article based on this work published in the Astrophysical journal. I would like to thank Dan Leopold, as well as Jim, for helping me to understand and enjoy experimental physics much more than I had before. I would also like to thank the members of my dissertation committee for many helpful comments on this text. I would also like to thank Trevor Weekes and the entire VERITAS collaboration. It has been an honor to work with all of you.

I would like to thank the entire high energy astrophysics group at Washington University, including Marty Israel, Bob Binns, Paul Hink, Michael Friedlander, Paul Downkontt, Garry Simburger, Marty Olevitch, Dana Braun, and Richard Bose. I would like to thank Julia Hamilton and Sarah Jordan for expert guidance through this dissertation process. I must, of course, thank my fellow students, who were always there to share a drink, or five. These include Lauren Scott, Karl Kosack, Chris Aubin, Scott Hughes, Jeremy Perkins, Brian Rauch, Kris Gutierrez, Vicki Lee,

ii

Trey Garson, Allyson Gibson, Qinghai Wang and many others.

I would like to thank Scott Hughes for reducing the X-ray data that is presented in this dissertation. I would also like to thank Margo and Hugh Aller, Paul Boltwood, Alberto Sadun, Daniel Kranich, and Aimo Sillanpaa for supplying optical, radio, and TeV γ-ray data that comprises this multi-wavelength campaign.

I had built up an incredible support network during my time at Washington University, and was grateful to share wonderful times with all of them. Among those are Kristin Huml, Jennifer Banks, Rose Martelli, Alison Stritzl, Danette Wilson, Amber Powers, Aaron Hock, and Diane Milligan. Whereever this group of "funhounds" were, a wonderful rendition of "Bye, Bye, Bye" or "Genie in a Bottle" was surely to be heard.

I would like to thank my family for all of their support, seeing as how I have been in school my entire adult life. My father Paul, my mother Patty, and my brother Ryan. A strong family bond has helped me my entire life, and I am sure I could not have done this without you all.

Lastly, I would like to thank my girlfriend, and love of my life, Amy Parker. From helping to proofread this thesis, to our weekly beer and hot wing date at Nick's pub, you have enriched my life in so many ways. With Newton, our crazy German Shepard, I know we will be enjoying many more great years to come.

Contents

v

List of Figures

List of Tables

Abstract

I report on a multiwavelength campaign on the TeV γ-ray blazar Markarian (Mrk) 421 performed during December 2002 and January 2003. These target of opportunity observations were initiated by the detection of X-ray and TeV γ-ray flares with the All Sky Monitor (ASM) on board the *Rossi X-ray Timing Explorer* (*RXTE*) and the 10 m Whipple γ-ray telescope. The campaign included observational coverage in the radio (University of Michigan Radio Astronomy Observatory), optical (Boltwood, La Palma KVA 0.6m, WIYN 0.9m), X-ray (RXTE pointed telescopes), and TeV γ-ray (Whipple and HEGRA) bands. At TeV energies, the observations revealed several flares at intermediate flux levels, peaking between 1 and 1.5 times the flux from the Crab Nebula. While the time averaged spectrum can be fitted with a single power law of photon index $\Gamma = 2.8$ from $dN_\gamma/dE \propto E^{-\Gamma}$, we find some evidence for spectral variability. Confirming earlier results, the campaign reveals a rather loose correlation between the X-ray and TeV γ-ray fluxes. In one case, a very strong X-ray flare is not accompanied by a comparable TeV γ-ray flare. I present a simple analysis of the data with a synchrotron-self Compton model, emphasizing that models with very high Doppler factors and low magnetic fields can describe the data.

This work is licensed under the Creative Commons Attribution-NonCommercial-ShareAlike2.5 License.

To view a copy of this license, visit

http://creativecommons.org/licenses/by-nc-sa/2.5/ or send a letter to

Creative Commons

543 Howard Street, 5th Floor

San Francisco, California, 94105, USA.

Chapter 1

Introduction

The *Compton Gamma-Ray Observatory*, launched in 1991, first showed that the production of high energy γ-rays ($E > 100\text{MeV}$) is a ubiquitous phenomenon in the Universe (Hartman et al., 1992). Around the same time, ground-based γ-ray observatories made the first high-confidence detections of very high energy TeV (VHE) γ-rays from the Crab Nebula and from Mrk421, opening up a new electro-magnetic window. The earth's atmosphere is opaque to radiation in this spectral window, absorbing high energy photons, and not allowing their propagation to sea level. Satellite experiments circumvent this obstacle by making measurements above the atmosphere; ground based γ-ray astronomy turns this apparent obstacle into the primary method for detection of γ-rays . New experiments such as HESS and MAGIC, together with the Whipple 10 m telescope, have now detected ~ 15 sources of $> 300\text{GeV}$ γ-rays . The sources of this VHE radiation are the energetic nonthermal sources in the universe. To date TeV emission has been seen in supernova remnants, pulsar powered

1

nebula, the galactic center and a number of Active Galactic Nuclei (AGN).

AGNs are young galaxies in which the majority of the luminosity originates from the *central engine*, widely believed to be a $\sim 10^{6-10}$ solar mass black hole. Disks form along the equator of the central engine accretion, due to interstellar matter spiralling into the black hole. Jets form along the central engine's spin axis, which focus much of the energy into narrow cones of highly relativistic plasma outflows. It is believed that the accretion process occurring in the disk powers the formation of the highly relativistic jets. Both the jet and the accretion disk emit broadband nonthermal radiation at all wavelengths, as well as thermal emission. Emission and absorption lines in the thermal emission can be seen; they are either broad or narrow depending on their proximity to the central engine and the extent of Doppler broadening.

While it was originally thought that these different emission characteristics arose from physically different types of AGNs, the current widely held belief (Urry, 2004) is that all AGNs are more or less similar in structure, and that observed differences are due to values of certain fundamental parameters, and the orientation of the AGN with respect to an observer.

1.0.1 Classification and Unification of AGNs

The zoo of different young active galaxies can be related under the framework of this AGN unification paradigm. Examples include quasars, Seyfert galaxies, flat spectrum radio quasars, quasi-stellar objects (QSOs), and blazars, among others. One main

2

classification scheme is to sort objects based on the ratio of flux in radio bands (F_r)
to flux in the optical band (F_o). .If $\log(F_r/F_o) < 1$, an AGN is radio quiet. If the
ratio is larger than one, it is radio loud. Both radio quiet and radio loud AGN can
be broken down into further classifications.

Radio Loud AGNs - Seyfert Galaxies

Radio loud AGNs, also known as Seyfert galaxies, can be broken into two classes
- type I (Sy I) and type II (Sy II). Both types of Seyfert galaxies are believed to be
the same type of object, differing only in the viewing angle of the observer. Kinney
et al. (2000) have shown that this observational classification can be described in the
context of the geometrical placement of an observer compared to the jet axis of the
Seyfert galaxy. It is believed that type II Seyferts result from a viewing angle with
respect to the jet that is large. This results in the observer viewing through the torus,
and the broad line emission region. Conversely, type I Seyferts have small viewing
angles with respect to the jet axis. An observer will not be viewing through the disk,
and will see more radiation from the jet.

Radio Quiet AGNs - FRI and FRII Galaxies, and Blazars

In the same way that type I and type II Seyfert galaxies are related to each other by
viewing angle, Blazars and FRI and FRII radio galaxies are as well (Veilleux, 2003).
Blazars show non-thermal radiation up to TeV energies, due to a small viewing angle
with respect to the jet axis. FRI and FRII galaxies are similar objects, though the

3

viewing angle of an observer is normal to the jet axis. A further classification can be made in the blazar family between quasars, and BL Lac objects. Quasars exhibit flat radio spectra with $S_{\nu} \propto \nu^{0.5}$, as well as emission lines. In addition to the flat spectra, BL Lac objects exhibit a high degree of linear polarization in their radiation (up to 3%), as well as strong variability, along with the absence of strong emission lines (Impey, 1996).

Blazars - BL Lac Objects

Blazars are powerful sources across the electromagnetic spectrum. Typical spectral energy distributions (SEDs) for the high energy peaked TeV blazars show two broad peaks, one from infrared to X-ray energies and the other from X-ray to γ-ray energies. The low-energy peak is commonly believed to originate as synchrotron emission from a population of relativistic electrons gyrating in the magnetic field of the jet plasma. The origin of the high-energy peak is unknown. The best studied models assume that the γ-rays are produced in inverse Compton processes by the same electrons that emit the synchrotron radiation at longer wavelengths (a recent review can be found in Krawczynski (2004)). In so-called hadronic models, γ-rays are emitted as synchrotron radiation of extremely energetic protons (Aharonian, 2000; Mücke et al., 2003), as inverse Compton and synchrotron emission from a Proton Induced Cascade (PIC) (Mannheim, 1998), or from $\pi^0 \rightarrow \gamma\gamma$ decays following the interaction of high energy protons with some target material (Pohl and Schlickeiser, 2000).

4

The space-borne EGRET *(Energetic Gamma Ray Experiment Telescope)* detector on board the *Compton Gamma-Ray Observatory* discovered strong MeV and GeV γ-ray emission from 66 blazars, mainly from Flat Spectrum Radio Quasars and Unidentified Flat Spectrum Radio Sources (Hartman et al., 1992, 1999). Ground-based Cherenkov telescopes discovered TeV γ-ray emission from seven blazars, five of which were not detected by EGRET (Horan and Weekes, 2004; Aharonian et al., 2005). Although γ-ray emission from blazars has been studied for more than a decade now, it is still unclear where and how the emission originates. According to the most common paradigm, the emission originates close to a mass-accreting supermassive black hole, in a relativistically moving collimated plasma outflow (jet) that is aligned with the line of sight to within a few degrees. The relativistic Doppler effect can explain the intensity of the blazar emission and its rapid variability at X-ray and γ-ray energies on hour time scales, because, since the apparent luminosity scales approximately as the fourth power of the relativistic Doppler factor [1] δ_j, and the observed flux variability timescale is inversely proportional to δ_j.

---

[1] The relativistic Doppler factor is given by $\delta_j = [\Gamma(1 - \beta \cos\theta)]^{-1}$ with Γ, the bulk Lorentz factor of the jet plasma, θ, the angle between jet axis and the line of sight, and β, the plasma velocity, in units of the speed of light.

1.1   A Brief History of Time with Atmospheric Cherenkov Telescopes

Very high energy ground based γ-ray astronomy, as a field, originated in the "heroic era " (Weekes, 1992). The mid 1960s saw the realization that instruments similar to cosmic-ray detectors could be used to detect γ-rays using a similar method that they use to detect cosmic rays. Indeed, the initial motivation for looking for γ-ray sources in the sky was driven by the hope that they would find the acceleration source of cosmic rays. These groups continued their work through the 1970s into the 1980s, where possible γ-ray detections were reported for the X-ray binaries Cygnus X-3 (Samorski and Stamm, 1983; Lloyd-Evans et al., 1983) (using the German experiments), as well as Her X-1 (with the Haverah Park array as well as Whipple) (Dingus et al., 1988; Gorham et al., 1986). Other groups, such as the Crimean group as well as the Whipple group reported detection of Cygnus X-3 as well (Aharonian, 2004).

These X-ray binaries that were reported as detections during the 1980s were not thought previously as being able to produce very high energy radiation. As more observations of Cygnus X-3 were taken, the significance of the result decreased. This, coupled with the knowledge that the original detection was only a few sigma above background resulted in the conclusion that Cygnus X-3 was a false identification (Aharonian, 2004).

6

While this false detection of Cygnus X-3 was an unfortunate event in the early history of the atmospheric Cherenkov technique, it pointed to the need for better techniques to separate background from signal. The key to this was the imaging technique for Cherenkov telescopes (Hillas, 1985), and the detection of the standard candle of γ-ray astronomy, the Crab Nebula. The discovery of a steady source of high energy γ-rays , along with the increased signal to noise ratio associated with the imaging technique were the real keys to establishing high energy γ-ray astronomy as a viable field.

1.2   Overview of Dissertation

In this dissertation I present results from a multi-wavelength campaign on the TeV blazar Markarian (Mrk) 421. The source is a nearby (z = 0.031) high energy-peaked BL Lac object, and was the first extragalactic source detected in the TeV γ-ray band (Punch et al., 1992).Correlated X-ray and TeV γ-ray emission has been seen in a number of multi-wavelength campaigns (Buckley et al., 1996; Maraschi et al., 1999), but the observations have typically under-sampled the short variability timescales. In November 2002, γ-ray observations with the Whipple 10 m telescope revealed several Mrk 421 flares with fluxes exceeding three times the steady flux from the Crab Nebula. The All Sky Monitor instrument aboard *RXTE* also showed extremely strong 2-12 keV fluxes reaching 100 milli-Crab. Collectively these triggered a coordinated campaign. Krawczynski et al. invoked radio, optical, and X-Ray

(*RXTE*) observations to commence as soon as the waning Moon would allow the Cherenkov telescope to take data once more. Although the X-ray and TeV γ-ray fluxes had decreased substantially when the campaign started on December 4th, we acquired simultaneous SED snapshots for a wide range of X-ray and TeV γ-ray flux levels.

In chapter 2, I present an overview of the atmospheric Cherenkov technique that is used to detect TeV γ-rays from ground based detectors. In chapter 3, I present the results of the multi-wavelength campaign, including lightcurve, spectra, and timing and correlation analysis. In chapter 4, I present some modeling of the multi-wavelength spectra, in the context of a synchrotron self Compton emission model.

Chapter 2

Experimental Technique

2.1 Ground Based γ-ray Astronomy

To develop a multi-wavelength view of the universe, astronomers must battle the opacity of the atmosphere to certain frequencies of electromagnetic radiation. The low-frequency limit for ground based observations is roughly 15 MHz, arising from free-electron absorption in the upper atmosphere starting at the plasma frequency (Rohlfs and Wilson, 2004),

$$\nu_p = 8.97 \sqrt{\frac{N_e}{cm^{-3}}} \ KHz \ . \tag{2.1}$$

The high frequency cutoff for the radio regime occurs at around 1300 GHz, and is due to absorption through the molecular degrees of freedom of molecules, particularly water and diatomic oxygen.

Similar obstructions to electromagnetic radiation occur in the infrared (also due to molecular absorption), and throughout the ultra-violet, X-ray, and γ-ray regimes, leaving narrow windows in the optical and radio wavebands. To overcome these barriers to observation, astronomers must place their detection equipment above the atmosphere. For the infrared and UV regimes, this has been accomplished with space-based telescopes such as IRAS, IUE, EUVE, the Hubble Space Telescope (optical) and the Spitzer Space Telescope (infrared). This method has also been essential in the X-ray regime (e.g., for HEAO, ROSAT, XMM-Newton, Chandra, and RXTE) as well as the γ-ray regime (with COS-B, and the EGRET, OSSE, and Comptel telescopes aboard the Compton Gamma Ray Observatory, as well as INTEGRAL and recently Swift). With X-ray and γ-ray space-borne telescopes, however, another set of limitations arise since the physical size that is possible for a space-borne instrument is limited to an effective area of $\leq 1\text{m}^2$ and limited stopping distance (a few radiation lengths). In the γ-ray regime, this places an upper limit on the energy that can be detected by a particular instrument. Take, for example, the EGRET instrument, which detected γ-rays by pair production inside spark chambers. The EGRET instrument was about 2m in height, and contained eight radiation lengths of spark chambers. This resulted in an energy measurement upper limit of 30 GeV[1] . Higher energy upper limits require more radiation lengths for the γ-ray to traverse, and therefore a larger or heavier instrument is required. At the same time, sparse statistics at

---

[1] This energy as also limited by the self-vetoing due to "back-splash" events in the calorimeter that triggered the anti-coincidence shields.

10

high energies require larger effective areas. However, current launch vehicles limit the maximum area to $\leq 1m^2$.

The natural opaqueness of our atmosphere to γ-rays can be used to our benefit. The atmospheric Cherenkov approach uses the atmosphere as a giant total-absorption calorimeter, causing pair production of incoming high energy γ-rays , and subsequent electromagnetic showers. The electrons and positrons in these showers will then produce optical Cherenkov radiation in the atmosphere, which can make it to a ground-level telescope. Blackett (1949) was the first to suggest that Cherenkov light from particles hitting the atmosphere contribute to the background light of the night sky (Blackett, 1949). The first experimental verification of this hypothesis was performed by Galbraith and Jelley (1953, 1955), who demonstrated coincidences in the signals detected by a pair of simple searchlight-PMT telescopes, due to cosmic-ray interactions with the earth's atmosphere. This method was first proposed to detect γ-rays by detecting the Cherenkov light that they (indirectly) produce by Chudakov et al. (1962). Turver and Weekes (1981), and later Hillas (1985) proposed refinements in the technique making use of parameters of the shower images to distinguish γ-rays from the large background of cosmic-rays.

This method to detect high energy γ-rays is employed at the Whipple 10m telescope, located on Mt. Hopkins in southern Arizona. Located at an altitude of about 2.1 km, the telescope employs a 10m optical reflector and 390 photo-multiplier pixels to detect these short flashes of light. Figure 2.1 is a picture of the Whipple 10m tele-

scope. The Whipple group, under the direction of CfA astrophysicist Trevor Weekes, made the first high-confidence detection of a galactic source (the Crab Nebula), and an extragalactic source (Mrk421), proving the power of the imaging technique and launching a new branch of astronomy.

Subsequent experiments have used the atmospheric Cherenkov technique in a stereoscopic mode, where multiple telescopes are used to image an air shower. The HEGRA experiment (Mirzoyan et al., 1994) demonstrated the power of this technique, while so-called "next-generation" instruments - HESS (Hinton, 2004), VERITAS (Weekes et al., 2002), and CANGAROO-III (Kubo et al., 2004) utilize this stereoscopic technique, while using larger telescopes.

2.1.1   Particle Air Showers of Photons and Hadrons

Photon Interactions at the Top of the Atmosphere

When photons with energies greater than $2m_ec^2$ (1.022 MeV) enter the atmosphere, they are able to produce electron positron pairs. The cross section for pair production is proportional to the free-electron scattering Thomson cross section, with relativistic corrections and corrections due to screening by the Coulomb field of the nucleus. It can be shown that the cross section for interaction for photons with energies in our energy range is (Ramana Murthy and Wolfendale, 1986):

$$\sigma_{pair} = \alpha r_e^2 Z^2 \left[\frac{28}{9} ln \left(\frac{189}{Z^{1/3}} \right) - \frac{2}{27} \right] . \tag{2.2}$$
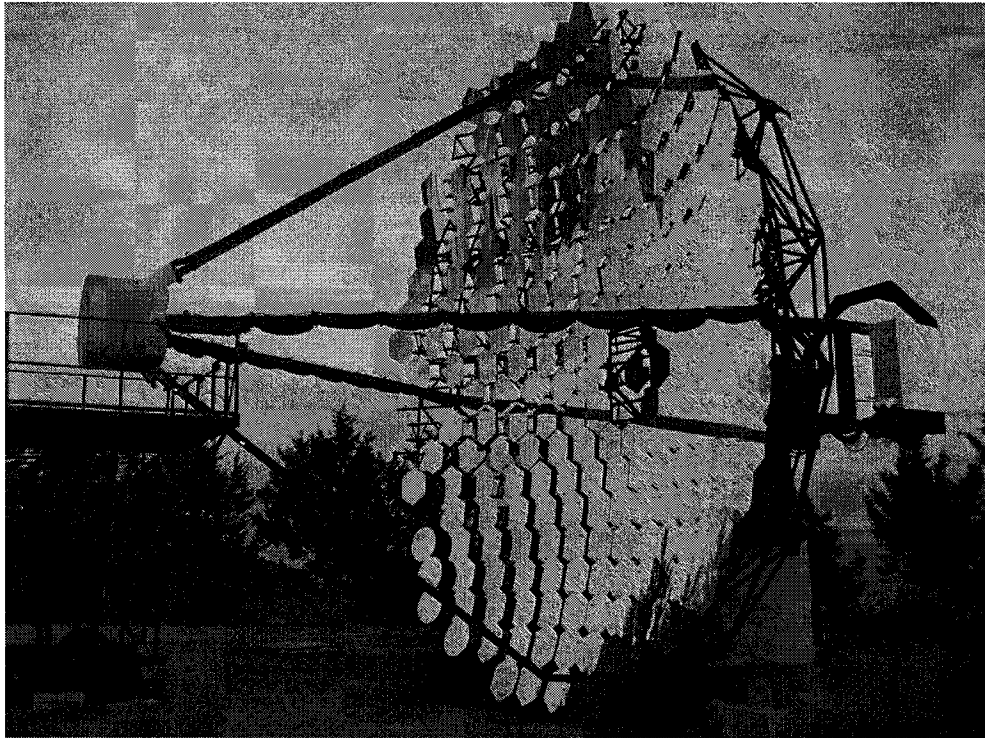
Figure 2.1: A photo of the Whipple 10m telescope.

In the case of a photon entering the atmosphere, the path length is inversely proportional to this cross-section, and is given by (Weekes, 2003)

$$\lambda_{pp} = \frac{1}{n\sigma_{pair}} \ , \tag{2.3}$$

where n is the number density of material the photon is passing through. We can also define a radiation length for a given particle passing through a given material with mass density ρ,

$$X = \frac{\rho}{n\sigma_{pair}} \ . \tag{2.4}$$

Typical γ-rays will pass through about 1 radiation length (or about 37 $\mathrm{g\,cm^{-2}}$) of atmosphere before pair producing, corresponding to an altitude of 20 km, for a standard atmospheric model with $\rho = \rho_0 \exp^{-z/h_0}$ with $\rho_0 = 1.35\,\mathrm{kg\,m^{-3}}$ and $h_0 = 7.25\,\mathrm{km}$ (Weekes, 2003).

If the primary γ-ray photons have energies much greater than twice the rest mass of the electron, the resulting electron-positron pair will each have sufficient energy to undergo a bremsstrahlung interaction, emitting another high energy photon. If energetic enough, this photon can once again undergo pair production. This sequence is known as an electromagnetic shower, and gives rise to a doubling in the number of particles (photons or electrons) after each radiation length (see, e.g. Longair (1992)). A rough schematic such a shower is given in Figure 2.2.

A high energy photon with energy E enters the atmosphere, and pair produces within roughly one radiation length X, defined in equation 2.4. Each resulting particle

14
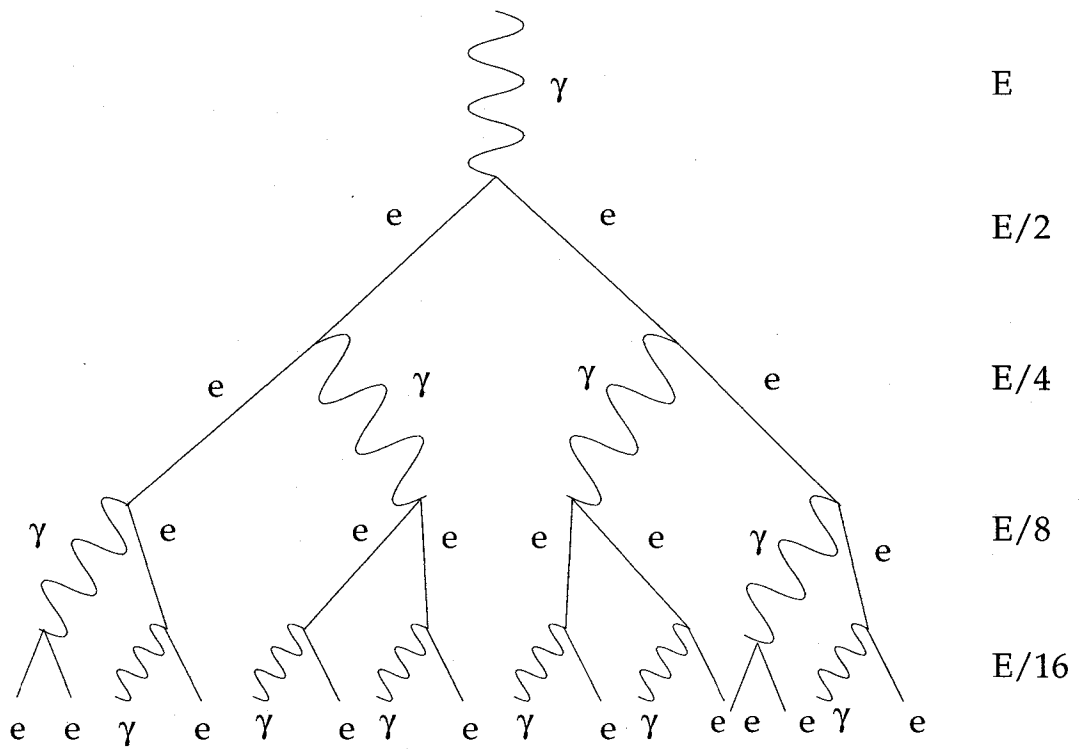
Figure 2.2: A simplified view of an electromagnetic shower. The energy at each level is the average energy per particle.

now has energy E/2, and will undergo bremsstrahlung radiation, giving off an additional photon after traversing, on average, one radiation length. The average energy of each particle at this stage is now E/4. This process will continue, with photons undergoing pair production, and electrons (and positrons) undergoing bremsstrahlung radiation. It can be seen that after n steps, the average energy per particle will be $E/2^n$. This electromagnetic cascade will cease when the average energy per particle is less than some critical energy E_c. Below this energy, it is ionization loss, not bremsstrahlung radiation, that is the the dominant energy loss process for electrons, causing electrons to lose all of their energy to ionization in a distance less than one radiation length. These two effects, when coupled together, imply that the shower will reach maximum size (number of particles, both photons and electrons) at this critical energy. A corollary is that since all showers will grow in size until the average energy is E_c, initial photons with larger starting energies will produce larger showers. These types of showers are compact in diameter, due to the relativistic beaming involved. For a γ-ray of energy 1 GeV, the average angle between the incident photon and the first produced electron positron pair is 0.2° (Weekes, 2003). Subsequently, the spread in an electromagnetic shower is dominated by multiple Coulomb scattering of secondary electrons.

Cosmic-Ray Nuclei Interactions at the Top of the Atmosphere

Much like incident photons described in the previous section, cosmic-ray nuclei incident in the atmosphere will also initiate particle cascades. These initial cosmic

16

rays produce showers with 3 main features (Longair, 1992):

- The primary cosmic ray will fragment into smaller nuclei, charged pions, and neutral pions. This fragmentation will continue until the energy per particle is below that required for pion production, about 1 GeV. The pions can be emitted with large transverse momentum, giving rise to broader showers.

- neutral pions will decay into 2 γ-rays , $\pi^0 \rightarrow 2\gamma$. These γ-rays will initiate electromagnetic cascades.

- charged pions will decay to muons, $\pi^+ \rightarrow \mu^+ + \nu_\mu$ and $\pi^- \rightarrow \mu^- + \bar{\nu}_\mu$ Low energy muons will decay into electrons, while high energy muons can reach the ground. These high energy muons reach the ground because their decay time to electrons is time dilated, due to their large Lorentz factors. It can be shown that muons with Lorentz factors greater than about 20 (corresponding to energies of 2 GeV) will reach the ground.

These nucleonic showers tend to cover a larger area. Both the lateral distribution and angular distribution of hadronic showers appear to be "splotchy", since they are composed of a number of electromagnetic sub-showers (from each π^0) and by rings from penetrating muons. This is also due to the fact that in the collision and subsequent fragmentations, protons inside the nucleus are in fact not point particles like electrons, but made up of quarks. An example of this type of shower is given in Figure 2.3.

17
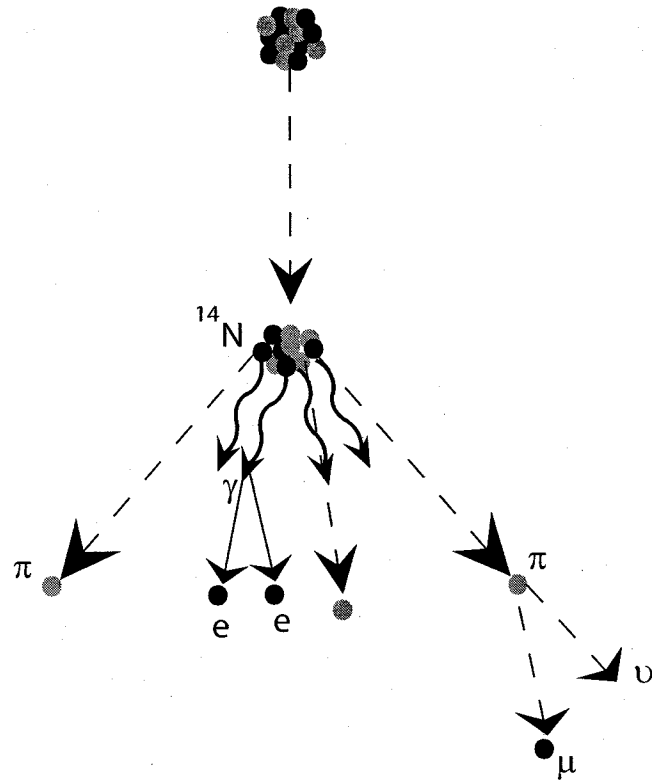
Figure 2.3: A simplified view of a nucleonic shower (Adapted from Bernlohr (2005))

2.1.2 Cherenkov Radiation

Both the electromagnetic and nucleonic cascades result in the production of a number of energetic charged particles. These charged particles, when traveling faster than the speed of light in air, will emit Cherenkov radiation. The essential features of this process (adapted from Jackson (1998)) are presented. A charged particle moving with a velocity v and charge e can be represented as a current

$$\vec{J} = ev\delta\left(x - vt\right)\delta(y)\delta(z)\hat{x} \ , \tag{2.5}$$

where $\hat{x}$ is the direction in which the electron is moving. To solve for the resulting electromagnetic fields we first take the Fourier transform of the current,

$$\vec{J}(\omega) = \frac{e}{\sqrt{2\pi}}\delta(y)\delta(z)e^{i\omega x/v}\hat{x} \ . \tag{2.6}$$

Substituting equation 2.6 into the solution for the retarded potentials, one can determine the radiated field and the Poynting flux ncE^2. Integrating over a sphere at a large distance r to find power radiated to infinity one obtains the usual result,

$$U = \int_0^\infty \int_\Omega \frac{n\sin^2\theta}{8\pi^2\epsilon_0 c^3} \left| \int \left[\dot{\vec{J}}(\omega) \right] d\vec{r} \right|^2 d\Omega d\omega \ . \tag{2.7}$$

If we now evaluate the integrand for the specific case of a charged particle moving uniformly (equation 2.6) we obtain

$$\left| \int \left[\dot{\vec{J}}(\omega) \right] d\vec{r} \right| = \left| \frac{\omega e}{\sqrt{2\pi}} \int_0^\infty \exp\left[ikx + \frac{i\omega x}{v} \right] dx \right| \ . \tag{2.8}$$

The exponent in equation 2.8 is always greater than zero for the free space dispersion relation $\omega = ck$. Therefore the integral of the oscillatory function ($\exp^{ikx}$) goes to zero,

19

resulting in no radiation in vacuum. In dispersive media, however, where $\omega = ck/n$, and $\cos\theta = -c/nv$ the exponent is zero, and the integral does not vanish. The angle $\theta_C \equiv \cos^{-1}(1/\beta n)$ is called the Cherenkov angle - it defines a Cherenkov cone of radiation, very similar to a shock front. By measuring θ_C, one can determine the velocity of the radiating particle. When we perform the integral in equation 2.7, we find that the energy radiated per unit frequency interval is

$$I(\omega) = \frac{\omega e^2 v}{4\pi\epsilon_0 c^3}\left(1 - \frac{c^2}{n^2 v^2}\right) . \tag{2.9}$$

Note that the intensity of Cherenkov radiation increases with frequency, and therefore decreases with wavelength. For particles passing through air, the Cherenkov radiation has a maximum intensity in the UV/Blue region of the visible spectrum, but is cut off by atmospheric absorption in the UV. Physically, this process can be viewed as the result of the time varying polarization of the medium, whereby the oscillating dipoles in the earth's atmosphere produce radiation that constructively interferes at a specific angle θ_C. Alternatively, one can view the process as an electromagnetic shock wave, like a "sonic boom". Figure 2.4 shows a pictorial example of this Cherenkov shock front.

To calculate the Cherenkov angle for a shock front, one must know the speed of the particle and the index of refraction for the medium it is passing through. For air at sea level, $n = 1.00029$. For a 0.50 GeV electron, the Cherenkov angle is $\theta \sim 1.4°$. The radiation propagates perpendicular to this conical shock front. For $\gamma \equiv \sqrt{1-\beta^2}^{-1} \gg \gamma_0$, the Cherenkov radiation is beamed in the forward direction

20
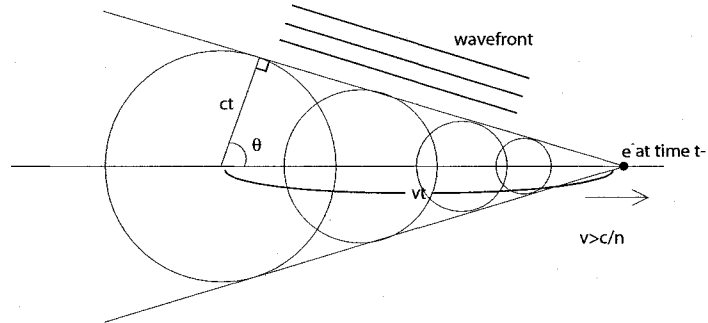
Figure 2.4: A cartoon describing the shock cone produced by Cherenkov radiation (Adapted from Longair (1992))

with angle

$$\sin^2 \theta_C = \left(\frac{1}{\gamma_0^2} - \frac{1}{\gamma^2}\right) .$$

(2.10)

Pulses of Cherenkov radiation due to particle showers in air are typically vary narrow, with a width between 8 and 10 nanoseconds. The Cherenkov light pulses are characterized by a fast rise and a long decay, and can be empirically described by the function

$$F(t) \simeq t^{1/2} e^{-\frac{2t}{t_0}} ,$$

(2.11)

where t_0 is the width of the Cherenkov light pulse.

21

2.1.3   Detection of Cherenkov Radiation by Ground-Based Telescopes

This thesis describes data collected with the Whipple imaging Atmospheric Cherenkov Telescope. Here I describe how this instrument detects and characterizes the Cherenkov radiation produced by electromagnetic showers from γ-rays and cosmic-rays. The main region of Cherenkov emission for electromagnetic showers will coincide with the region of maximum shower development; that is, the region that has the largest density of charged particles with velocities greater than c/n. Figure 2.5 shows this region for the electromagnetic shower from a 1 TeV γ-ray . Proton (or more generally cosmic-ray) induced showers can be viewed as a collection of such electromagnetic showers produced by the π^0-decay γ-rays .

It is apparent from Figure 2.5 that the emitted light from a proton-initiated shower covers more than 11 times the area than a γ-ray shower of similar energy. This fact will provide a basic clue on how to differentiate γ-ray showers from proton showers on the ground. Protons and cosmic-ray initiated showers are also $\sim 10^3$ more abundant than their γ-ray counterparts. Therefore, being able to discriminate a γ-ray from the enormous background of cosmic-rays is one of the primary concerns of the work presented here.
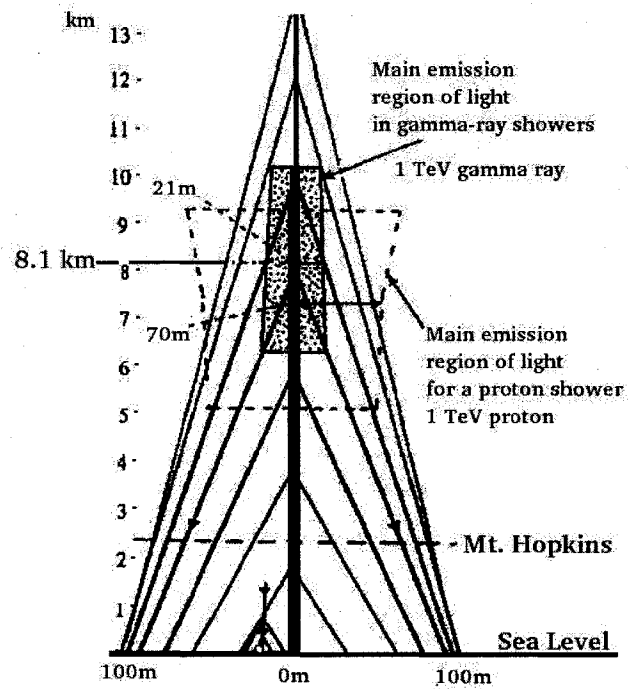
Figure 2.5: A cartoon describing a typical Cherenkov light pool generated by an air shower (Figure taken from Weekes (2003)).

Signal to Noise properties of the Atmospheric Cherenkov Technique

Apart from identifying γ-ray showers from the predominant cosmic-ray background, a γ-ray telescope must have a sufficient signal to noise ratio (SNR) in order to detect these faint Cherenkov light pulses against the night sky background (NSB) light. To accomplish this, an atmospheric Cherenkov Telescope (ACT) must consist of a very large optical light collector, a camera to image the showers, and fast electronics to digitize the Cherenkov pulses. The latter is of prime importance, since typical Cherenkov light pulses are $\sim 8 - 10$ns in length. The signal seen from a typical Cherenkov light pulse is (Weekes, 2003)

$$S = \int_{-\infty}^{+\infty} C(\lambda)\eta(\lambda)Ad\lambda \ .$$ (2.12)

Here $C(\lambda)$ is the flux of Cherenkov light, as a function of wavelength, $\eta(\lambda)$ is a combination of the quantum efficiency of the detecting device and the mirror reflectivity (also a function of wavelength), and A is the mirror collection area. These Cherenkov light pulses must be measured against a background of night sky light. This background (due to stars, airglow, city light, etc.) is

$$B = \int_{-\infty}^{+\infty} B(\lambda)\eta(\lambda)\tau A\Omega d\lambda \ .$$ (2.13)

Here, $B(\lambda)$ is the spectrum of background light, τ is the integration time of the electronics, and Ω is the solid angle subtended by the pixels in the camera of the telescope. The amount of background light seen should increase with both observing time (τ) and over how much area one is looking (Ω). If we assume that the background

24

light B is related to the noise by $N = \sqrt{B}$, the signal to noise ratio is

$$\frac{S}{\sqrt{B}} = \int_{-\infty}^{+\infty} C(\lambda) \sqrt{\frac{\eta(\lambda)A}{\Omega B(\lambda)\tau}} d\lambda \; . \tag{2.14}$$

In the design of ACTs, equation 2.14 implies that for the largest possible signal to noise ratio, we require an instrument of large light collecting diameter, with high efficiency low-noise light detectors, and with fast data acquisition electronics. Present day ACTs are single optical telescopes with diameters in the range 10-12m. Cameras are typically composed of 100 - 1000 photomultipliers with bialkali photocathodes covering a $3 - 5°$ field of view. Higher efficiency detectors are currently being developed. Typical detectors today have efficiencies of $\sim 25\%$ in the wavelength range 300-400 nm, while these new detectors promise efficiencies of more than 40% (Leopold et al., 2005).

Hillas Parametrization of Cherenkov Air Showers

Hillas (1985) first suggested that γ-ray air showers could be differentiated from cosmic-ray showers by imaging the Cherenkov light that arrived at the ground, and then performing a moment analysis on the light pool to describe its properties.

Figure 2.6 shows a γ-ray image with the geometric meaning of the parameters indicated on the diagram. Most γ-ray -like images can be parameterized under the assumption that they are shaped like ellipses. The parameters of the ellipse can be characterized by the first moments of the distribution (image centroid), the second
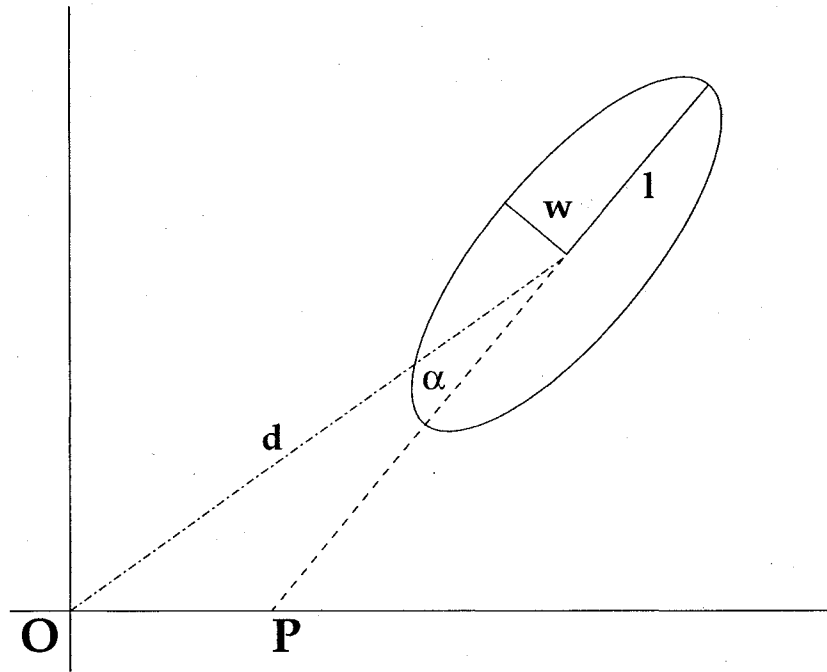
Figure 2.6: A picture describing a few of the relevant Hillas parameters for a γ-ray -like shower. **O** is the center of the camera, and **P** is the deduced point of origin of the γ-ray .

moments (rms spread and orientation) and third moments (skew). Parameters that describe such a light pool are w, the rms width of the elliptical image, l, the rms length, or extent of the semi-major axis, s, the size, or the sum of intensities of all pixels that constitute an image, d, the distance from the center of the ellipse to the center of the camera, and α, the angle between the major axis and the line connecting the image centroid and the position of the putative source.

Figure 2.7 shows Hillas parameters for a number of simulated cosmic-ray showers (Helium, in this case), and γ-ray showers over a range of energies. Equations 2.15 to 2.21 define some of the Hillas parameters, along with definitions of the moments of the light distribution.
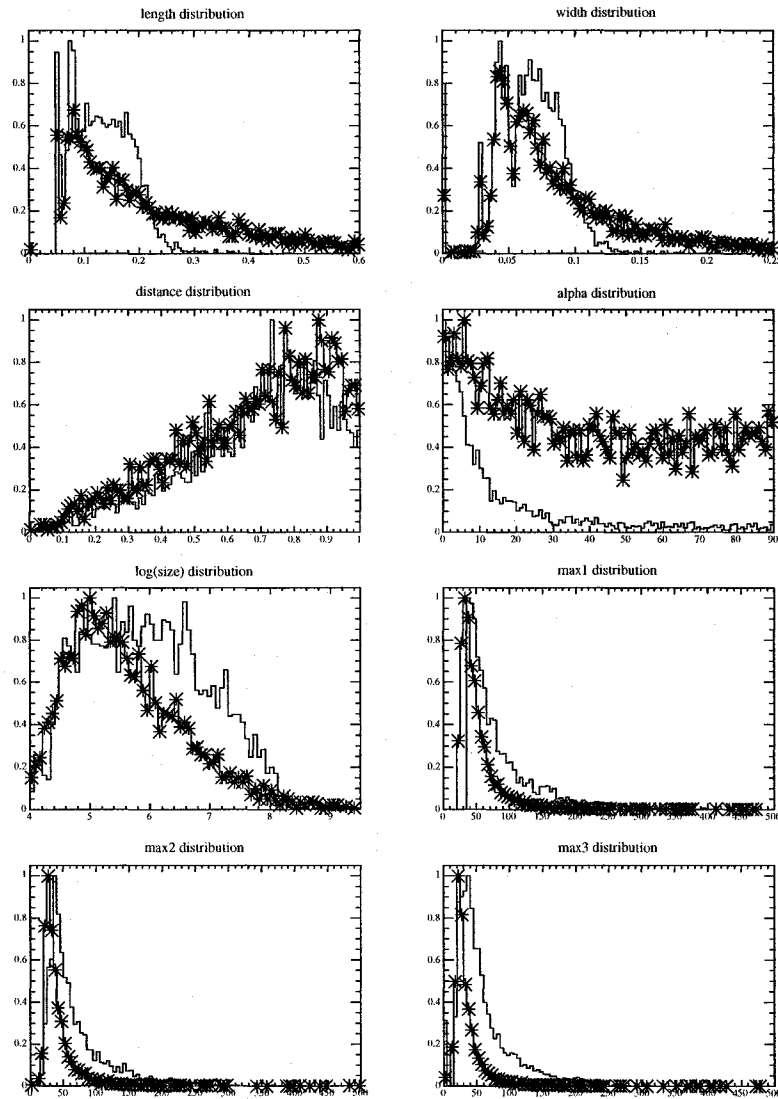
Figure 2.7: Histograms of relevant Hillas parameters for γ-ray showers (solid line) and Helium cosmic-ray showers (starred line).

28

$$\langle x \rangle = \frac{1}{S_{tot}} \sum_i S_i x_i$$

$$\langle y \rangle = \frac{1}{S_{tot}} \sum_i S_i y_i$$

$$\langle x^2 \rangle = \frac{1}{S_{tot}} \sum_i S_i x_i^2$$

$$\langle y^2 \rangle = \frac{1}{S_{tot}} \sum_i S_i y_i^2$$

$$\langle xy \rangle = \frac{1}{S_{tot}} \sum_i S_i x_i y_i$$

$$\text{SIZE} \equiv \text{S}_{\text{tot}} = \sum_i S_i x_i \qquad \text{moments} \qquad (2.15)$$

$$\sigma_x^2 \equiv \langle x^2 \rangle - \langle x \rangle^2$$

$$\sigma_y^2 \equiv \langle y^2 \rangle - \langle y \rangle^2$$

$$\sigma_{xy}^2 \equiv \langle xy \rangle - \langle x \rangle \langle y \rangle$$

$$d \equiv \sigma_y^2 - \sigma_x^2$$

$$z \equiv \sqrt{d^2 + 4(\sigma_{xy}^2)} \qquad \text{useful quantities} \qquad (2.16)$$

$$\text{LENGTH} \equiv \sqrt{0.5(\sigma_x^2 + \sigma_y^2 + z)} \qquad (2.17)$$

$$\text{WIDTH} \equiv \sqrt{0.5(\sigma_x^2 + \sigma_y^2 - z)} \qquad (2.18)$$

$$\text{DISTANCE} \equiv \sqrt{\langle x \rangle^2 + \langle y \rangle^2} \qquad (2.19)$$

$$\text{MISS} \equiv [(1 + d/z)\langle x \rangle^2 + (1 - d/z)\langle y \rangle^2]/2$$

$$-2\langle x \rangle \langle y \rangle \sigma_{xy}^2/z \qquad (2.20)$$

$$\alpha \equiv \text{ALPHA} \equiv \arcsin\left(\frac{\text{MISS}}{\text{DISTANCE}}\right) \qquad \text{Hillas parameters} \qquad (2.21)$$

From 2.7, it is clear that limits, or cuts, can be placed on each particular Hillas parameter to classify a γ-ray -like event from a cosmic-ray like one. By optimizing

29

these cuts on simulations or on data from a known source of γ-rays , such as the Crab Nebula, one can come up with a set of cuts that can maximize background reduction and the overall number of γ-rays accepted (for strong sources and spectral measurement), or, also one that can maximize the significance of detection (for discovery of weak sources).

Background Reduction

Normal observations at the Whipple 10m telescope come in two varieties. The first type of observation is known as an ON - OFF pair, in which a 28 minute run is taken pointing at the source (ON), followed by a 28 minute run taken at an offset of 30 min in Right Ascension (OFF). These two runs are taken at the same declination angle. In this manner, the OFF run tracks a different part of the celestial sphere, but at the same range of Altitude and Azimuth angles that the ON source observation did. This removes systematic errors that depend on zenith angle or slow changes in the atmosphere. This type of observation, therefore, is only possible on clear nights when the weather and atmospheric conditions (e.g. cloud cover) are stable. If the number of events passing the Hillas cuts described above are N_{ON} and N_{OFF} for the ON and OFF runs, respectively, we can find an estimate of the total number of γ-rays observed during the 28 minute ON run by taking the difference in the number of ON and OFF source events. The excess number of counts is given by

$$N_\gamma = N_{ON} - \beta N_{OFF} , \qquad (2.22)$$

30
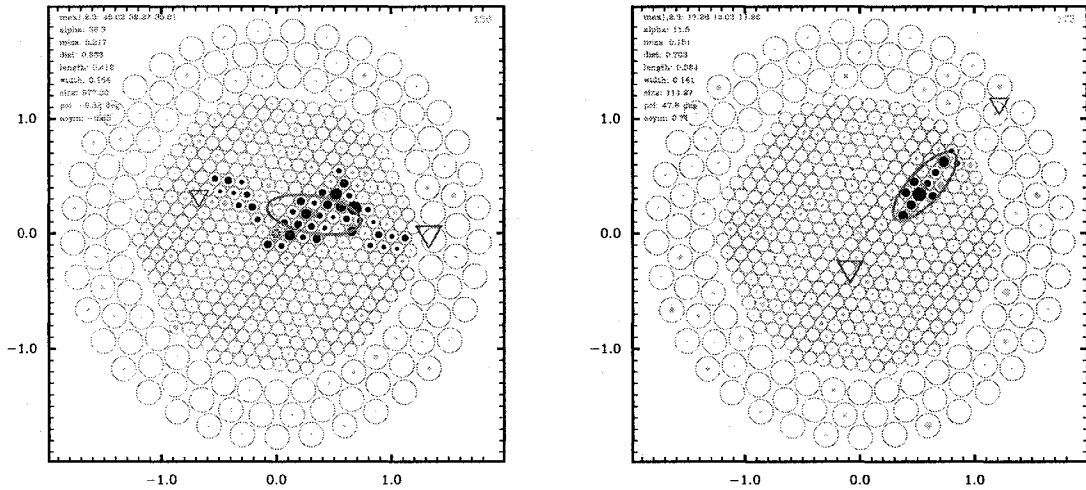
(a) A cosmic-ray-like image.

(b) A γ-ray -like image.

Figure 2.8: Two Cherenkov images from the Whipple 10m telescope. The small circles in each figure show pixel locations in the Whipple 10m camera. For pixels that show a signal (a dark circle inside the pixel), the relative size of the signal is signified by the size of circle drawn. The x and y axis are in degrees. The ellipses shown are computed using the derived length and width parameters. The large and small triangles in each figure point towards the two possible points of origin for each event - the the larger triangle of the two represents the preferred point of origin, based on an asymmetry parameter.

31

where β is the ratio of the durations of the OFF and ON runs (1 in this example). The significance of such a result can be defined as the simple ratio of the excess to the standard deviation of the background. Li and Ma (1983) provide a more precise likelihood ratio definition of the significance assuming that the ON and OFF-source counts follow a Poisson distribution, and that N_{ON} and N_{OFF} are ≥ 10:

$$S = \sqrt{2} \left(N_{ON} \ln \left[\frac{1+\beta}{\beta} \frac{N_{ON}}{N_{ON} + N_{OFF}} \right] + N_{OFF} \ln \left[(1+\beta) \frac{N_{OFF}}{N_{ON} + N_{OFF}} \right] \right)^{1/2}$$

$$(2.23)$$

In addition to ON - OFF observations, the Whipple 10m telescope also employs TRACKING-mode observations. These observations are identical to ON mode observations, only no corresponding OFF observation is taken. For TRACKING mode observations to be taken, the prospective source must be a known point source at the center of the camera, where adequate OFF-source data has been taken to understand the background. If this is true, the the number of γ-rays from the source is once again given by equation 2.22 where N_{OFF} and N_{ON} are determined from a histogram of α angles for the TRACKING mode observation. Based on previous analyses, N_{ON} is defined as the number of events passing cuts that have an α angle less than 15 degrees, and N_{OFF} is defined as the number of events passing cuts that have an α angle between 20 and 65 degrees. Since we assume a point source, N_{ON} are γ-ray -like events that point towards the source, and N_{OFF} are γ-ray -like events that do not. In this case β in equation 2.22 is the *tracking ratio*, and gives the expected number of

32

background events in the ON-alpha region based on a measurement of the number of background events in the OFF-alpha (20 to 65 degree) region. This ratio is determined from analyzing a number of OFF runs, by calculating

$$\beta = \frac{N(20° < \alpha < 65°)}{N(\alpha < 15°)} \, .$$

(2.24)

Empirically, $\beta \sim 1/3$. While ON - OFF observations must be taken on clear evenings, TRACKING mode observations can be taken in less than optimal weather, since the background is determined from a simultaneous measurement. For observations of a known variable source, temporal density and statistical significance can be improved by taking observations in the tracking mode. However, this is done at the expense of systematic error since there is no true OFF-source data to constrain the shape of the alpha distribution. Therefore, we follow a procedure established by the Whipple group (Buckley et al., 1996) whereby, whenever possible, each night of a multi-wavelength campaign consists of one ON-OFF pair and two TRACKING runs to balance statistical and systematic errors. Subsequent significance and errors quoted here will be derived from equation 2.23.

2.2 Multi-wavelength Approaches

Our understanding of active galaxies can greatly benefit from coordinated multi-wavelength observations in two major ways: First, temporal monitoring across wavebands allow observers to find time correlations or anti-correlations in the data. Strong

correlations in time, either with or without a lag between the two data sets, can be a strong discriminant in choosing models that describe the source properly. Second, spectral information across wavebands can be exploited to also discriminate amongst source models. A brief description of the three other wavebands used in this dissertation will now follow.

2.2.1 X-ray Observations

X-ray observations, as stated earlier, must be taken from space, as the atmosphere is opaque to X-ray radiation. The X-ray data that will be presented here come from the Rossi X-ray Timing Explorer (RXTE) satellite. RXTE, launched in 1995, contains three instruments. The Proportional Counter Array (PCA)(Jahoda et al., 1996) has an energy range from 2 to 60 keV, and consists of 5 proportional counters making up an effective area of 6500 cm^2. The All Sky Monitor (ASM)(Levine et al., 1996) has an energy range from 2 to 10 keV, and has the ability to perform a scan of 80% of the sky every 90 minutes. The final instrument aboard RXTE is the High Energy X-ray Timing Experiment (HEXTE)(Rothchild et al., 198). HEXTE has an energy range from 15 to 250 keV, and provides a time sampling of 8 μsec. Data presented here include monitoring data collected by the ASM, as well as pointed observations taken with the PCA as part of our group's approved multi-wavelength program.

34

2.2.2   Optical Observations

The optical observations that are presented here come from a number of ground based telescopes. While the atmosphere is transparent to visible light, the atmosphere still presents difficulties in observing. Photometric observations, like those presented here, rely on the use of a set of calibrated bandpass filters to accept only a predefined wavelength range for each measurement. The flux from the AGN in a given spectral band is compared to the flux of a star (using the same filter) either in the same field of view (relative photometry) or as part of a sequence of absolute standards taken in the same night (absolute photometry).

Mrk421, like other TeV Blazars, is a BL Lacertae object. One of the defining features of the BL Lac class is a lack of emission and absorption lines in a featureless optical spectrum dominated by broad-band nonthermal emission. This makes spectral measurements less important than relative aperture photometry for the multi-wavelength studies of Mrk421.

There are a number of challenges to performing optical photometry in active galactic nuclei. The nucleus of the galaxy which we are interested in is usually embedded in an optically bright host galaxy. To accurately determine the optical properties of the AGN, this host galaxy light must be taken into account, and subtracted in such a way as to only measure the light from the central nucleus. For Mrk421, two bright stars in the field of view further complicate matters since the tails of the diffraction

35

spikes from these stars overlap the position of Mrk421.

2.2.3 Radio Observations

Radio astronomy is also a ground based endeavor, large parabolic dishes are coupled with feed horns to measure a radio signal. As only specific wavebands are able to pass through the atmosphere, only these particular bands can be measured. Typically, radio observations operate at frequencies between 500 MHz and $\sim$ 10 GHz. Radio observations have a limitation for our purposes in that at these energy ranges one is typically measuring behavior far from the central engine of the AGN. X-ray and γ-ray measurements on the other hand tend to originate earlier in the jet, and closer to the central engine. While radio observations are among the highest in angular resolution (using long-baseline interferometry), emission from the inner few parsecs of the AGN is typically obscured by synchrotron-self absorption.

Chapter 3

Results

3.1 Observations and Standard Data Reduction

3.1.1 TeV γ-ray Measurements

TeV observations were taken with the Whipple 10 m Cherenkov telescope (Mount Hopkins, AZ) and with the CT1 telescope of the High Energy Gamma-Ray Astronomy (HEGRA) collaboration (La Palma, Spain). In this section I describe the two data sets.

The Whipple observations were taken between 4 December 2002 (UT) and 15 January 2003 (UT). A total of 44 hrs of data were acquired: 32 hrs on the source, and 12 hrs on an adjacent field for background estimation purposes. The data were analyzed using the standard "Hillas" 2nd-moment-parameterization technique. Standard cuts (`SuperCuts2000`) were used to select γ-ray events and to suppress background cosmic-ray events. The fluxes were normalized to the flux from the Crab Nebula

37

using a data set of 15 hrs of on-source data and matching background observations taken in December 2002 and January 2003. Using the zenith angle dependence of this Crab data set we account for the zenith angle dependence of the γ-ray excess rate by simply normalizing our measured Mrk421 rate to the Crab rate at a corresponding zenith angle. Significances and corresponding error bars were calculated using the method of Li and Ma (1983).

From Monte Carlo simulations, we fold the Crab spectrum with the instrument response to obtain the peak energy (energy threshold) for the Whipple 10m data to be consistent with the value 400 GeV derived elsewhere (Petry et al., 2002). More detailed descriptions of Whipple observing modes and analysis procedures can be found elsewhere (Weekes, 1996; Punch and Fegan, 1991; Reynolds et al., 1993). Details about the Whipple telescope including the GRANITE-III camera have been given in Finley et al. (2001).

A second TeV γ-ray data set was acquired with the HEGRA CT1 telescope (see Rauterberg (1995) for a description of the CT1 instrument) between 3 November 2002 and 12 December 2002. The telescope was equipped with a 127 pixel camera with a $3°$ diameter field of view, and with an effective area of $10\,\mathrm{m}^2$ (Mirzoyan, 1994). The analysis used 17 hrs of data with zenith angles between $12°$ and $58°$. The HEGRA CT1 data were normalized to the Crab flux in a similar way as the Whipple data. We estimate a mean energy threshold for the CT1 data set of approximately 700 GeV.

38

The normalization to the steady Crab flux is a convenient way to combine data from different instruments to avoid systematic errors resulting from errors in the absolute flux calibration of each instrument, and to perform a first-order correction for variations in rate with zenith angle. The drawback of the method is that the different energy thresholds of the Whipple and HEGRA observations can introduce a normalization error if the source energy spectrum deviates from the Crab energy spectrum. Using previous measurements of the Mrk 421 TeV spectral index as a function of flux level, we estimate that the Whipple/HEGRA normalization error is always smaller than 30%. Based on the Whipple measurement of the energy spectrum from the Crab nebula (Hillas et al., 1998), a flux of 1 Crab corresponds to a differential 1 TeV flux of $(3.20 \pm 0.17_{\text{stat}} \pm 0.6_{\text{syst}}) \times 10^{-11}$ photons cm^{-2} s^{-1} TeV^{-1} and to a νF_ν of $(5.12 \pm 0.27_{\text{stat}} \pm 0.96_{\text{syst}}) \times 10^{-11}$ ergs cm^{-2} s^{-1}.

3.1.2   X-ray Measurements

We reduced the data from the *RXTE* Proportional Counter Array with the standard *RXTE* data analysis software. Standard-2 mode PCA data taken with the top layer of the operational Proportional Counter Units (PCUs) were analyzed. The number of PCUs operational during a pointing varied between 2 and 4. We restricted the spectral analysis to the energy range from 4 keV to 15 keV. We excluded data below 4 keV, as some showed corrupted behavior (exceptionally high or low count rates of individual bins not compatible with the energy resolution of the instrument). The high-energy cut-off was chosen to guarantee more than 10 counts per energy bin for all data sets, a

pre-requisite for using the χ^2-fitting method for parameter estimation. After applying the standard screening criteria and removing abnormal data spikes, the net exposure in each Good Time Interval ranged from 168 sec to 9.01 ksec. Light-curves were then extracted with `FTOOLS v5.0`. Background models were generated with the tool `pcabackest`, based on the *RXTE* guest observer facility (GOF) calibration files for a "bright" source (more than 40 counts/sec/PCU). Response matrices for the PCA data were created with the script `pcarspv.7.11`. For each pointing, a power law model was fitted over the energy range from 4 keV to 15 keV. The analysis of this X-ray data was performed by Washington University graduate student Scott Hughes.

We complement the data from the pointed RXTE telescopes with data from the RXTE All Sky Monitor (ASM) (Levine et al., 1996) taken between December 2, 2002 (UT) and January 14, 2003 (UT). We derived fluxes by averaging the "summed band intensities" acquired during one day.

3.1.3 Optical Measurements

In the following, we will discuss three optical data sets. The first was taken at the Boltwood Observatory (Stittsville, Ontario, Canada) with a 0.4 m telescope, a SiTe 502A CCD chip, and a Johnson-Cousins R filter. The data were collected for $\sim$ 10 days between December 3, 2002 and January 12, 2003. Relative aperture photometry was performed with an aperture of 10 arcsec and "star 1" from Villata et al. (1998) as the comparison star. The background was estimated using a concentric annulus

with a diameter between 37 and 44 arcsec. We did not subtract the light from the host-galaxy. Usually, five two-minute exposures were integrated before deriving the photometric value. The typical statistical error on the relative photometry is 0.02 mag. The analysis is compromised by two very bright stars near Mrk 421 that cause a varying level of light to spill into the source and background regions. Based on previous optical results on the same source and stars in the field of view, we estimate that photometric measurements have a systematic error of 0.08 mag per data point.

The second set of optical observations were made using a 35 cm Celestron telescope installed on the tube of the 60 cm KVA telescope (La Palma, Spain). The observations were made with the ST-8 CCD using a standard Kron/Cousins R-filter. The analysis used the reduction programs developed by Kari Nilsson (Tuorla Observatory) with the reference stars one and two from Villata et al. (1998).

The final set of optical data were collected using the WIYN 0.9 m telescope at KPNO with the S2KB CCD imager using a Harris V-filter. The data were collected from 6 December 2002 to 15 January 2003 (with, however, a large gap 9 Dec 2002 to 3 Jan 2003). Relative aperture photometry was performed using standard IRAF routines with an aperture of 6 arcsec, sky annulus ranging from 27 to 30 arcsec in diameter, and "star 1" of Villata et al. (1998) as the comparison star. Again, we did not subtract light from the host galaxy. Typical statistical errors from the photometric fits were smaller than 0.005 mag. Based on the spread in magnitude difference between two reference stars, we estimate the uncertainty for each data

41

point to be 0.02 mag for the purpose of determining variability, although a larger systematic error ($\sim$ 0.08mag) might be present due to background from the bright reference stars. With regard to the absolute flux, due to the presence of host-galaxy light, we expect the values reported to contain an undetermined systematic offset of as much as 0.1 mag. Optical magnitudes for all three data sets are converted to absolute fluxes according to Allen (1973).

3.1.4 Radio Measurements

We used the University of Michigan equatorially mounted 26-meter paraboloid in its automatic observation mode to observe Mrk 421 at 4.8 GHz, 8.0 GHz and 14.5 GHz between December 3, 2002 and January 10, 2003. Both linear polarization and total flux density measurements were made, but only the total flux density measurements are reported here. Each observation consisted of a series of five-minute ON-OFF type measurements over a 40-minute time period interleaved with observations of other program sources. Observations were restricted to within three hours of the local meridian to minimize instrumental errors. The telescope pointing corrections are interpolated from position scans through sources stronger than 2 Janskys. The flux density measurements have been corrected to the Baars flux density calibration scale (Baars et al., 1977) using observations of a grid of calibrator sources, distributed around the sky, which were observed at approximately two-hour intervals. The 1σ error bars include both the estimated measurement and calibration uncertainties. The observation and calibration procedures have been described in more detail elsewhere

42

(Aller et al., 1985).

3.2   Determination of TeV γ-ray Energy Spectra with the Forward Folding Method

The spectral analysis of the Whipple TeV γ-ray data used a different set of gamma-hadron separation cuts that minimize the systematic error associated with uncertainties in the γ-ray selection efficiency of the cuts while still giving a good sensitivity. The "extended zenith angle scaled cuts" (Kosack et al., 2004) select primary γ-rays with an efficiency that is largely independent of the zenith angle of the observation and the energy of the primary photon. The analysis is based on the Grinnell-ISU (GrISU) package[1] that uses the KASCADE air-shower simulation code (Kertzman and Sembroski, 1994), followed by the simulation of the Cherenkov light emitted by the air shower and the simulation of the detector response. To calibrate the overall gain of the Whipple 10m telescope in the simulations, we compared simulated and observed muon events. Muons show up as bright arcs of Cherenkov light in the camera and are useful for calibration because the light per unit arc length is nearly constant, regardless of the impact parameter and angle of the muon trajectory. The overall gain of the telescope can be found by comparing the distribution of the signal per arc length in a simulated set of muon events and in an observed set. We took the simulated muon events from a sample of simulated proton and helium showers.

---

[1]   http://www.physics.utah.edu/gammaray/GrISU

43

Muons are identified with a dedicated muon identification algorithm that extracts ~ 200 muon arcs per 28 min data run. We adjusted the overall gain factor in the simulations until they reproduced the observed signal per arc length distribution (see Kosack (2005) for details). The overall gain factor agrees to within 15% with the value computed from measurements of the mirror reflectivity, photo-multiplier tube (PMT) quantum efficiency, and electronic gain.

We used the forward folding technique to fit the energy spectra. Although earlier TeV γ-ray analyses used similar methods, this new method was first implemented by Kosack (2005). Here I offer a more complete description of the method as presented in our published paper (Rebillot et al., 2006). For each Cherenkov event that passed the gamma-hadron separation cuts, we computed an estimator E of its primary energy, based on the image parameters '*size*' S (sum of counts in an image) and '*distance*' d (distance of the image centroid from the center of the field of view):

$$\ln E \;=\; g(x) + h(d) \;, \tag{3.1}$$

with $x = \ln S$, $g(x) = A + Bx + Cx^2$ and $h(d) = D_1 + \alpha d$ for $d < d_0$ and $h(d) = D_2 + \beta d$ for $d > d_0$. The values of the constants A, B, C, D_1, D_2, α, β, and d_0 were determined by fitting to simulations (Kosack, 2005) and are given in Table 3.1. Using extended zenith angle cuts, the energy estimator gives an energy resolution of $\sigma(\ln E) = 0.25$. We limited the spectral analysis to ON-OFF data taken at zenith angles less than 30° (see section 2.1.3 for a discussion of data taking methods). After histogramming the energy estimator for the signal and the background regions, the

44

Parameter	Value
A	-7.05
B	1.30
C	-0.034
D_1	0.057
α	-0.20
D_2	-1.96
β	2.44
d_0	0.75°

Table 3.1: Parameters used for the TeV γ-ray energy estimator.

background histogram was subtracted from the signal histogram. Subsequently, an

energy spectrum was fitted to the "excess histogram" using the standard forward

folding approach, making use of a simulated set of γ-ray showers. The data set

consisted of 67,500 showers simulated over an area $A_{MC} = \pi (400\,\text{m})^2$ in the energy

range from 50 GeV to 25.6 TeV over nine energy intervals. The first energy interval

went from 50 to 100 GeV, and each subsequent interval was a factor of 2 larger than

the one before it. In each energy interval i, the showers were distributed in energy

according to a power law energy spectrum $dN_{MC}^{(i)}/dE = N_i (E/1\text{TeV})^{-\Gamma_{MC}}$, with

$\Gamma_{MC} = 2.5$. We fit two models:

$$\frac{dN_\gamma}{dE} = N_0 \times (E/1\,\text{TeV})^{-\Gamma} \tag{3.2}$$

45

and

$$\frac{dN_\gamma}{dE} = N_0 \times (E/1\,\text{TeV})^{-\Gamma} \times \exp\left(-E/E_0\right) , \tag{3.3}$$

where N_0 is the flux normalization at 1 TeV, Γ is the photon index and E_0 is an optional high-energy cutoff. For each trial parameter set $\mathcal{P}$ (with $\mathcal{P} \in \{\mathcal{N}_i, -\}$ or $\mathcal{P}_\epsilon \{N_0, \Gamma, E_0\}$), another "excess histogram" is filled with appropriately weighted simulated γ-ray showers that pass the γ-ray selection cuts. The weight is:

$$W_i(E; \mathcal{P}) = \frac{\frac{dN_\gamma}{dE}(E; \mathcal{P}) \times \Delta t}{N_i \times E^{-\Gamma_{MC}}/A_{MC}} , \tag{3.4}$$

where Δt is the duration of the data set, and A_{MC} is the simulated shower area, and

$$N_i = (\Gamma_{\text{MC}} + 1) \times \left(n_i \times \left[E_{\text{min,i}}^{\Gamma_{\text{MC}}+1} - E_{\text{max,i}}^{\Gamma_{\text{MC}}+1} \right]^{-1} \right) . \tag{3.5}$$

Here, n_i is the number of showers simulated in the ith energy interval that stretches from energy $E_{\text{min,i}}$ to $E_{\text{max,i}}$. Equation 3.5 defines N_i such that the integral over the denominator in Eq. 3.4 from $E_{\text{min,i}}$ to $E_{\text{max,i}}$ equals n_i. The weight depends on the true energy of the simulated γ-rays ; the showers are filled into the excess histogram according to their reconstructed energy. The numerator in Eq. 3.4 gives for the parameter combination $\mathcal{P}$ the model fluence (flux times integration time Δt) at an energy E. The denominator gives the fluence that has actually been simulated. This procedure is designed to save computational time in the fitting procedure, since only the weighting function, and not the simulations themselves, need be repeated for each iteration.

46

We performed a search in parameter space until the parameter combination $\mathcal{P}_{\mathrm{min}}$ is found that minimizes the χ^2-difference between the observed and simulated excess histograms. We determined the $1\,\sigma$ error region from the condition (Press et al., 1992)

$$\chi^2(\mathcal{P}) \leq \chi^2(\mathcal{P}_{\mathrm{min}}) + 1 \ . \tag{3.6}$$

The best fit model parameters and the associated errors are the main results of a spectral analysis. Plotting individual data points in an energy spectrum is well known to be an ill-defined problem. A very good discussion can be found in Loredo and Epstein (1989). Owing to the finite energy resolution of the telescopes, some information about the true energy spectrum is irrevocably lost. We have experimented with "deconvolution methods", as for example, the Backus-Gilbert method (Backus and Gilbert, 1970; Loredo and Epstein, 1989). Owing to a combination of almost Gaussian distributions of $\ln\,(E_{\mathrm{true}} - E_{\mathrm{rec}})$ and $E_{\mathrm{true}} - E_{\mathrm{rec}}$ and the modest signal-to-noise ratios of the TeV γ-ray energy spectra, we find that deconvolution methods improve only very little the effective energy resolution.

We thus use the simplest method to plot flux estimates, based on the counts in the excess histogram (see e.g. Fenimore et al. (1982)). For an energy bin stretching from E_1 to E_2, we plot the flux value at the energy $E = 10^{(\log\,(E_1)+\log\,(E_2))/2}$. The flux value is given by scaling the best-fit model according to the observed number of excess counts:

$$f = \frac{dN}{dE}\,(\mathcal{P}_{\mathrm{min}}) \times \frac{k_i}{<k_i>} \ . \tag{3.7}$$

Here, k_i is the number of excess counts in the ith bin of the signal histogram, and $< k_i >$ is the sum of weights of the simulated events in the ith bin.

To verify our method, we determined the spectrum of the Crab Nebula, a well studied steady source for which the spectrum has previously been determined by a number of groups (Whipple, HEGRA, and CAT). Figure 3.1 shows the Crab spectrum from small zenith angle data ($< 30°$) acquired between 14 September 2002 (UT) and 24 March 2003 (UT), and the time averaged TeV γ-ray spectrum of Mrk 421 for the data set of the multi-wavelength campaign. Both data sets are from the Whipple 10 m telescope. The power law fit to the Crab data gives a flux normalization of $2.42 \pm 0.11 \times 10^{-11}$ photons cm^{-2} s^{-1} TeV^{-1}, and a photon index of $\Gamma = 2.5 \pm 0.1$. The χ^2 is 5.27 for four degrees of freedom. The results agree well with the previous results published by the Whipple and HEGRA collaborations (Hillas et al., 1998; Aharonian et al., 2004). The power law fit to the Mrk 421 ON-OFF with zenith angle greater than $30°$ data set gives a flux normalization of $1.7 \pm 0.1 \times 10^{-11}$ photons cm^{-2} s^{-1} TeV^{-1}, and a photon index of $\Gamma = 2.8 \pm 0.1$. The χ^2 is 5.06 for 4 degrees of freedom. The flux and spectral index lie in the range of previous observations (Zweerink et al., 1997; Aharonian et al., 1999; Krennrich et al., 1999). We find that the photon statistics do not allow us to derive meaningful constraints on the high-energy cutoff E_0.

Using the best-fit parameters from the Crab spectral analysis, we can weight the Monte Carlo events by the determined spectrum and compare several simulated distributions of the image parameters with the background subtracted distributions for

48
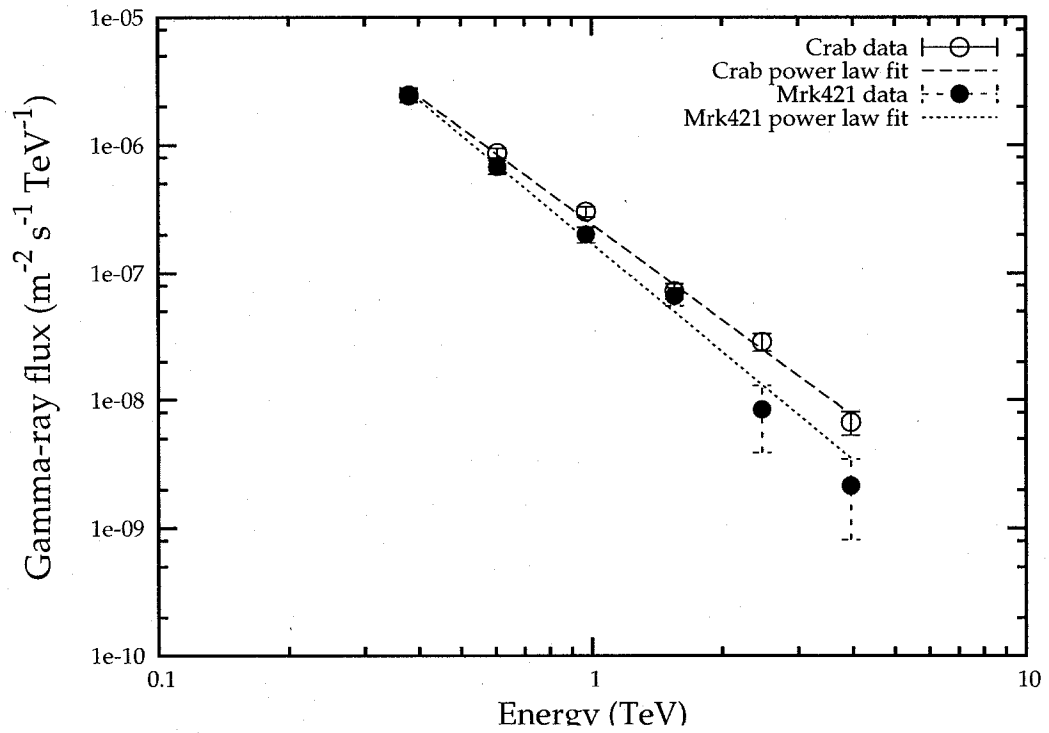
Figure 3.1: Whipple TeV spectrum of the Crab nebula and Mrk 421. The dashed and dotted lines give the results of power law fits for the Crab and Mrk421, respectively.

49

the Crab data (Figure 3.2). The good agreement between simulated and experimental data verifies that the simulations describe the air showers and the detector response adequately.

3.3 Results from the Multi-wavelength Campaign

3.3.1 Overview

Figures 3.3 and 3.4 combine all the light-curves measured in December 2002, and January 2003, respectively. From top to bottom, the figures show the TeV γ-ray flux data, TeV photon indices Γ, (where $dN/dE \propto E^{-\Gamma}$), *RXTE* PCU 10 keV flux amplitudes (from the 4-15 keV spectral fits), the 4-15 keV photon indices, the *RXTE* ASM 2-12 keV fluxes, the optical data, and the radio data. The TeV γ-ray fluxes varied between 0 to $\sim$ 2 times that of the Crab nebula, with slightly higher fluxes observed during the second half of the campaign. We determined TeV photon indices on a night to night basis whenever the flux was sufficiently high to warrant a spectral analysis. For epochs of low fluxes (December 6 and 7, 2002 (UT) (MJD 52614-52615), December 8, 9 and 10, 2002 (UT) (MJD 52616-52618), December 14, 15, and 16, 2002 (UT) (MJD 52622-52624), and January 7 and 8, 2003 (UT) (MJD 52646-52647)) we combined the data of several nights to determine an energy spectrum. A χ^2 test of statistical variability was performed by fitting the entire TeV photon index dataset to a constant function. The best fit to the data, with 2σ errors, is $\Gamma = -2.864 \pm 0.097$, with a χ^2 value of 46.5 for 20 degrees of freedom. The probability of obtaining

50

Figure 3.2: Hillas parameter distributions for Whipple 2002-2003 Crab ON/OFF data and simulated data. Histograms show simulated data, while data points show Crab data. The "Alpha ON, Alpha OFF" plot shows actual ON and OFF data from the Crab, while the "Alpha ON-OFF, Alpha MC" plot shows the subtracted ON - OFF distribution, compared to Monte Carlo simulations.

51
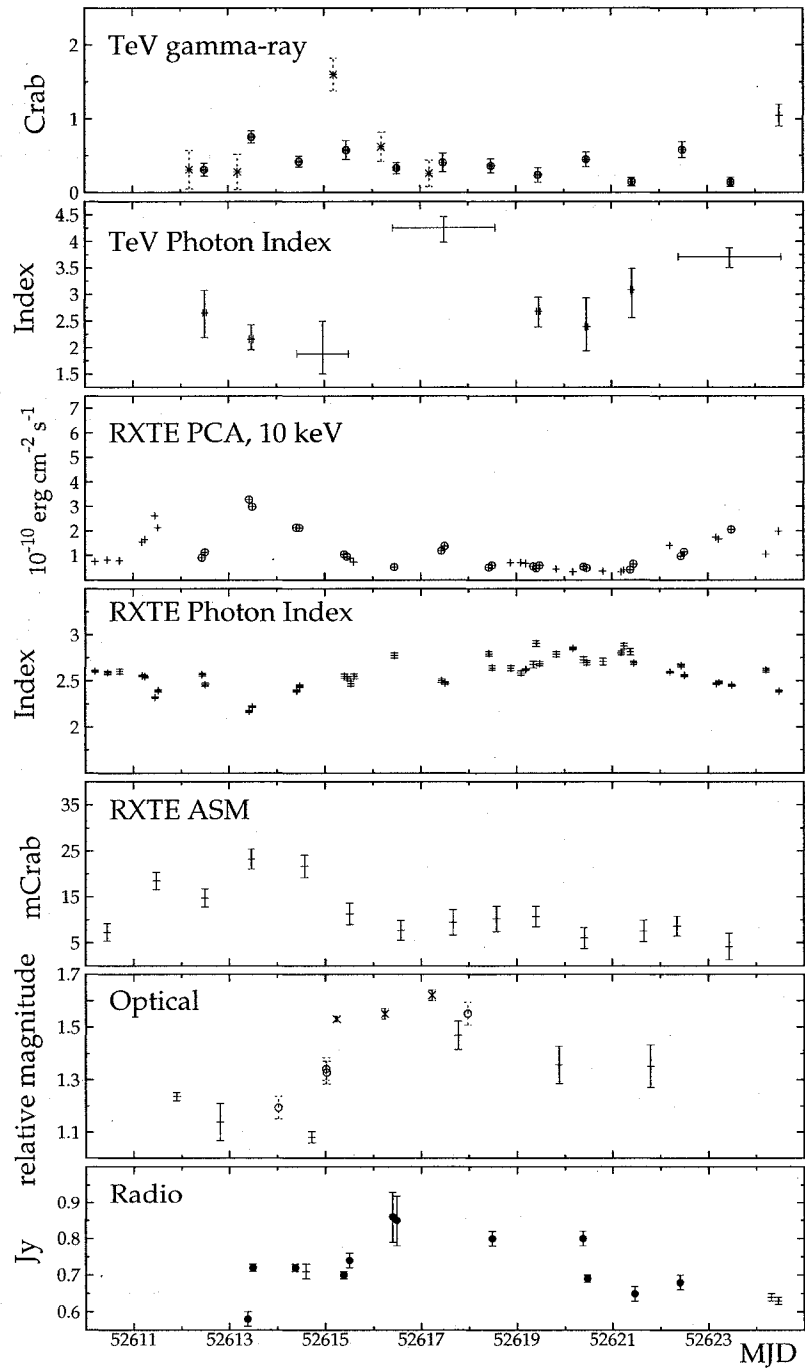
Figure 3.3: Multi-wavelength data from December, 2002. The γ-ray flux data points show per-night averages, in crab units. Starred data points signify data taken from the HEGRA CT1 telescope, while crosses denote Whipple 10m data. The error bars on the RXTE PCA data are not shown as they are smaller than the symbol size, and have units of 10^{-10} erg cm^{-2} s^{-1} at 10 keV. The circled X-ray and γ-ray data points overlapped or were taken less than 5 min apart. The TeV γ-ray and RXTE photon indices show Γ, where $dN/dE \propto E^{-\Gamma}$. The ASM data are given in mCrab. In the optical band, open circles show the WIYN V band data, crosses show the Boltwood R band data, and 'x' denotes La Palma R band data. All of the optical data are in relative magnitude units. The open (filled) circles in the radio band show measurements that overlapped or were taken within 5 min of a TeV γ-ray observation (X-ray and TeV γ-ray observation). The radio data are given in Janskys.

53
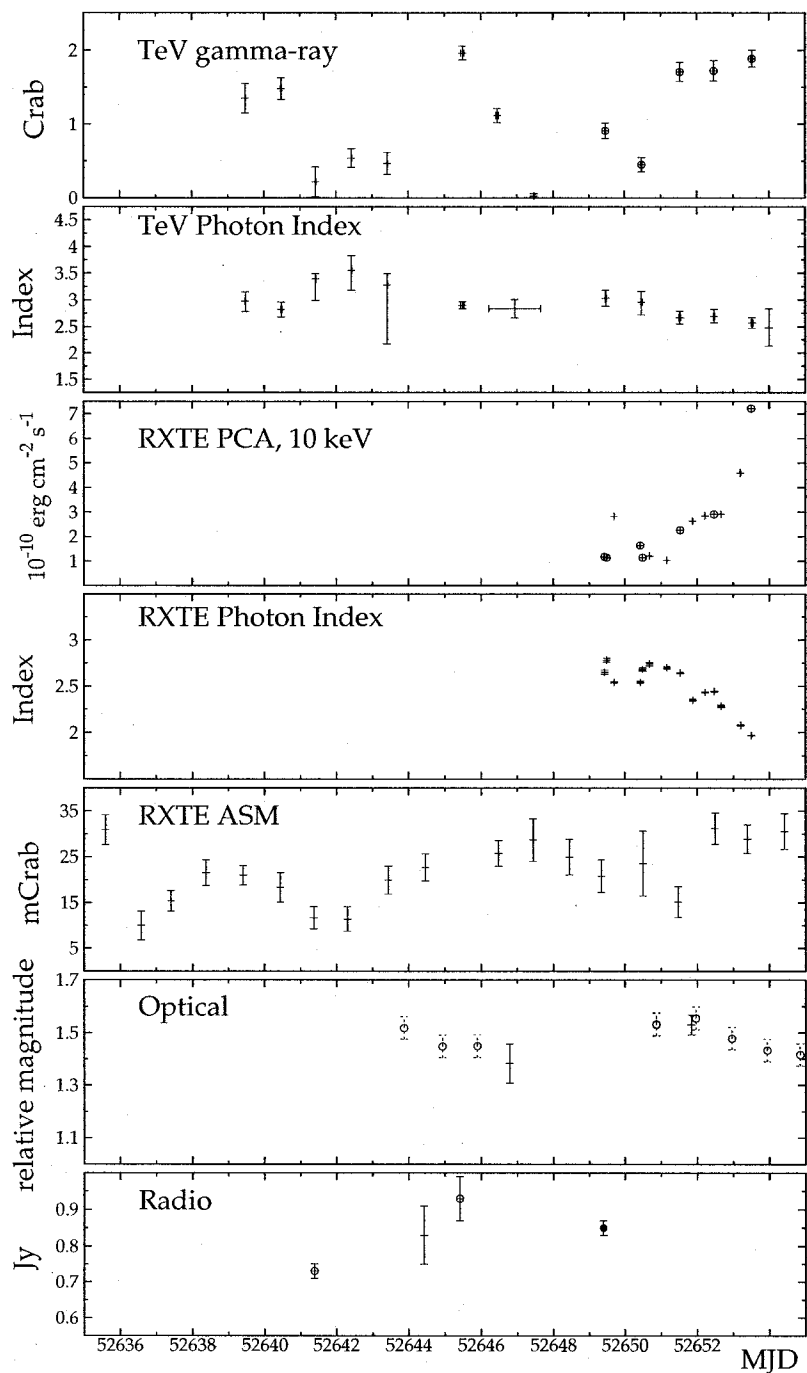
Figure 3.4: Same as Figure 3.3 for the data from January 2003.

54

this value by chance is 2.2×10^{-4}. Seven data points lie outside the 2σ confidence region. For the first and third spectrally-variable time periods (MJD 52615-52617, MJD 52641-52643), the spectral variability seems to trail significant variations in the flux.

The 4-15 keV *RXTE* data is shown in Figures 3.3 and 3.4. The X-ray fluxes varied between 0.2×10^{-3} cts cm^{-2} s^{-1} keV^{-1} and 4.5×10^{-3} cts cm^{-2} s^{-1} keV^{-1}. Strong flares were observed on December 3, 2002 (MJD 52611), December 5, 2002 (MJD 52613), January 10, 2003 (MJD 52649), and on January 14, 2003 (MJD 52653). The 4-15 keV X-ray photon indices show a large range of values from $\Gamma = 1.97$ to $\Gamma = 2.90$.

The values of $\Gamma \geq\sim 2$ indicate that the presumed synchrotron SED peaked at and below the 4-15 keV energy range covered by observations. In two cases, the X-ray index varies very rapidly: on MJD 52619 it changes by $\Delta\Gamma = 0.22$ within 1.4 hrs, and on MJD 52650 it changes by $\Delta\Gamma = 0.14$ within 1.6 hrs.

If the X-ray emission is indeed synchrotron emission from a population of high-energy electrons, a change in the observed photon spectrum $dN_\gamma/dE \propto E^{-\Gamma}$ by $\Delta\Gamma \approx 1$ corresponds to a change in the electron energy spectrum $dN_e/dE \propto E^{-p}$ by $\Delta p \approx 2$. Synchrotron cooling of a power-law distribution of electrons steepens an electron power-law by no more than $\Delta p = 1$. **Thus, the wide amplitude of the spectral changes observed here implies that we may see evidence for the high-energy cutoff of accelerated electrons moving into the energy range sampled by the observations.** Alternatively, flares might be associated

55

with changes of several parameters constraining the emitting plasma, as for example the jet magnetic field or the jet beaming angle.

The *RXTE* PCU and ASM fluxes seem to trace each other, although the sparse sampling of the PCU data and the large statistical error bars of the ASM data do not allow us to draw definitive conclusions. The optical and radio data show substantial variability by about $\pm 50\%$ of the mean flux, but no detailed correlation is present. This is not a surprise since for the optical data one expects sizable contributions from the galaxy light and perhaps thermal emission from the accretion region in addition to optical synchrotron. Furthermore, one expects longer variability timescales for the lower energy synchrotron radiation, since the lower energy electrons which produce this radiation cool more slowly. Since synchrotron self-absorption may make the inner jet (where the shorter γ-ray and X-ray variability is likely to occur) opaque, the radio emission is likely to come further out along the jet from a larger region.

3.3.2   The X-Ray/TeV γ-ray Flux Correlation

We studied the X-ray and TeV γ-ray flux correlation with the help of the discrete correlation function (DCF) of Edelson and Krolik (1988). The DCF gives the linear correlation coefficient for the two light curves as a function of a time lag between them. The DCF is the standard tool used in the case of sparsely sampled data and gives fewer spurious results than a traditional correlation function analysis that interpolates between light-curve data points. We determined the statistical significance of the

56

correlation coefficients with the help of a set of simulated γ-ray light curves, computing for each simulated light curve the DCF with the observed X-ray data. These light-curves are generated by a superposition of triangular shots, with all shots having the same amplitude and the same rise and fall time.

Figure 3.5 gives the DCF for the X-ray and TeV γ-ray data sets. For a time lag of zero days, we find a DCF value of 0.58 ± 0.12. The simulated data sets show that the correlation is significant. For uncorrelated lightcurves consisting of triangular shots with the same structure function, we calculate that the chance probability to get a larger DCF value at a time lag of zero days is 3.12%. Figure 3.6 shows the X-ray/TeV γ-ray flux correlation for all overlapping observations. The measurements entering this figure are shown by the circled data points in Figures 3.3 and 3.4. The correlation shows substantial scatter, with similar X-ray (TeV) fluxes sometimes corresponding to TeV (X-ray) fluxes that differ by more than a factor of 2 from each other. The scatter may be an inherent property of the emission mechanism. Alternatively, it may be caused by a short time lag between the flares in the two bands, not resolved by the sparse sampling during the campaign.

3.3.3   Evolution of the X-ray Spectral Indices

Figure 3.7 shows the correlation between the 10 keV fluxes and the 4-15 keV photon indices. A correlation can clearly be recognized in the sense that higher fluxes are accompanied by harder energy spectra. The correlation is similar to the flux/hardness correlations reported for other BL Lac-type objects, e.g. Mrk 501, 1ES 1959+650,

57
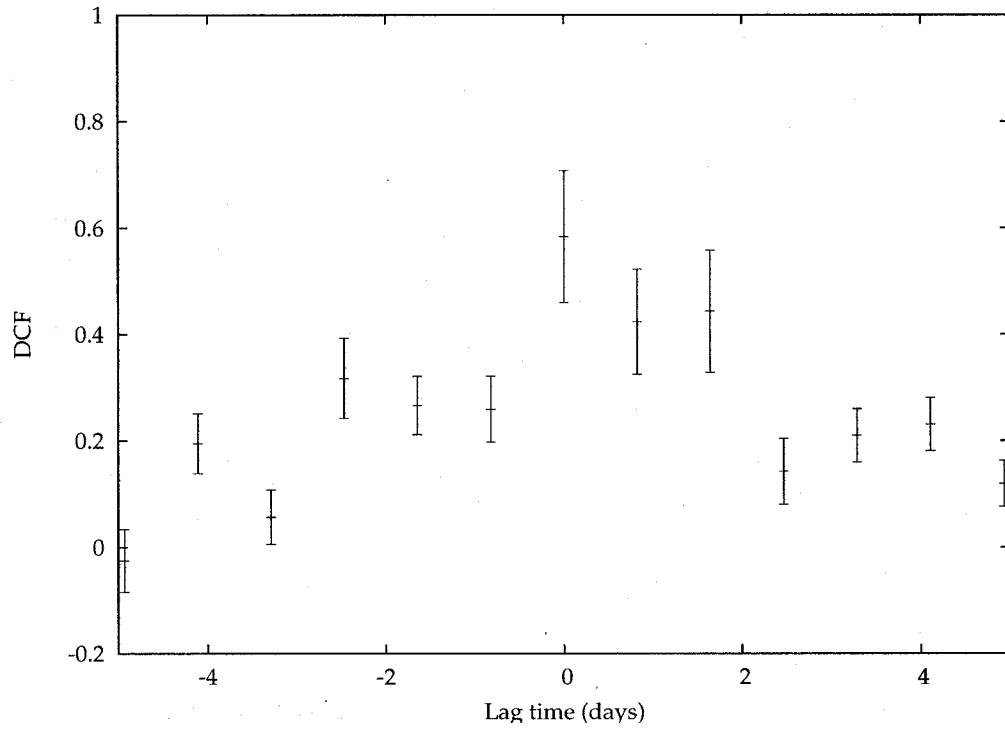
Figure 3.5: Discrete correlation function of the complete X-ray and γ-ray data set. A positive time lag means the γ-ray flux precedes the X-ray flux.
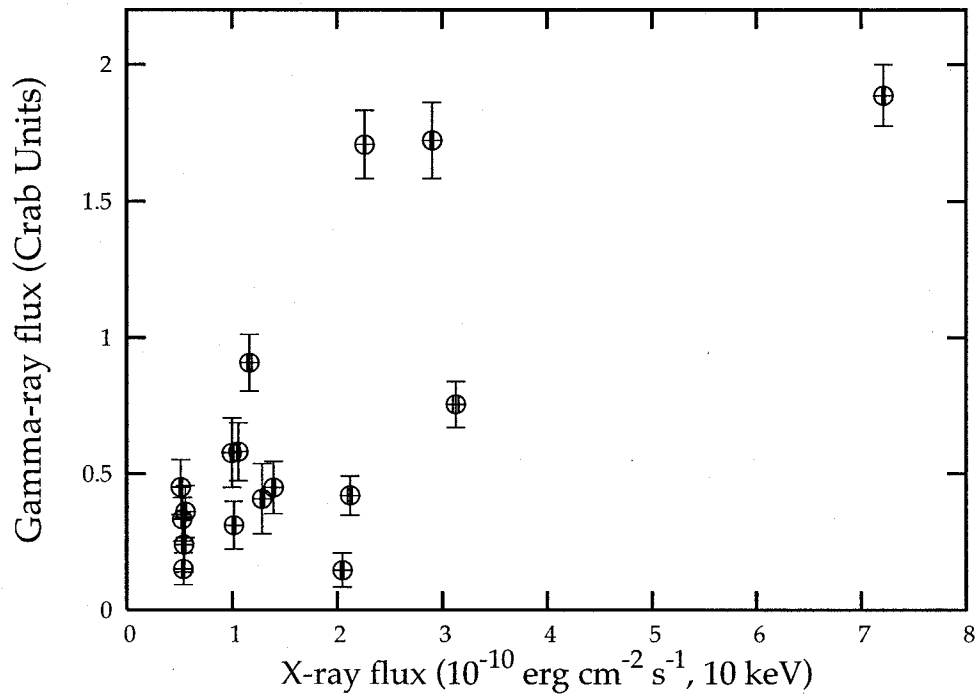
Figure 3.6: Plot of the TeV γ-ray versus X-ray flux correlation for measurements for all overlapping data sets.
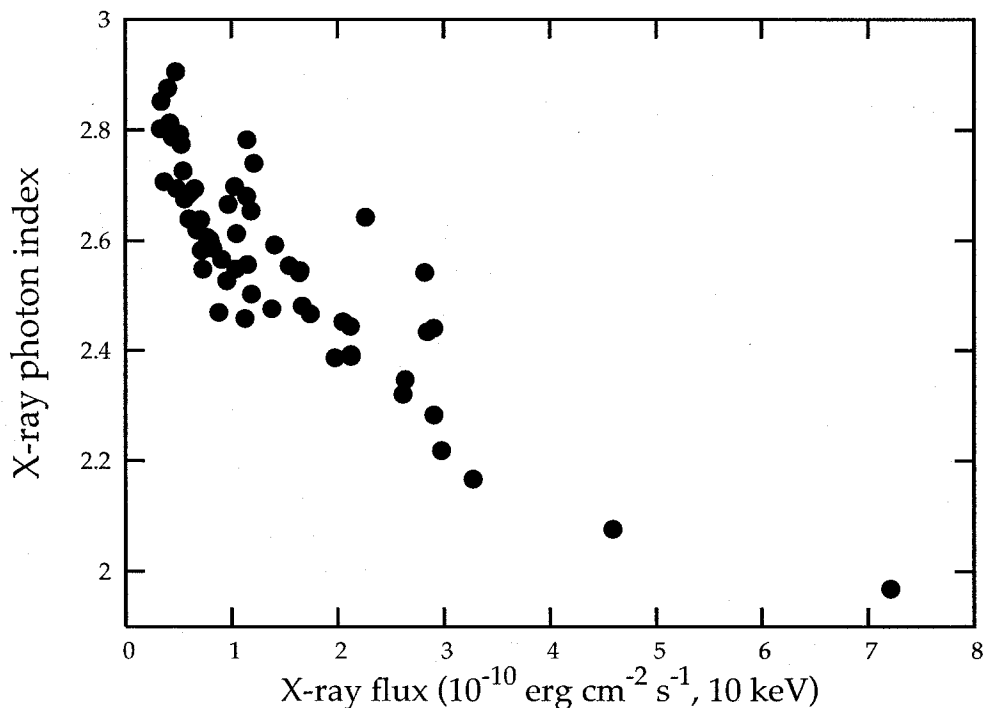
Figure 3.7: Correlation of the 10 keV X-ray flux and the 3-14 keV photon index (both: RXTE PCA data).

1H1426, and PKS 2155. We further scrutinized the temporal evolution of the spectral indices with so called X-ray "hysteresis" curves (Takahashi et al., 1996; Kirk and Mastichiadis, 1999; Kataoka et al., 2000), plotting the X-ray photon index as a function of X-ray flux, and indicating the temporal sequence of the measurement throughout the evolution of individual flares. In the simplest model whereby flares are formed by short lived shocks (e.g. internal shocks from colliding blobs), one expects the temporal evolution to be dictated by the interplay of the acceleration, cooling, and

60

confinement times. For the Fermi mechanism, the particle energies reached depend on the allowed acceleration time. Thus, during the beginning of flares, the X-ray and γ-ray energy spectra are expected to harden. Once synchrotron cooling starts to dominate the particle energy spectra, the emitted photon energy spectra are expected to soften. We studied two X-ray flares, one occurring at the beginning of the campaign (MJD 52612 to MJD 52615), and the other at the end (MJD 52651 to MJD 52653). The first flare is shown in Figure 3.8. This flare coincided with an increase of the TeV γ-ray flux by a factor of 2.4 from MJD 52612 to MJD 52613. The X-ray spectrum hardens during the rising phase of the flare and softens during the decaying phase. Furthermore, the X-ray spectrum is softer during the falling phase than during the rising phase. The "clockwise" evolution in the $\Gamma_x - F_x$ plane is consistent with earlier results (Takahashi et al., 1996), and with the expectations from Fermi acceleration and synchrotron cooling. The data of the second flare are shown in Figure 3.9.

The TeV γ-ray flux increased from MJD 52650 to MJD 52651 by a factor of 3.8 and remained roughly constant during the following two nights of observations. While the X-ray flux increased from MJD 52652 to 52653 by a factor of ~ 2.5, the TeV flux measured at the same time as the X-ray fluxes did not increase substantially. The general trend is that the spectrum hardens as the flux increases, although at MJD 52652.25, the spectrum softens temporarily while the flux is still increasing. Unfortunately, our observations did not cover the decaying phase of the flare.
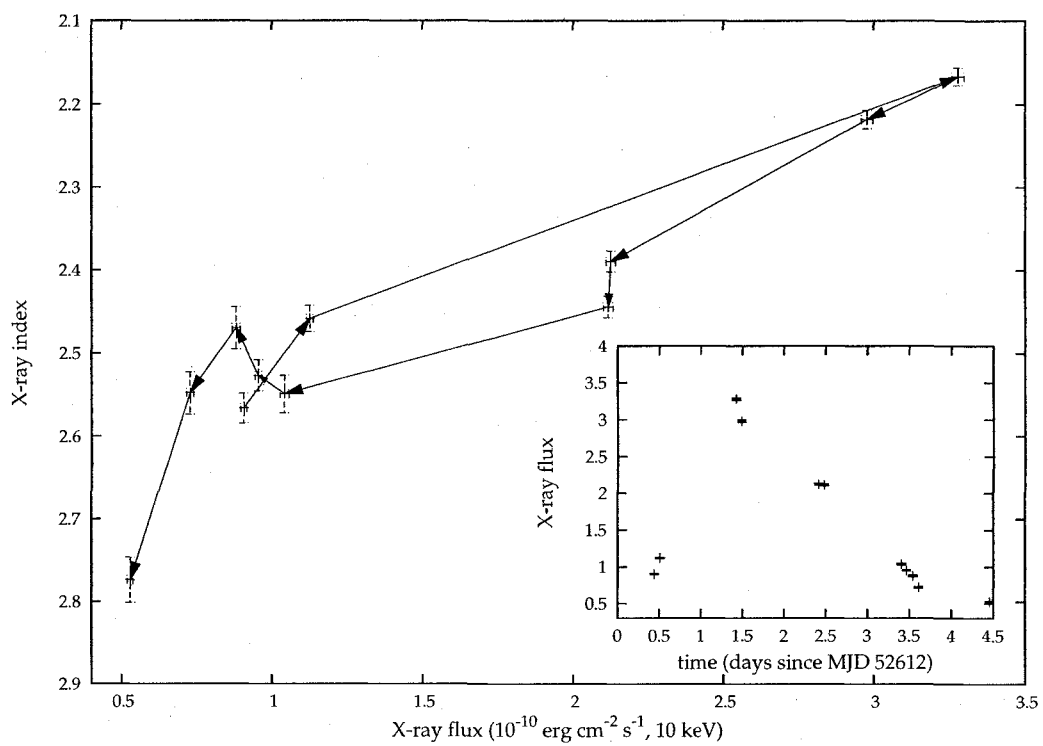
Figure 3.8: X-ray power law spectral index versus X-ray flux for the MJD 52612-52615 X-ray flare.

62
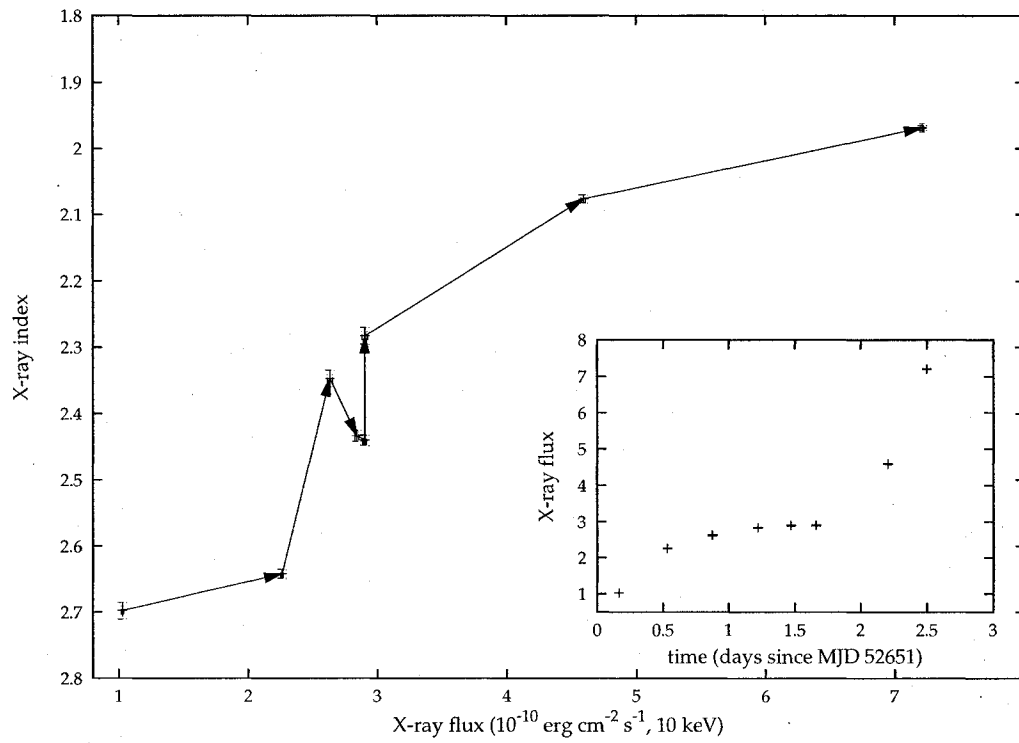
Figure 3.9: X-ray power law spectral index versus X-ray flux for the MJD 52651-52653 X-ray flare.

63

We can also investigate any intrinsic variability time scales in the X-ray and γ-ray data sets by looking at the structure function of each. Figure 3.10 gives the structure function of the X-ray data set. By visual inspection of this structure function, there appears to be a break in the structure function between 0.5 and 2 days. These data were fit with a power law between 0.001 and 2 days, and a horizontal line between 2 and 40 days. The intersection of these two curves is a good measure of the characteristic time of the structure function- it is found to be 0.878 ± 0.04 days. For the TeV γ-ray dataset, no clear break in this structure function is evident. The fact that the γ-ray structure function shows no significant break implies that the sampling is insufficient to resolve the intrinsic variability timescale, and that the light-curve is consistent with white noise.
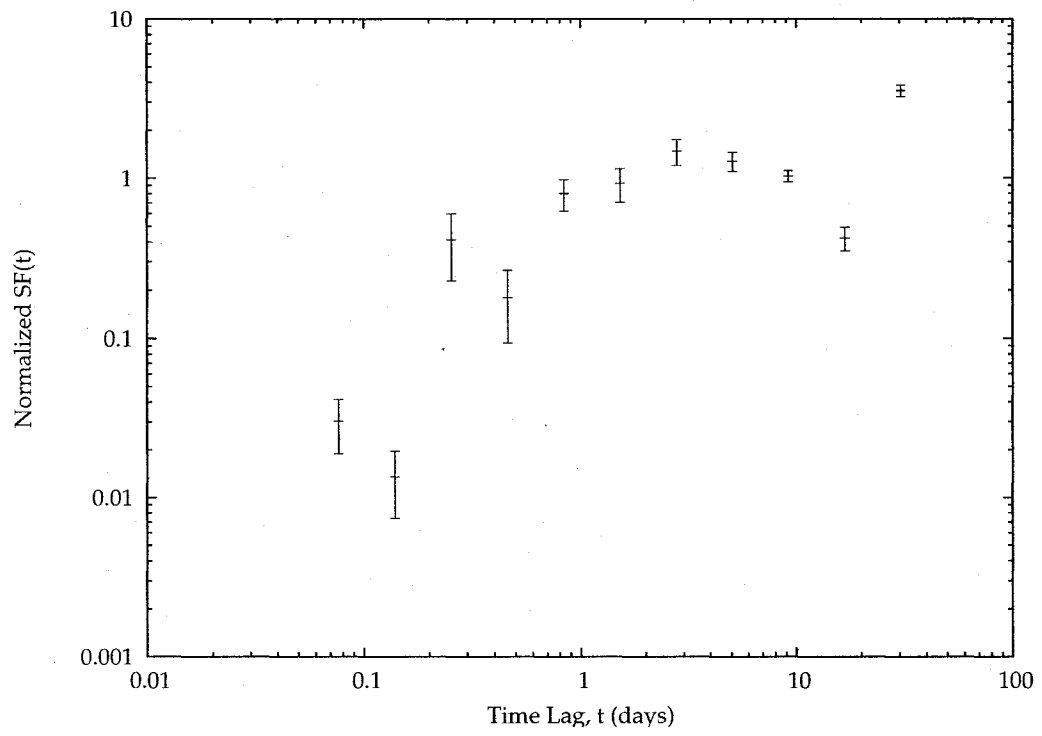
Figure 3.10: X-ray structure function for the entire X-ray dataset.

65

Chapter 4

Synchrotron Self-Compton

Modeling of the Multi-wavelength

Campaign

4.1   A Simple Model for the Acceleration of Electrons in Shocks of AGN Jets

It is commonly assumed that some sort of disturbance in the jet outflow of an AGN produces mildly relativistic shocks which in turn produce the observed broad-band flares. Some form of shock acceleration and synchrotron/inverse-Compton cooling is invoked, however the details of this, even the mechanism by which the flare turns on and off, are poorly understood. Here we consider one of the simplest models to see if

66

we can formulate a self-consistent theory. We assume that blobs traveling with different velocities collide and merge. We further assume that a forward and reverse shock forms in this collision and moves through the blobs with a timescale $\Delta t = R/v_{rel}$. Over this period, we assume that electrons are injected into the shock at a constant rate Q, where they are accelerated by the shock while cooling by synchrotron and inverse-Compton processes. When the blobs merge, and the shocks have moved through the region, we assume that the acceleration stops and the electron population cools, producing the tail of the flare. First order Fermi acceleration (Blandford and Ostriker, 1978) is an excellent candidate for the acceleration process. In this model, as particles traverse a shock they are Lorentz boosted then scatter isotropically, sometimes making it across the shock for another return trip. The resulting energy gain for a roundtrip across and back the shock front is

$$\frac{\Delta E}{E} = \frac{4V_s}{3c} \; ,$$

(4.1)

where V_s is the velocity of the shock front.

First order Fermi acceleration can be incorporated into a "leaky box" model of shock acceleration (Protheroe and Stanev, 1999; Drury et al., 1999) to derive the spectrum of accelerated particles at a given time. By considering conservation of particles, we can write

$$\frac{\partial N}{\partial t} + \frac{\partial}{\partial E}(r_{acc}EN) = Q - r_{esc}N \; ,$$

(4.2)

where, following Protheroe and Stanev (1999), we neglect synchrotron losses. Here, N is the number of particles at a given energy and time, Q is the rate of injection of new particles into the acceleration region, while r_{acc} and r_{esc} describe the rates of particle acceleration and the rate of particles leaving the acceleration region, respectively. The second term in equation 4.2 is the term that describes the shock acceleration of particles in the "leaky box" and how particles of lower energies are boosted to higher energies. In general this term should also describe the loss of energy by particles, and the flux from higher to lower energies.

The energy gain rate is

$$\frac{dE}{dt} = r_{acc}E \ .$$

(4.3)

To accurately describe the acceleration of electrons in jets, we must also account for energy losses due to synchrotron radiation. This is easily done by noting that the energy loss rate of synchrotron radiation is proportional to E^2. Therefore equation 4.3 can be updated to take into account synchrotron losses,

$$\frac{dE}{dt} = r_{acc}E - aE^2 \ ,$$

(4.4)

where a is the synchrotron loss constant. To introduce synchrotron energy losses into the leaky box model, we must replace r_{acc} in equation 4.2 with $r_{acc} - aE$.

I assume that the rate of particles escaping the acceleration region r_{esc} is equal to the rate of particles being accelerated r_{acc}. This assumption is analogous to assuming that the velocities upstream and downstream of the shock are equal. This condition

68

follows for a *strong non-relativistic shock* (Protheroe and Stanev, 1999; Drury et al., 1999).

For the energy dependence of r_{acc}, we take the prescription of Protheroe and Stanev (1999), that the acceleration rate is dependent both on the energy of the particle and the magnetic field:

$$r_{acc} = b \left(\frac{E}{1\mathrm{GeV}} \right)^{-1} \left(\frac{B}{1\mu\mathrm{G}} \right) . \tag{4.5}$$

Here, b ranges between 1.5×10^{-6} and 4×10^{-3} s^{-1}. It is better to determine the various constants from more physically meaningful quantities such as the maximum electron energy, and synchrotron break frequency. We can determine the synchrotron loss parameter a in terms of b if we consider the maximum energy for acceleration in the system. At this maximum energy, synchrotron loss rates will equal acceleration rates, so that $bE_{max}^{-1} = aE_{max}$, so that $a = bE_{max}^{-2}$. This reduces the input into the numerical solution of the leaky box model to one major parameter, the observed maximum energy of electrons. At E_{max}, a characteristic timescale can also be defined such that at the maximum energy, $\tau_0 = 1/r_{acc}$.

Electrons accelerated using the above prescription produce non-thermal spectra that exhibit power law behavior. The spectral index of these non-thermal spectra varies between 2 and 3, and depends on the compression ratio of the shock. Figure 4.1 shows a power-law spectrum of electrons produced using a shock acceleration model. Particles are injected at 10^8eV with a cutoff due to synchrotron cooling at

69
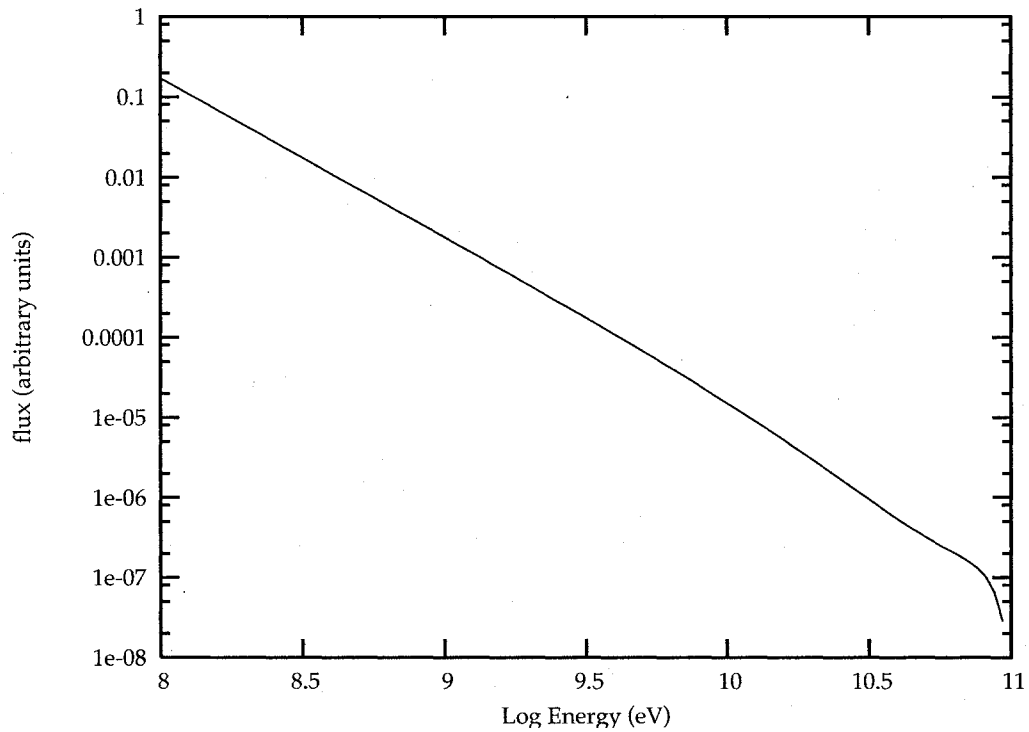
Figure 4.1: Spectrum of electrons having undergone shock acceleration, with synchrotron cooling. Particles are injected at 10^8eV, and are cut off due to synchrotron cooling at 10^{11}eV.

10^{11}eV. Figure 4.2 shows an integrated flux light curve. Particles are injected for $1/5$ of the total evolution time.
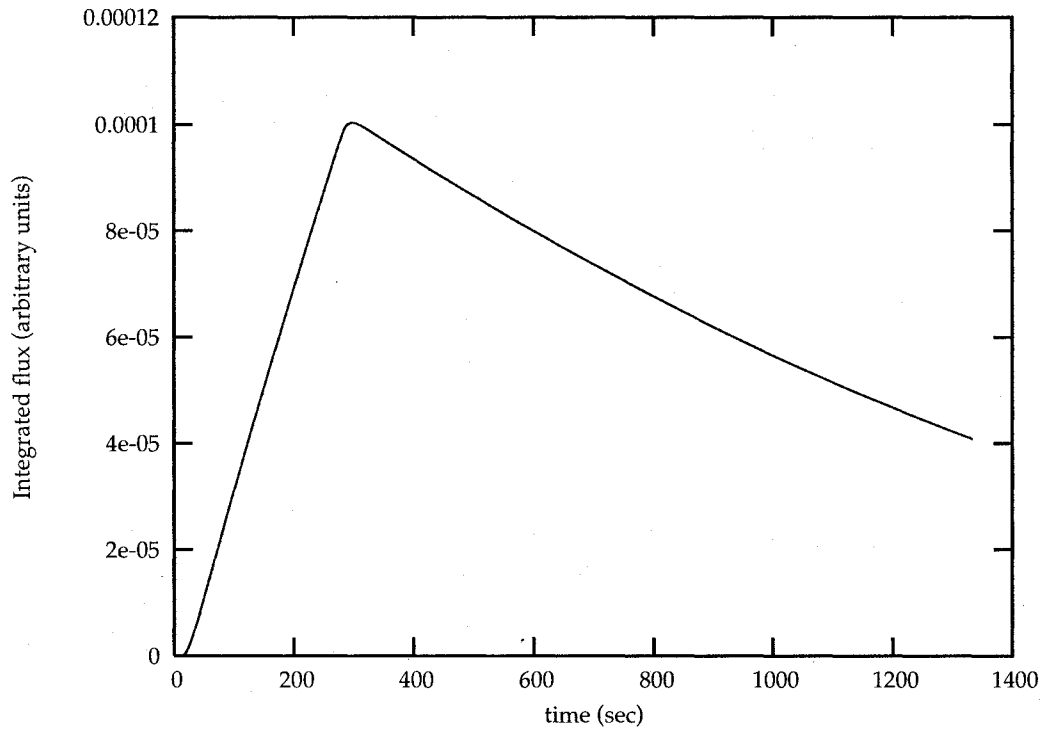
Figure 4.2: Lightcurve of electrons having undergone shock acceleration, with synchrotron cooling. Particles are injected for 1/5 of the total evolution time.

4.2 Synchrotron and Inverse Compton Emission from High Energy Electrons

4.2.1 Theoretical Overview

Emission that is seen in the radio to X-ray band of high-energy-peaked blazars such as Mrk421 is due to synchrotron radiation. Emission in the γ-ray band for blazars such as Mrk421, is widely believed to result from inverse Compton scattering of low energy photons up to TeV γ-ray energies, however proton-induced cascades and other mechanisms can not be ruled out at present. In what follows we concentrate on the leptonic models which have the widest support for blazars such as Mrk421. The following gives a short description of these two radiation processes. We consider here emission in the jet frame.

Synchrotron Radiation

Synchrotron radiation results from a relativistic particle radiating due to acceleration in a magnetic field. This qualitative discussion mirrors that of Rybicki and Lightman (1979). This is a generalization of the non-relativistic case with the distinction that, for relativistic particles, a majority of the radiation is beamed within a cone of half angle $1/\gamma$ about the velocity vector of the particle and timescales are dilated by a further factor of γ. This extreme beaming accounts for most of the behavior seen in synchrotron radiation. An observer viewing a particle undergoing

72

synchrotron radiation will see pulses of radiation, due to relativistic beaming. By Fourier transforming the time domain signal of a narrow beam repeatedly sweeping past the observer, one obtains the spectral characteristics. The duration of these pulses depends on the gyration frequency of the particle in the magnetic field, the pitch angle of the particle with respect to the magnetic field, and this $1/\gamma$ factor. Accounting for the fact that, according to the observer, the particle has moved some distance in its trajectory while emitting towards the observer, the length in time of the pulse is approximately

$$\Delta t \sim \frac{1}{\gamma^3 \omega_B \sin \alpha} \ . \tag{4.6}$$

Here, $\gamma \gg 1$ is the electron Lorentz factor, $\omega_B = \gamma mc/qB$ is the gyrofrequency of the electron, and α is the pitch angle. In the frequency domain, we see that much of the power will be emitted at the critical frequency

$$\omega_c = \frac{3}{2\Delta t} = \frac{3\gamma^2 qB\sin\alpha}{2mc} \ . \tag{4.7}$$

The power emitted per unit frequency for each electron is

$$P(\omega) = \frac{\sqrt{3}}{2\pi} \frac{q^3 B\sin\alpha}{mc^2} F\left(\frac{\omega}{\omega_c}\right) \ . \tag{4.8}$$

Here, q is the charge of the electron, m is the mass of the electron, $F(x) \sim x^{1/3}$ for $x \ll 1$, and $F(x) \sim e^{-x}\sqrt{x}$ for $x \gg 1$. Integrating over frequency, the total power radiated per electron is

73

$$P_{tot} = \frac{4}{3}\sigma_T c\gamma^2 \beta^2 U_B \;, \tag{4.9}$$

where σ_T is the Thomson cross section, $\beta = \mathrm{v}/\mathrm{c}$ is the speed of the electron, and

$U_B = B^2/8\pi$ is the magnetic energy density.

The preceding discussion can be applied to an ensemble of electrons, if one assumes

that the electrons form a power law in energy, $N(E)dE \propto E^{-\alpha}dE$, and are not coherent.

This electron spectrum can be folded with the kernel function given in equation 4.8.

Noting from equation 4.7 that $\omega_c \propto \gamma^2$, and that the dependence upon γ occurs only

in the function F, we find that

$$P_{tot}(\omega) \quad \propto \quad \int_{\gamma_1}^{\gamma_2} F\left(\frac{\omega}{\omega_c}\right)\gamma^{-\alpha}d\gamma \tag{4.10}$$

$$\propto \quad \omega^{-(\alpha-1)/2} \int_{x_1}^{x_2} F(x)x^{(\alpha-3)/2}dx \tag{4.11}$$

In equation 4.11, we have changed our variables of integration to x, and obtained

the frequency dependence without having to evaluate the dimensionless integral. If

we assume that the energy limits are wide enough, and the integrand is constant, we

find that the total emitted power for a $E^{-\alpha}$ power law distribution of electrons is also

a power law, with index $-(\alpha-1)/2$. A more detailed analysis would show that the

total power per unit frequency is proportional to the magnetic field as $B^{(\alpha+1)/2}$.

Inverse Compton Scattering

Inverse Compton scattering is the process by which photons scatter off of energetic electrons, and in the process gain energy (increasing in frequency) at the expense of the electron. Let us consider the Thomson scattering regime, $\epsilon_0 \gamma \ll mc^2$, where ϵ_0 is the energy of the photon, and γ is the Lorentz factor of the electron. The total power transfer from electron to photon for Compton scattering is

$$P_{compton} = \frac{4}{3}\sigma_T c \gamma^2 \beta^2 U_{ph} \ , \tag{4.12}$$

where U_{ph} is the photon energy density and γ is the electron Lorentz factor. Comparing this to equation 4.9, we see that for one electron, the ratio of total power in synchrotron radiation to the total power in inverse Compton scattering is just $U_{\mathrm{B}}/U_{\mathrm{ph}}$, or the ratio of magnetic energy density to the energy density of the seed (Comptonized) photons. For a power law distribution of electrons that was introduced earlier, the radiated power per unit wavelength is once again obtained by folding the Thomson or Klein-Nishina kernel with the electron distribution (Rybicki and Lightman, 1979)

$$P(\omega) \propto \epsilon_1^{-(\alpha-1)/2} \int \int \epsilon^{-(\alpha-1)/2} v(\epsilon) \mathrm{d}\epsilon \, \mathrm{d}V \ . \tag{4.13}$$

Here, ϵ is the incident photon energy, ϵ_1 is the outgoing photon energy, and $\mathrm{v}(\epsilon)$ is the number density of incident photons. In the Thomson regime, inverse Compton scattering of a power law distribution of electrons with $dN/dE \propto E^{-p}$ also results in a power law, with index $(p-1)/2$. This index is the same as the result for synchrotron

radiation.

4.2.2 Multi-wavelength Emission from a Power-Law Distribution of Electrons

Previous observations have shown a reasonable correlation in the X-ray and γ-ray states when Mrk421 is in an active state (Buckley et al., 1996; Jordan and The VERITAS Collaboration, 2001). This multi-wavelength campaign showed Mrk 421 to be in a level of intermediate activity compared to previous observations. During the observational campaign, Mrk 421 showed significant flux variability in the radio, optical, X-ray and γ-ray bands and significant spectral variability at X-rays and TeV γ-rays . While we measured an average TeV γ-ray photon index of $\Gamma = 2.8$, the observations revealed evidence for spectral variability on a time scale of days. The shortest timescale observed for Mrk421 corresponds to a doubling time of $\sim 15-30\text{min}$ Gaidos et al. (1996). In particular, the data suggest very soft γ-ray energy spectra with $\Gamma \approx 4$ during the first half of the observation campaign. One of the most interesting results from this campaign is that the X-ray and TeV γ-ray fluxes are correlated on the $\sim 97\%$ confidence level, but also that we find widely different TeV γ-ray fluxes for a single X-ray flux and vice versa. The most extreme example is the "orphan X-ray flare", seen on January 13, 2003 (MJD 52653). The loose X-ray/TeV correlation may suggest that the model parameters (e.g. the volume of the emission zone) change with time, or that the commonly made assumption of a

single synchrotron self-Compton (SSC) emission zone, presented below, is an over-simplification. Previous observations of Mrk 421 had already shown a rather loose X-Ray/TeV γ-ray correlation (Blazejowski et al., 2005) and the same applied for 1ES 1959+650 (Krawczynski, 2004). In the case of Mrk 501, a rather tight correlation has been reported (Krawczynski et al., 2000, 2002).

The X-ray and TeV γ-ray emission from Mrk 421 data have been modeled with Synchrotron Self-Compton (SSC) codes by many groups (see Inoue and Takahara (1996); Bednarek (1997); Bednarek and Protheroe (1999); Bottcher et al. (1997); Mastichiadis and Kirk (1997); Tanihata et al. (2001); Krawczynski et al. (2001); Konopelko et al. (2003); Kino et al. (2002); Blazejowski et al. (2005)). A crucial model parameter is the jet Doppler factor δ_j . The TeV spectrum constrains the maximum electron Lorentz factor since $\gamma m_e c^2$ must be greater than $E_{\mathrm{max,observed}}$. The maximum synchrotron energy constrains the product $\gamma^2 B$. Given the observation of $E_{max} >\sim 1\mathrm{TeV}$, one typically requires $B <\sim 1\mathrm{G}$.

By observing other parameters of the resulting SSC fits, one can develop constraints on variables in this problem. First consider the locations of the synchrotron and inverse-Compton peak. If the frequency at which the synchrotron spectrum is maximum is ν_S, and the frequency at which the inverse-Compton spectrum is maximum is ν_C, the location of each of the two peaks can be related to each other through

77

the break electron Lorentz factor (Tavecchio et al., 1998),

$$\nu_C \simeq \frac{4}{3}\gamma_{\mathrm{br}}^2 \nu_S \; . \tag{4.14}$$

The location of the IC peak is proportional to the location of the synchrotron peak, and the square of the break electron energy. The location of these two peaks can also be related to magnetic field strength and jet Doppler factor by

$$B\delta \simeq (1+z)\Big(\frac{\nu_S^2}{2.8 \times 10^6 \nu_C}\Big) \; , \tag{4.15}$$

for B in Gauss, and both frequencies in Hertz. Here, we see that for a fixed location of both the synchrotron and IC peaks, the Doppler factor and magnetic field strength are inversely proportional.

Relations also exist between the observed total luminosities of the synchrotron and IC peaks. First, the ratio of the total luminosities are equal to the ratio of the radiation and magnetic field energy densities in the comoving bulk frame (Tavecchio et al., 1998),

$$\frac{L_S}{L_C} = \frac{U'_{rad}}{U'_B} \; , \tag{4.16}$$

where primed variables are in the bulk frame. The total luminosities are not easily observable quantities, due to sparse data coverage across all wavebands, but the peak luminosities are more easily measured. The peak luminosity of both the synchrotron and IC curves are related by

$$B\delta^3 \propto (1+z)\sqrt{\frac{2(\nu_S L_S)^2}{c^3 t_{var}^2 \nu_C L_C}} \; , \tag{4.17}$$

78

where t_{var} is the variability timescale for emission. We see that the peak luminosity and the location of that peak for both the synchrotron and IC emission constrain the magnetic field and Doppler factor of the emission region.

In this discussion we do not want to embark on comprehensive modeling of the data from the entire campaign; due to limited γ-ray statistics, we were unable to perform detailed SED modeling throughout the campaign. What follows is a time averaged analysis over the entire campaign. The main aim is to draw attention to a single remarkable fact: while it is difficult to model the data with Doppler factors on the order of 20 and lower, much higher Doppler factors cannot be excluded.

We modeled the data with the one-zone synchrotron self-Compton code of Krawczynski (2004). The code assumes a single spherical emission volume of radius R relativistically approaching the observer with a jet Doppler factor δ_j. The emission volume is homogeneously filled with a tangled magnetic field of strength B and a non-thermal population of electrons with number density n_e. The electron energy spectrum follows $dN/d\gamma \propto \gamma^{-p}$ with $p = 2$ for electron Lorentz factor γ between γ_{min} and γ_{break}, and with $p = 3$ between γ_{break} and γ_{max}. This break energy occurs because of synchrotron losses modifying the electron energy spectrum. When the timescale for synchrotron losses matches the timescale for acceleration, this break occurs. If no break energy is specified, a power law spectrum with $p = 2$ is generated between γ_{min} and γ_{max}. The code models extragalactic absorption owing to the $\gamma_{TeV} + \gamma_{CIB} \rightarrow e^+ e^-$ pair-production processes of TeV photons on photons from the Cosmic Infrared Background (CIB)

79

using the CIB model of Kneiske et al. (2002).

We fit the data for 5 values of the jet Doppler factor; $\delta_j = 20$, 50, 100, 500, and 1000. For these five values, fits were produced using both a broken power law with break energy E_{break}, and power laws with no break energy. The model parameters for the fits with no break energy are given in Table 4.1, while model parameters for the fits with a break energy are given in Table 4.2. Figures 4.3 to 4.6 show the SSC models with no break in the electron energy spectrum. Figures 4.7 to 4.10 show the SSC models with a break in the electron energy spectrum. All models sucessfully model the X-ray component. As a consequence of synchrotron self-absorption, all of the models presented fail to predict the radio fluxes. The implication is that relatively large emission regions (located further downstream than the emission region that gives rise to the X-ray and γ-ray emission) contribute to the radio flux. The models also underpredicts the optical fluxes; the optical data may include additional flux contributions from downstream jet regions, thermal emission from the accretion region, in addition to a known contribution from the host galaxy.

Figures 4.3 to 4.10 also show the spectral energy distribution of Mrk 421 together with the simple synchrotron self-Compton fits to the data from the campaign. At radio, optical and γ-ray frequencies the mean fluxes measured during the campaign are given. Three *RXTE* X-ray energy spectra are shown corresponding to different flux levels - the minimum, maximum, and average flux value over the campaign. The solid curved lines show, for comparison, a beautifully detailed low-flux and high-flux

δ_j	B (G)	R	$\log \gamma_{min}$	$\log \gamma_{max}$	U_B	U_{part}	$\frac{U_{part}}{U_B}$	L_k	Fig.
20	0.35	1.35	2.3	5.4	4.88×10^{-3}	0.3	61.5	2.09	4.3
50	0.09	1.7	2.3	5.4	3.23×10^{-4}	0.08	247.7	5.47	4.3
100	0.35	.18	2.3	5.0	4.88×10^{-3}	0.7	143.7	2.2	4.4
500	0.6	.005	2.1	4.5	1.43×10^{-2}	45	3147	2.65	4.5
1000	0.5	.0019	2.3	4.4	9.96×10^{-3}	100	1×10^4	3.23	4.6

Table 4.1: Parameters for the 5 synchrotron self-Compton model fits without a break in the electron spectrum. δ_j is the relativistic Doppler factor, B is the magnetic field, in Gauss, R is the size of the emission region, in 10^{13}meters, γ_{min} and γ_{max} are the minimum and maximum Lorentz factors for the primary electron energy spectrum, U_B and U_{part} are energy densities in units of erg cm^{-3}, and L_k is the minimum kinetic luminosity (defined in section 5) in units of 10^{43} erg s^{-1}. The figure number for each of these fits is also shown.

energy spectrum measured with *BeppoSAX* ("Beppo" Satellite per Astronomia X) during the 1998 flaring period (Fossati et al., 2000).

Figures 4.11 to 4.18 show the inverse Compton model predictions in the TeV γ-ray regime, and compares them to the Whipple data. Figures 4.11 to 4.14 show fits with no break in the electron spectrum, while figures 4.15 to 4.18 are fits with a break in the electron energy spectrum. While the model with $\delta_j = 20$ produces a TeV energy spectrum that is softer than the observed one, the other models with higher Doppler
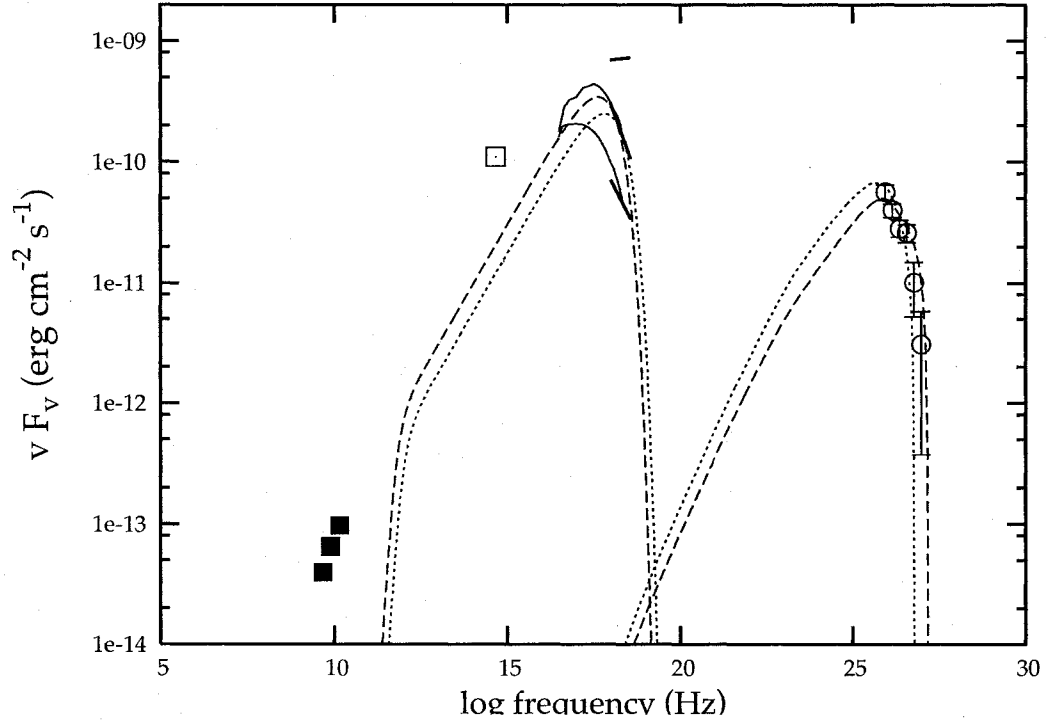
Figure 4.3: Mrk 421 Spectral Energy Distribution from this campaign. The filled squares show the radio data, and the open square shows the optical data. The curved solid line is Bepposax data Fossati et al. (2000). The bold solid lines show X-ray spectra from this campaign - the minimum, average, and maximum fluxes, along with their respective spectral index. The open circles are Whipple TeV γ-ray data from this campaign. The long dashed lines show the results from a simple Synchrotron Self-Compton model with $\delta = 50$, while the short dashed lines should results with $\delta = 20$.
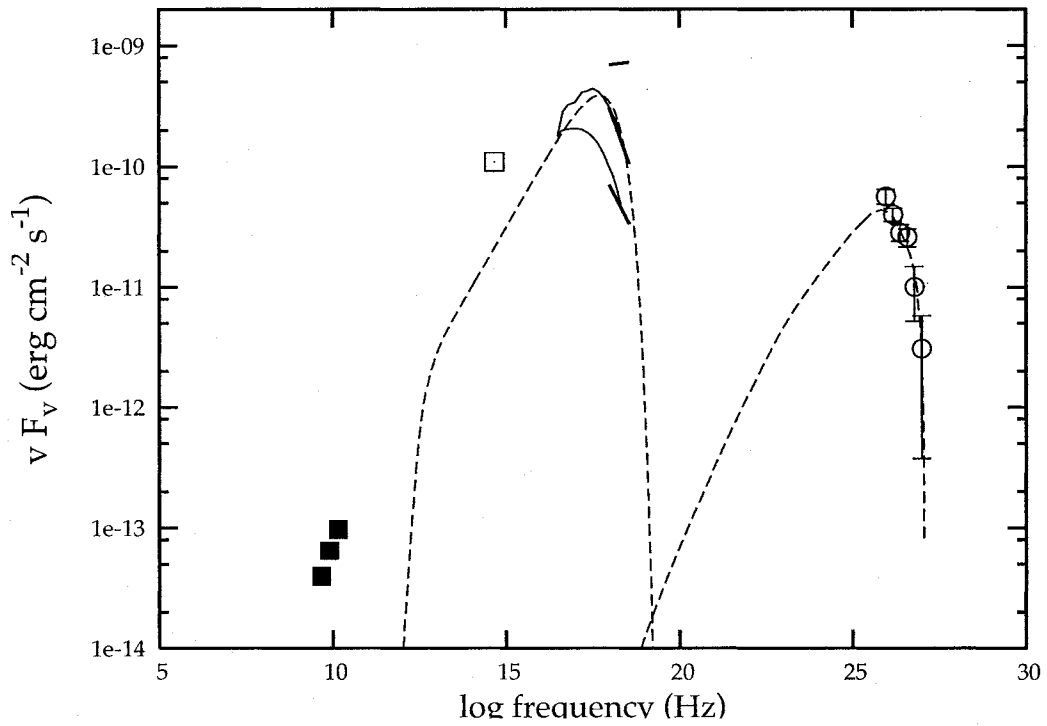
Figure 4.4: Mrk 421 Spectral Energy Distribution from this campaign. The data points are defined in Figure4.3. The long dashed line show the results from a simple Synchrotron Self-Compton model with $\delta = 100$.

Figure 4.5: Mrk 421 Spectral Energy Distribution from this campaign. The data points are defined in Figure 4.3 The long dashed lines show the results from a simple Synchrotron Self-Compton model with $\delta = 500$.

84

Figure 4.6: Mrk 421 Spectral Energy Distribution from this campaign. The data

points are defined in Figure 4.3. The long dashed lines show the results from a simple

Synchrotron Self-Compton model with $\delta = 1000$.

δ_j	B (G)	R	$\log \gamma_{\min}$	$\log \gamma_{\max}$	$\log \gamma_{\text{break}}$	U_B	U_{part}	$\frac{U_{part}}{U_B}$	L_k	Fig.
20	0.62	1.4	2.5	5.3	4.9	1.53	0.2	13.1	1.59	4.7
50	0.22	1.05	3.3	5.3	4.8	0.193	0.08	41.5	1.93	4.7
100	0.2	.32	2.3	5.3	4	0.159	1	629	9.67	4.8
500	0.3	.01	1.5	4.8	3.8	0.358	50	1.4×10^4	11.8	4.9
1000	0.5	.0017	2.8	4.7	3.26	0.996	400	4×10^5	10.9	4.10

Table 4.2: Parameters for 5 synchrotron self-Compton model fits with a break in the electron power law spectrum. δ_j is the relativistic Doppler factor, B is the magnetic field, in Gauss, R is the size of the emission region, in 10^{13} meters, γ_{min}, γ_{max} and γ_{break} are the minimum, maximum, and break Lorentz factors for the primary electron energy spectrum, U_B and U_{part} are energy densities - U_B is in units of 10^{-2}erg cm^{-3}, while U_{part} is in units of erg cm^{-3}, and L_k is the minimum kinetic luminosity (defined in section 5) in units of 10^{43} erg s^{-1}. The figure number for each fit is also given.
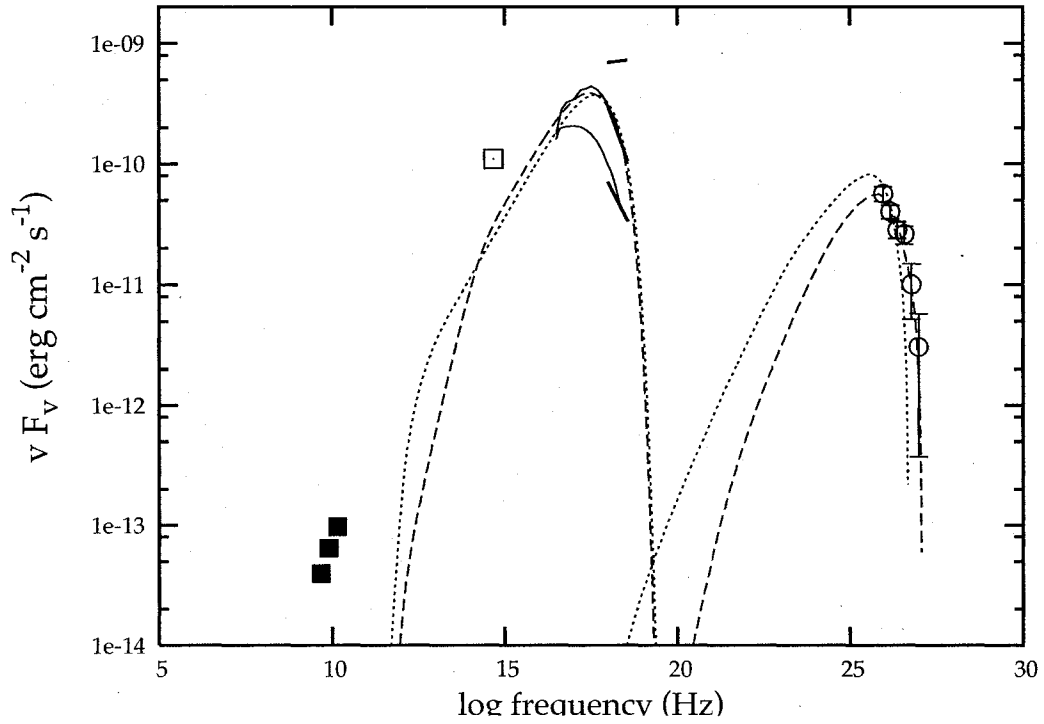
Figure 4.7: Mrk 421 Spectral Energy Distribution from this campaign. The data points are defined in Figure 4.3. These SSC models include a break in the electron energy spectrum. The long dashed lines show the results from a SSC model with $\delta = 50$, while the short dashed lines should results with $\delta = 20$.
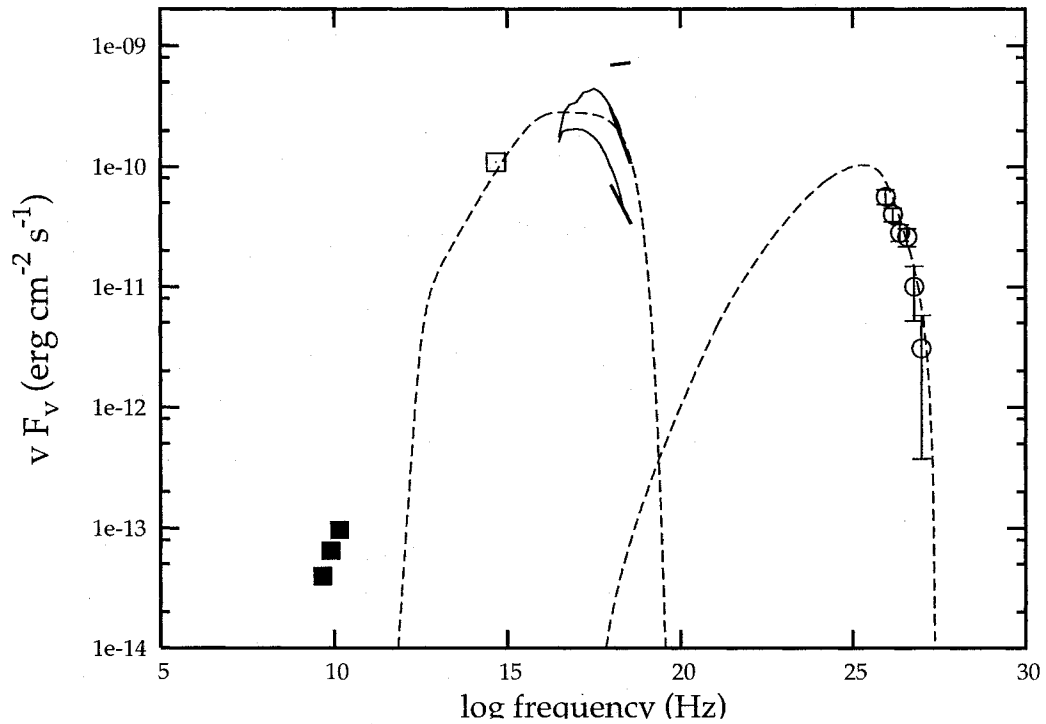
Figure 4.8: Mrk 421 Spectral Energy Distribution from this campaign. The data points are defined in Figure 4.3. These SSC models include a break in the electron energy spectrum. The long dashed line show the results from a SSC model with $\delta = 100$.
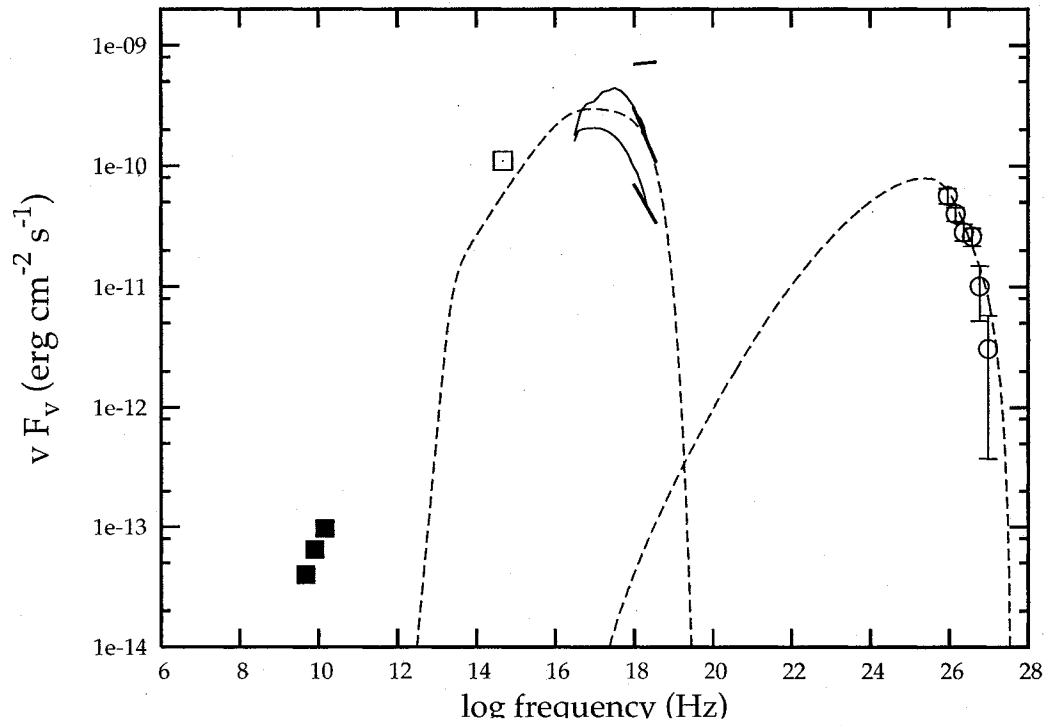
Figure 4.9: Mrk 421 Spectral Energy Distribution from this campaign. The data points are defined in Figure 4.3. These SSC models include a break in the electron energy spectrum. The long dashed line show the results from a SSC model with $\delta = 500$.
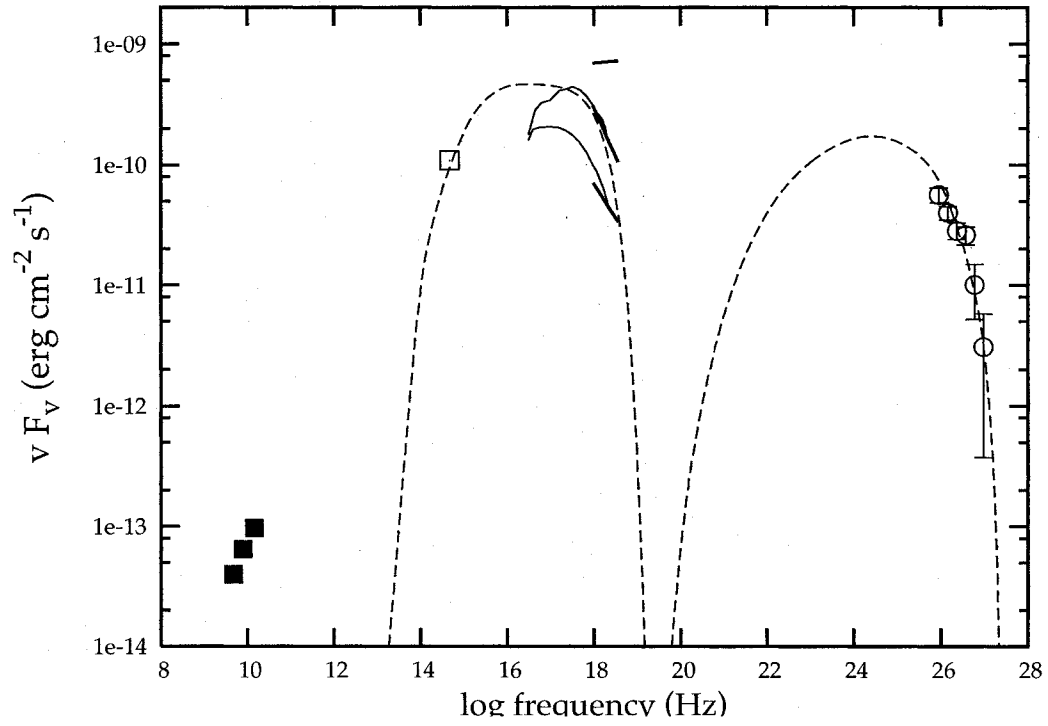
Figure 4.10: Mrk 421 Spectral Energy Distribution from this campaign. The data points are defined in Figure 4.3. These SSC models include a break in the electron energy spectrum. The long dashed line show the results from a SSC model with $\delta = 1000$.

factors describe the TeV data satisfactorily.

In Tables 4.1 and 4.2 we list for the 10 models the magnetic field energy density U_B, the energy density in electrons U_e, the ratio $r = u_e/u_B$, and the kinetic luminosity $L_k = \pi R^2 c \Gamma^2 (u_e + u_B)$ for $\Gamma = \delta_j$ (Begelman et al., 1994). The two pairs of models with lower Doppler factors are closer to equipartition (i.e. $r \sim 1$) between magnetic field and particles, and radiate more efficiently than the extreme model with $\delta_j = 1000$. The kinetic luminosity is very similar for all three models, with the high radiative efficiency of the low-δ_j models making up for the stronger boosting of the high-δ_j models. Taken seriously, the models with $\delta_j = 500$ and $\delta_j = 1000$ would imply that the X-ray and TeV γ-ray emission is produced by an ultra-relativistic particle dominated wind, very close to the supermassive black hole. These high δ_j models also require larger densities of electrons than low δ_j models; they further require smaller emission volumes.

The published models with Doppler factors δ_j of 20 or lower generally predict TeV energy spectra that are softer than the observed ones, especially if a correction for extragalactic absorption is applied, which steepens the energy spectra considerably. Models with Doppler factors δ_j on the order of 50 combined with low magnetic field values give satisfactory model fits to both the X-ray (synchrotron) and the TeV (Inverse Compton) emission (see e.g. Buckley (2001), the self-consistent modeling of Krawczynski et al. (2001); Konopelko et al. (2003) and the discussions by Tavecchio (in press); Piner and Edwards (2005)). Piner and Edwards (2005) also observed the
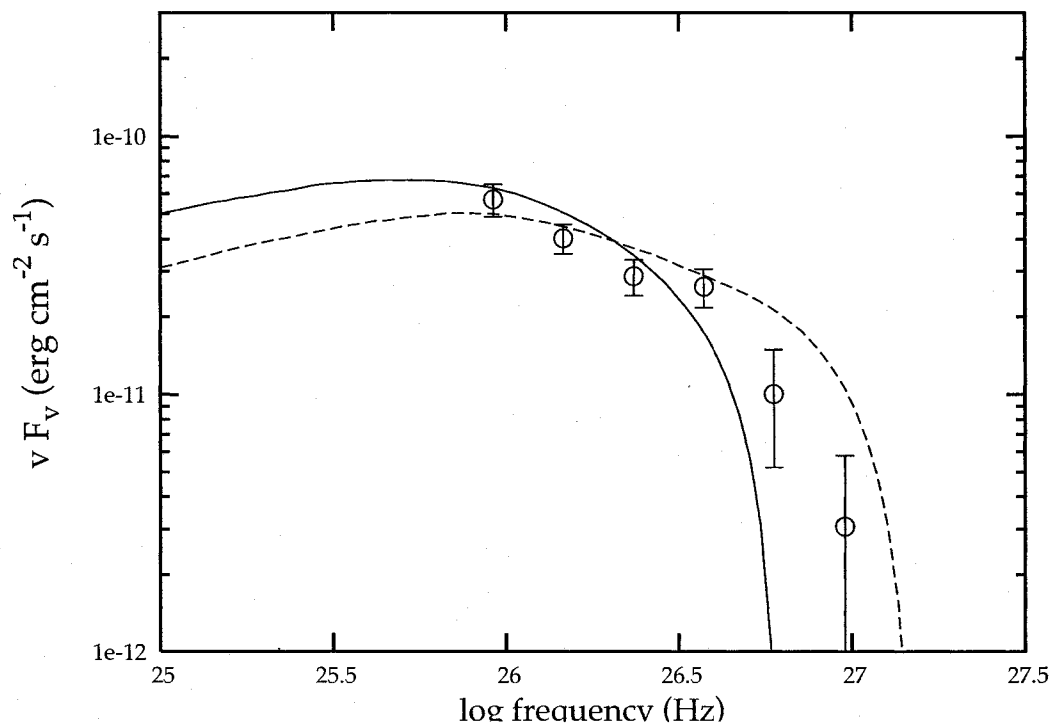
Figure 4.11: Mrk 421 Spectral Energy Distribution in the TeV energy range. The data points are defined in Figure 4.3 The lines show SSC fits for two different values of the jet Doppler factor δ_j, $\delta = 20$ and $\delta = 50$. These fits result from an electron energy spectrum with no break energy.

92
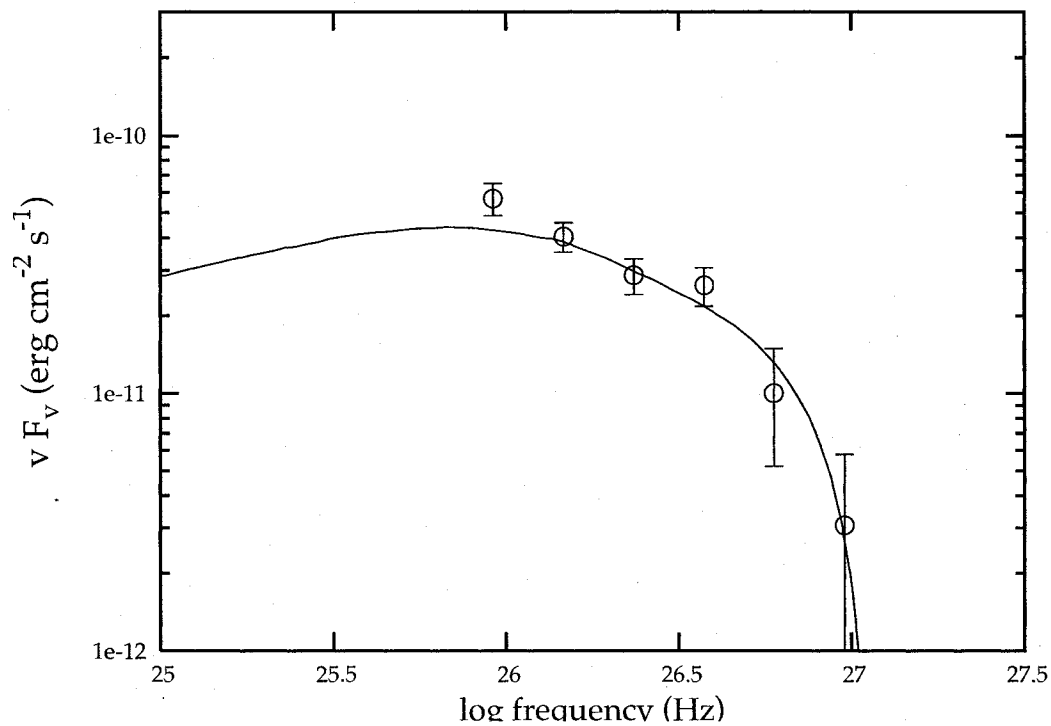
Figure 4.12: Mrk 421 Spectral Energy Distribution in the TeV energy range. The data points are defined in Figure 4.3. The line shows a SSC fit for a value of the jet Doppler factor $\delta = 100$. These fits result from an electron energy spectrum with no break energy.

93
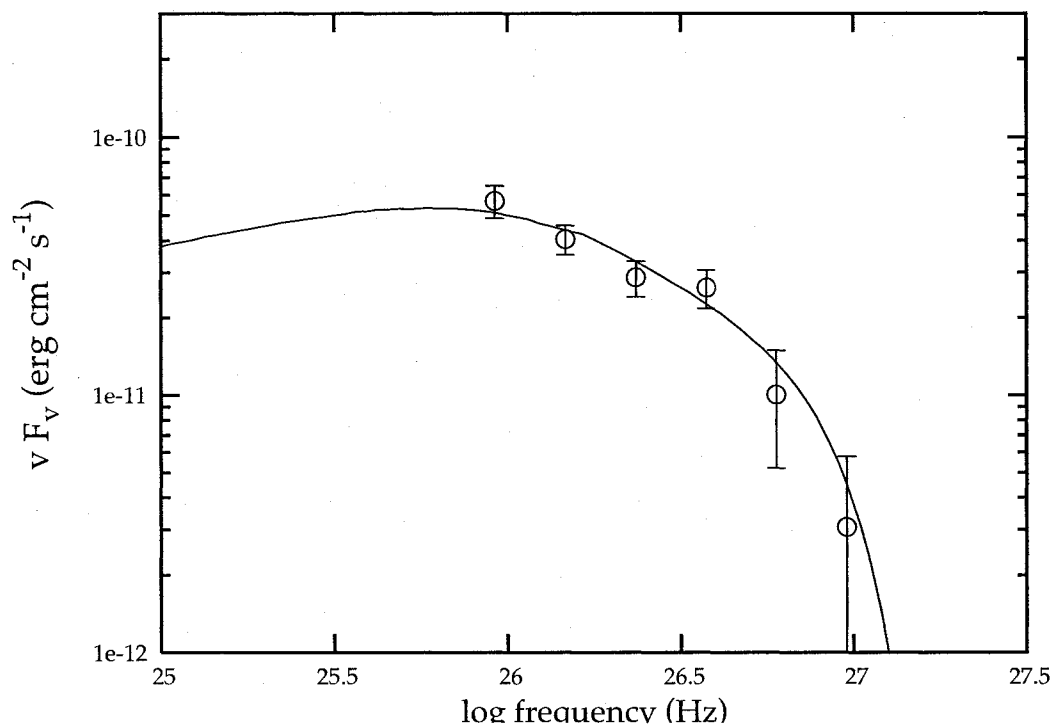
Figure 4.13: Mrk 421 Spectral Energy Distribution in the TeV energy range. The data points are defined in Figure 4.3. The line shows a SSC fit for a value of the jet Doppler factor $\delta = 500$. These fits result from an electron energy spectrum with no break energy.

94
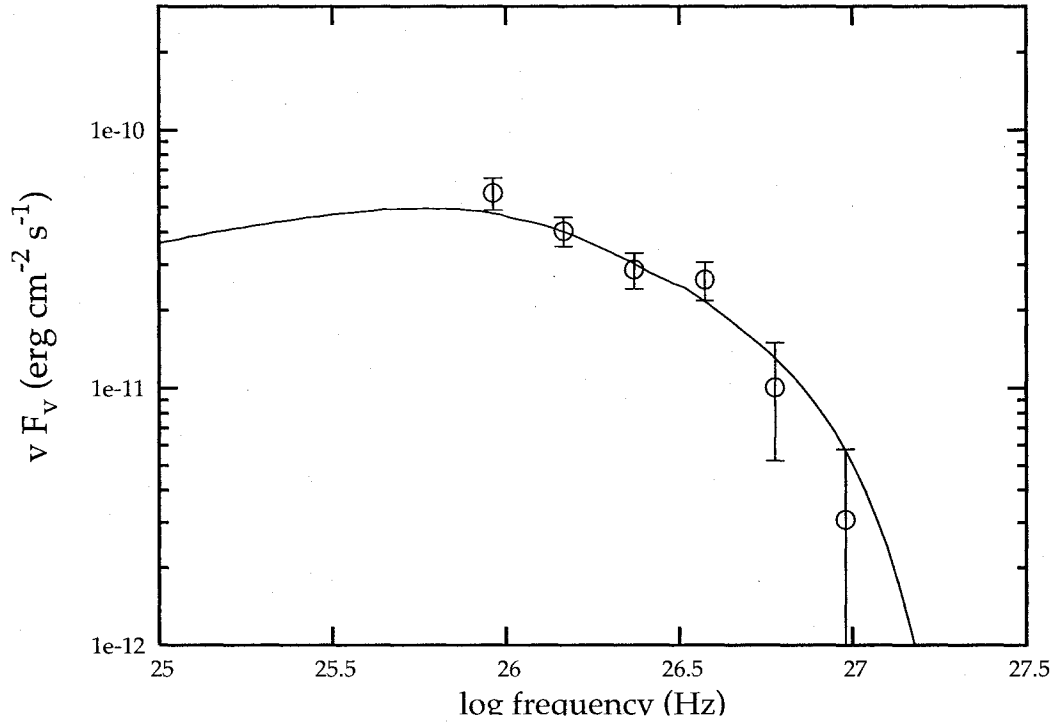
Figure 4.14: Mrk 421 Spectral Energy Distribution in the TeV energy range. The data points are defined in Figure 4.3. The line shows a SSC fit for a value of the jet Doppler factor $\delta = 1000$. These fits result from an electron energy spectrum with no break energy.
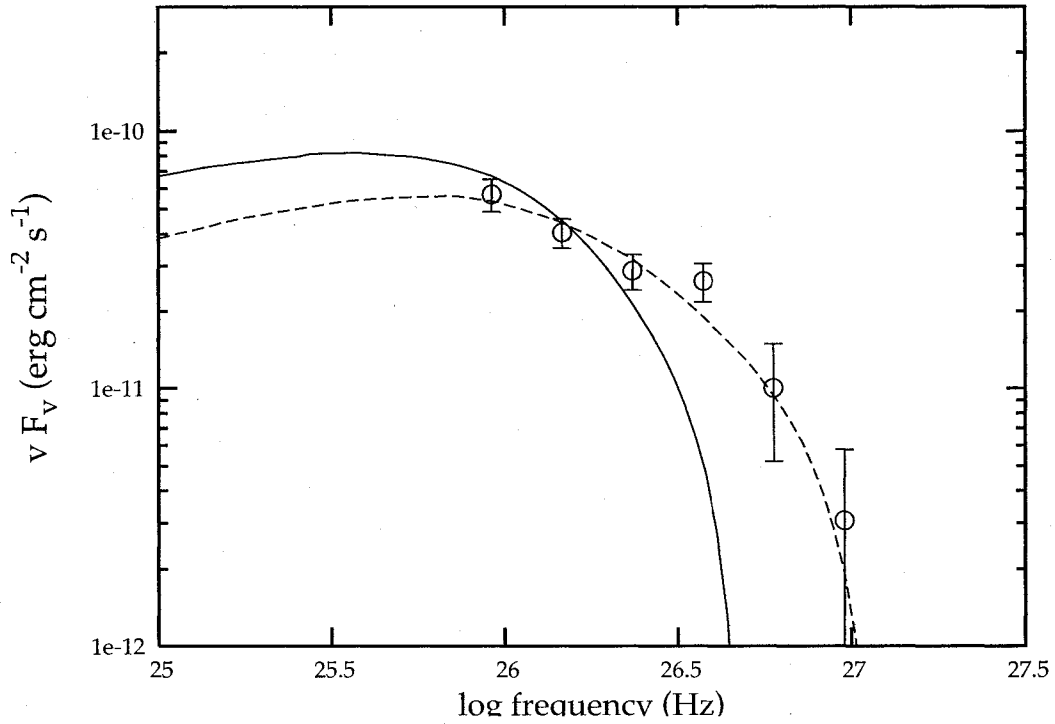
Figure 4.15: Mrk 421 Spectral Energy Distribution in the TeV energy range. The data points are defined in Figure 4.3. The lines show SSC fits for two different values of the jet Doppler factor δ_j, $\delta = 20$ and $\delta = 50$. These fits are a result of a broken electron energy spectrum, at Lorentz factor γ_{break}.
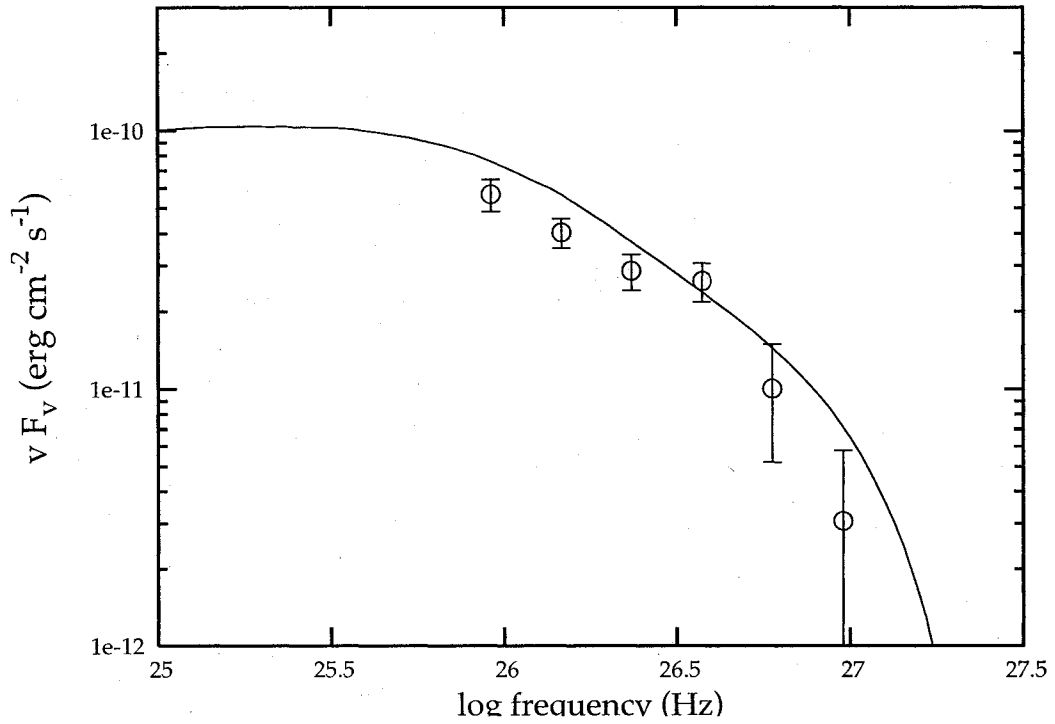
Figure 4.16: Mrk 421 Spectral Energy Distribution in the TeV energy range. The data points are defined in Figure 4.3. The line shows a SSC fit for a different value of the jet Doppler factor $\delta = 100$. This fit are a result of a broken electron energy spectrum, at Lorentz factor γ_{break}.

97
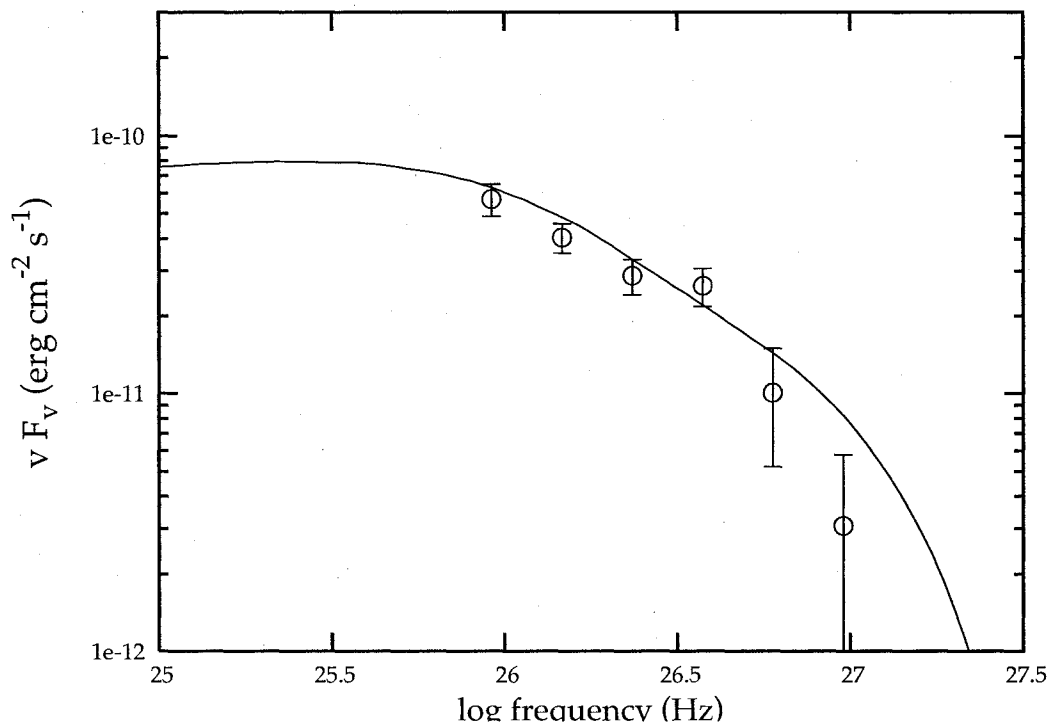
Figure 4.17: Mrk 421 Spectral Energy Distribution in the TeV energy range. The data points are defined in Figure 4.3. The line shows a SSC fit for a different value of the jet Doppler factor $\delta = 500$. This fit are a result of a broken electron energy spectrum, at Lorentz factor γ_{break}.

98
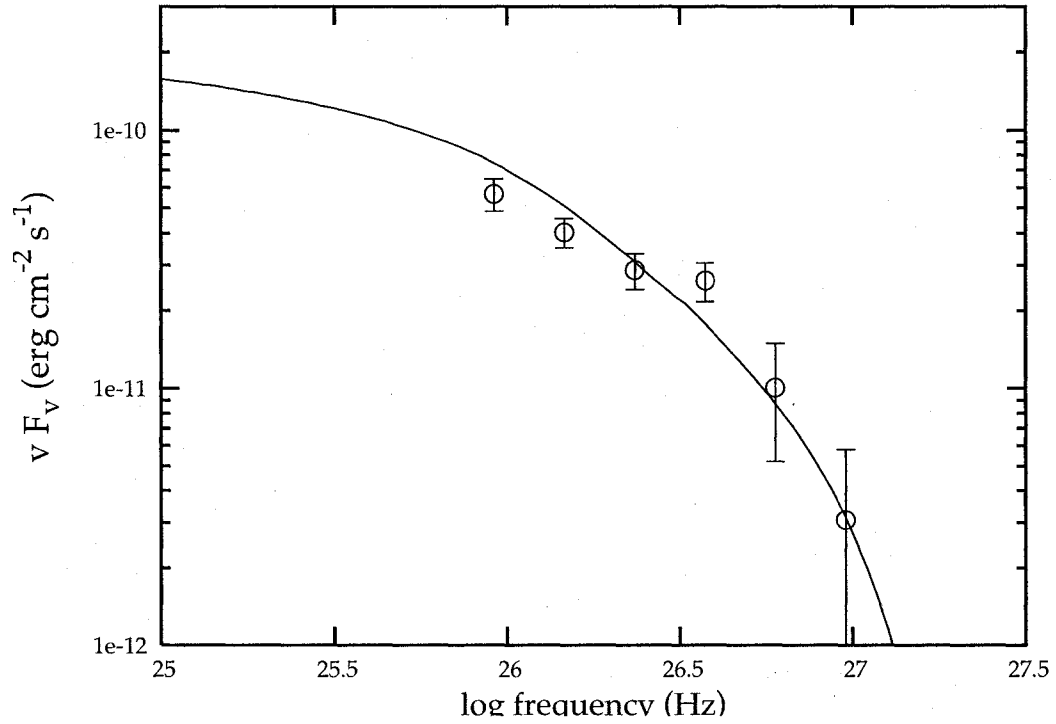
Figure 4.18: Mrk 421 Spectral Energy Distribution in the TeV energy range. The data points are defined in Figure 4.3. The line shows a SSC fit for a different value of the jet Doppler factor $\delta = 1000$. This fit are a result of a broken electron energy spectrum, at Lorentz factor γ_{break}.

99

radio emission of Mrk 421 parsec-scale radio jet with the Very Large Baseline Array (VLBA). Remarkably, they find apparent pattern speeds of only $\sim 0.1c$, an incongruous result if the bulk Lorentz factor of the jet $\Gamma \sim \delta$ is really ~ 50. As discussed by the authors, the highly relativistic motion inferred from TeV observations can be reconciled with the modestly relativistic flow calculated from VLBA observations by postulating that the jet slows down between the sub-parsec (TeV) and parsec (VLBA) regimes. It may be possible to describe the multi-wavelength data with a synchrotron-Compton model and lower Doppler factors by invoking additional seed photons. Buckley (2001) pointed out the possibility that Mrk421 was a transitional object between the LBL and HBL classes, and that a combined SSC and external Compton model with a large Doppler factor ($\delta \sim 100$) could describe the observed spectra. Two new model variants that combine ingredients of SSC and external Compton have been proposed by Georganopoulos and Kazanas (2003), and by Ghisellini et al. (2005). While the first authors assume that downstream emission regions provide seed photons, the second authors speculate that the jet is composed of a fast spine with a slow-moving envelope. In this model, the fast spine emits the X-ray and γ-ray radiation. Given the similar kinematic luminosity of our three models, it may be as hard to slow down a low-δ_j jet as a high-δ_j jet.

Unfortunately, the current observations will not allow us to decide between the many different model variants. We hope that the new generation of Cherenkov telescopes (H.E.S.S., MAGIC, VERITAS and CANGAROO) will break many model de-

generacies. A key will be to measure correlated evolution of the energy spectra in both

the X-ray and the γ-ray energy bands with better spectral and temporal coverage.

Chapter 5

Discussion and Future Work

5.1 Discussion

Since this Mrk421 multi-wavelength campaign occurred during a period of inter-
mediate flux activity, new results were obtained that differ in several important
ways compared with previous multi-wavelength data, taken almost exclusively when
Mrk421 was in a very high flux state. In particular, a time-series analysis of the multi-
wavelength data revealed an "orphan" X-ray flare near the end of the campaign; the
X-ray flux increased by more than a factor of 2 over two days, with no correspond-
ing increase in the TeV γ-ray flux. "Orphan" flares such as these are not simply
explained with conventional one-zone SSC models. In these simple models, one ex-
pects to see any increase in synchrotron (X-ray) flux to be followed by an increase in
inverse-Compton (γ-ray) flux. An increase in X-ray flux without an increase in γ-ray
flux suggest that more complicated models are required to explain observed data. In

102

multi-zone models, it is possible to produce synchrotron radiation corresponding to the X-ray flux seen in our case, in one acceleration region in the jet, while the inverse Compton emission may arise in a nearby, but separate emission region. "Orphan" γ-ray flares have been seen in similar sources, such as 1ES1959+650 (Krawczynski et al., 2004). Existence of γ-ray flares without an X-ray counterpart can also be explained with multi-zone SSC models, again by invoking the possibility of synchrotron emission occurring in different region from the inverse-Compton emission. "Orphan" γ-ray flares can also be explained by so-called external Compton models, where some external population of electrons are Inverse Compton scattered, giving rise to γ-ray radiation that has no correlation with synchrotron X-ray radiation. Any such deviation from simple correlated behavior requires models to go beyond the simple one-zone SSC framework. In fact, one zone models can explain the data, but parameters like the radius R have to change.

When we model the time-averaged spectrum from this multi-wavelength campaign using a one-zone SSC model, we see that very large Doppler factors, on the order of 500 and 1000, can also describe the Mrk421 TeV spectrum. For a given variability timescale, Doppler factors can constrain the size of the emission region, since for a comoving radius of the emission region R', a Doppler factor δ and a redshift z,

$$R' < ct_{var}\frac{\delta}{1+z} .$$
(5.1)

The shortest variability timescale ever seen for Mrk421 corresponded to a doubling in flux on a timescale of about 30 minutes (Gaidos et al., 1996). For a variability

timescale of $t_{var} \sim 30$ minutes a redshift $z \simeq 0.031$ and a Doppler factor $\delta \simeq 1000$, this implies that the largest possible emission volume has a radius in the comoving frame of 5.2×10^{14}m. While larger Doppler factors relax the constraint on R', they require smaller emission volumes, so as to keep the overall luminosity constant, and at the level of the TeV γ-ray data.

The spectral shape of high Doppler factor models also changes with increasing Doppler factor. In this thesis we consider the extreme case of $\delta \simeq 1000$ to look for compatibility with the data. Comparing the IC spectra in figure 4.7 (low Doppler factor, with a broken power-law electron spectrum) to the IC spectra in figure 4.10 (high Doppler factor, also with a broken power-law), important distinctions regarding the shape of the spectra arise. First, the $\delta = 1000$ IC spectra has a much broader peak than the IC spectra with $\delta = 20$ and $\delta = 50$. This broad peak is due to the fact that electrons in jets with Doppler factors of around 1000 have at least 10 times to cool, since $\Delta t_{jet} = \Delta t_{obs}\delta$. In addition, larger magnetic fields are required, since $\delta/B = const$ (see Eq. 4.15). These longer cooling times will shift the break energy in the underlying electron spectra, causing the broad peak seen. Along with this broad peak at high Doppler factor, the power-law index gradually increases up to the IC peak luminosity. For low Doppler factor spectra, the power-law index is roughly constant. For all of these models, the TeV γ-ray regime is roughly the same, due to the maximum energy cutoff in the electron energy spectrum. This degeneracy can be broken with measurements in the GeV γ-ray regime.

104

5.2 Future Work

Multiple avenues to acquiring better multi-wavelength coverage and better γ-ray data are emerging. As stated earlier, SSC model degeneracies due to varying Doppler factors can be broken with multi-wavelength campaigns that include coverage in the GeV energy range. GLAST, to be launched in mid 2007, will be a perfect complement to TeV γ-ray observations. Simultaneous measurements of the peak luminosity of the inverse Compton peak and the synchrotron peak will also be a very important tool in the discrimination of emission models, as this would help constrain both the magnetic field strength and Doppler factor of the jet.

Secondly, VERITAS (Weekes et al., 2002), a next generation Atmospheric Cherenkov Telescope, is using updated technology to lower the energy threshold and improve the background rejection by providing stereoscopic information of the air showers with four telescopes. Flash analog to digital converters (FADCs), developed at Washington University, enable us to decrease the integration time of the electronics, and subsequently increase the signal to noise threshold of the system. Stereoscopic measurements of air showers will improve background rejection.

Lastly, high-efficiency photocathodes, also being developed at Washington University, promise quantum efficiencies near 50% in the UV/blue region, which is the region of interest for the atmospheric Cherenkov technique. Currently, we have achieved quantum efficiencies of 40% at 250 nm, with a drop at longer wavelengths. If these

photocathodes are placed inside of a PMT, they make ideal pixels for an ACT. An increase in detection efficiency also increases the signal to noise ratio and reduces the energy threshold. Appendix D is a recent article by our group that concerns production and measurement of these InGaN photocathodes, and represents a significant part of my thesis work.

In conclusion, continued multi-wavelength studies of high-energy peaked blazars such as Mrk421 will continue to provide greater insight into the production of TeV γ-ray radiation from these sources. With the advent of VERITAS and GLAST we expect much more sensitive measurements of time resolved spectra over a broad band - from MeV to 10 TeV energies. Technological advances in detector systems will allow for a further substantial reduction in the energy threshold, filling the gap between ground and space-based measurements, and providing unparalleled effective areas ($\sim 10^4$ - $10^5 m^2$ down to $\sim 100 GeV$), thus increasing the reach of the technique to sources at cosmological distances of a redshift approaching unity. These advances will only help to constrain the possible emission models for these active galactic nuclei.

Appendix A

Whipple 10m Data of Mrk421

Tables A.1 - A.5 give the raw tracking data from Mrk421 taken by the Whipple 10m telescope in December 2002 and Janurary 2003. The tracking ratio was calculated by looking at OFF runs taken on Mrk421 during the same time period. Using these runs, a tracking ratio of $\alpha = 3.43 \pm 0.08$ was calculated. SuperCuts 2000 were used in the cutting of the data. Also noted are the runs that were included in the nightly spectral analysis (which required having an average zenith angle less than 30 degrees) and the runs that were included in the total campaign spectra (requiring zenith angle less than 30 degrees, *and* matching OFF run).

Table A.6 gives the nightly averaged γ-ray data that is presented in Figures 3.3 and 3.4. This data has been normalized to the zenith-angle-dependent Crab Nebula rate, as is described in section 3.1.1 of this dissertation.

run #	MJD	Rate (γ/min)	Error (γ/min)	Zenith (°)	Nightly?	Total?
023161	52612.42588	0.1723	0.3406	38.77	N	N
023162	52612.44597	0.7061	0.3187	33.08	N	N
023164	52612.48818	0.6737	0.4018	21.16	Y	N
023165	52612.50780	0.8598	0.3996	15.81	Y	N
023188	52613.41000	0.3911	0.3408	42.48	N	N
023189	52613.43008	1.2317	0.3325	36.81	N	N
023191	52613.47131	2.1982	0.4130	25.13	Y	N
023192	52613.49172	1.7568	0.2920	19.44	Y	Y
023214	52614.40450	0.3091	0.3236	43.25	N	N
023215	52614.42429	1.0841	0.3866	37.66	N	N
023217	52614.46544	0.4074	0.2503	26.02	Y	Y
023218	52614.48552	1.1131	0.2353	20.39	Y	Y
023265	52615.39780	0.9284	0.4652	44.36	N	N
023236	52615.41818	0.6410	0.4349	38.62	N	N

Table A.1: Whipple 10m data from this multi-wavelength campaign. Shown for each run are the run number, the mean Julian date (MJD) start time of each run, the calculated γ-ray rate, in $\gamma\,\mathrm{min}^{-1}$, the error in the γ-ray rate, the average zenith angle for the run, in degrees, and whether or not the run was used in the night by night spectral analysis, and if it was used in the average spectral analysis.

run #	MJD	Rate (γ/min)	Error (γ/min)	Zenith (°)	Nightly?	Total?
023237	52615.43784	1.3899	0.4512	33.06	N	N
023238	52615.45786	0.6316	0.2907	27.39	Y	Y
023256	52616.43505	0.6713	0.3187	33.07	N	N
023257	52616.45582	0.2006	0.2921	27.20	Y	Y
023259	52616.49853	0.5693	0.4346	15.37	Y	N
023260	52616.51818	1.3098	0.4003	10.54	Y	N
023274	52617.43439	0.4269	0.3244	32.49	N	N
023277	52617.49699	1.2589	0.4399	15.06	Y	N
023286	52618.42058	0.3801	0.3236	35.63	N	N
023288	52618.45935	1.4268	0.4148	24.65	Y	N
023291	52618.50011	0.2887	0.3061	13.55	Y	N
023299	52619.35552	0.8944	0.4182	53.08	N	N
023301	52619.39649	-0.1989	0.2162	41.66	N	N
023304	52619.46519	0.1682	0.4100	22.25	Y	N
023305	52619.48503	-0.0186	0.2914	16.80	Y	Y

Table A.2: Same as table A.1.

109

run #	MJD	Rate (γ/min)	Error (γ/min)	Zenith (°)	Nightly?	Total?
023313	52620.39227	0.0982	0.3580	42.09	N	N
023316	52620.45685	1.2664	0.4257	23.82	Y	N
023317	52620.47653	1.3930	0.4204	18.35	Y	N
023322	52621.37776	-0.2840	0.4040	45.39	N	N
023325	52621.44981	1.0562	0.4247	25.03	Y	N
023333	52622.43321	1.3705	0.3296	28.96	Y	Y
023336	52622.49831	0.9604	0.2694	11.33	Y	Y
023340	52623.44561	0.5643	0.2951	24.68	Y	N
023341	52623.46521	0.1231	0.2643	19.21	Y	N
023342	52623.48723	0.2128	0.1692	13.36	Y	N
023347	52624.49503	2.3939	0.3403	10.83	Y	Y
023439	52639.47185	3.1285	0.4676	7.71	Y	N
023462	52640.43930	3.3506	0.4683	13.74	Y	N
023465	52640.47617	3.4132	0.4850	7.19	Y	N
023490	52641.42167	0.4702	0.4328	17.69	Y	N

Table A.3: Same as table A.1.

110

run #	MJD	Rate (γ/min)	Error (γ/min)	Zenith (°)	Nightly?	Total?
023520	52642.42084	1.1718	0.2712	17.18	Y	N
023545	52643.41296	0.9987	0.3208	18.57	Y	N
023572	52645.37949	3.1908	0.4709	26.40	Y	N
023574	52645.41239	4.9493	0.4831	17.24	Y	N
023575	52645.44737	4.4632	0.4724	8.88	Y	N
023578	52645.48399	4.6312	0.4439	8.63	Y	N
023580	52645.52607	4.1385	0.4283	18.79	Y	N
023591	52646.34500	1.0830	0.4465	35.39	N	N
023592	52646.39637	4.0951	0.4533	20.89	Y	N
023596	52646.42914	2.1797	0.4057	12.20	Y	N
023602	52646.52489	1.8468	0.4457	19.21	Y	N
023605	52647.46430	0.0667	0.0645	7.16	Y	N
023615	52649.43082	2.2364	0.4508	9.96	Y	N
023618	52649.48484	1.9152	0.2670	10.98	Y	Y
023625	52650.41631	1.1288	0.2765	12.67	Y	Y

Table A.4: Same as table A.1.

111

run #	MJD	Rate (γ/min)	Error (γ/min)	Zenith (°)	Nightly?	Total?
023629	52650.48664	0.9023	0.4001	12.03	Y	N
023638	52651.48850	3.3333	0.4408	13.54	Y	N
023640	52651.53201	3.8143	0.3345	25.00	Y	Y
023644	52652.45026	4.1357	0.4571	7.15	Y	N
023645	52652.46976	3.8206	0.4459	9.52	Y	N
023651	52653.46283	3.1378	0.3134	8.75	Y	Y
023654	52653.50604	4.6880	0.4573	19.29	Y	N
023655	52653.52557	4.1599	0.4729	24.74	Y	N

Table A.5: Same as table A.1.

MJD	Rate (Crab)	Error	MJD	Rate (Crab)	Error
52612.46696	0.31036	0.08741	52639.47185	1.35020	0.20180
52613.45078	0.75375	0.08450	52640.45774	1.48355	0.14782
52614.44494	0.41993	0.07222	52641.42167	0.21737	0.20008
52615.42792	0.57669	0.12779	52642.42084	0.53904	0.12475
52616.47690	0.33183	0.07971	52643.41296	0.46582	0.14963
52617.46569	0.40721	0.12928	52645.44986	1.96050	0.09321
52618.46001	0.36033	0.09596	52646.42385	1.11400	0.09640
52619.42555	0.23890	0.10105	52647.46430	0.02872	0.02777
52620.44188	0.44997	0.10086	52649.45783	0.90778	0.10408
52621.41379	0.15000	0.05804	52650.45148	0.44944	0.09636
52622.46576	0.58021	0.10593	52651.51026	1.70730	0.12478
52623.46602	0.14548	0.06229	52652.45026	1.72175	0.13817
52624.49503	1.04920	0.14914	52653.49815	1.88577	0.11210

Table A.6: The averaged nightly γ-ray rates that are shown in figures 3.3 and 3.4. Shown here, for each night, are the average MJD time, the average γ-ray rate, in $\gamma\,\mathrm{min}^{-1}$, and the error on this rate.

113

Appendix B

RXTE PCA Data from Mrk421 during December 2002 and Janurary 2003

114

MJD	Flux ($10^{-10}\,\mathrm{erg\,cm^2\,s^{-1}}$)	Error	Index	Index Error
52610.20889	0.77193	0.006351	2.61	0.01
52610.46907	0.82266	0.008145	2.59	0.02
52610.72092	0.79533	0.013479	2.60	0.03
52611.19092	1.54550	0.010087	2.55	0.01
52611.24991	1.64666	0.014912	2.55	0.01
52611.45583	2.61560	0.014729	2.32	0.01
52611.52342	2.12458	0.016387	2.39	0.01
52612.44120	0.90692	0.010013	2.57	0.02
52612.50759	1.12688	0.010923	2.46	0.02
52613.42842	3.27904	0.019280	2.17	0.01
52613.49435	2.97930	0.018726	2.22	0.01
52614.41518	2.12555	0.015868	2.39	0.01
52614.48129	2.11725	0.016062	2.44	0.01
52615.40898	1.04242	0.014457	2.55	0.02
52615.46861	0.95550	0.011172	2.53	0.02

Table B.1: RXTE PCA X-ray data from this multi-wavelength campaign. Shown here for each run are the MJD start time, the flux, in units of $10^{-10}\,\mathrm{erg\,cm^2\,s^{-1}}$ at 10 keV, the error on this flux, the power-law index Γ, where $dN/dE \propto E^{-\Gamma}$, and the error on the power-law index.

MJD	Flux ($10^{-10}\,\mathrm{erg\,cm^2\,s^{-1}}$)	Error	Index	Index Error
52615.54268	0.88160	0.013538	2.47	0.03
52615.60991	0.72770	0.011592	2.55	0.03
52616.45574	0.52897	0.009301	2.77	0.03
52617.44268	1.18886	0.014124	2.50	0.02
52617.50935	1.38101	0.013508	2.48	0.02
52618.42963	0.51265	0.007992	2.79	0.03
52618.49639	0.59953	0.009434	2.64	0.03
52618.88398	0.70646	0.011120	2.64	0.03
52619.09685	0.71252	0.010411	2.58	0.02
52619.19472	0.67652	0.004309	2.62	0.01
52619.35648	0.55836	0.013429	2.68	0.04
52619.41648	0.47327	0.009695	2.90	0.03
52619.48361	0.60158	0.008696	2.68	0.02
52619.83296	0.44466	0.008499	2.79	0.03
52620.18231	0.33661	0.003142	2.85	0.01

Table B.2: Same as Table B.1.

116

MJD	Flux ($10^{-10}\,\mathrm{erg\,cm^2\,s^{-1}}$)	Error	Index	Index Error
52620.40361	0.54226	0.011542	2.73	0.03
52620.47018	0.48525	0.006954	2.69	0.02
52620.82092	0.36482	0.008504	2.71	0.04
52621.20259	0.33052	0.004486	2.80	0.02
52621.25796	0.39990	0.008090	2.88	0.03
52621.39083	0.42096	0.009958	2.81	0.04
52621.45805	0.65697	0.008027	2.69	0.02
52622.21185	1.40552	0.006784	2.59	0.01
52622.44435	0.96931	0.009194	2.67	0.02
52622.51092	1.14923	0.009784	2.56	0.01
52623.17759	1.74331	0.009090	2.47	0.01
52623.23185	1.66906	0.014129	2.48	0.01
52623.49842	2.04837	0.012778	2.45	0.01
52624.21861	1.04846	0.011913	2.61	0.02
52624.48565	1.97638	0.013041	2.39	0.01

Table B.3: Same as Table B.1.

MJD	Flux (10^{-10} erg cm^2 s^{-1})	Error	Index	Index Error
52649.44102	1.18266	0.015700	2.65	0.02
52649.50120	1.14680	0.015667	2.78	0.02
52649.70583	2.82176	0.014477	2.54	0.01
52650.42954	1.64021	0.012939	2.54	0.01
52650.49565	1.14407	0.012217	2.68	0.02
52650.68833	1.21291	0.012562	2.74	0.02
52651.16537	1.02944	0.007949	2.70	0.01
52651.53370	2.26258	0.009456	2.64	0.01
52651.87824	2.63590	0.019760	2.35	0.01
52652.22120	2.84346	0.014615	2.43	0.01
52652.47213	2.90438	0.014074	2.44	0.01
52652.66250	2.90400	0.021207	2.28	0.01
52653.20750	4.59278	0.016443	2.08	0.01
52653.49972	7.21269	0.015120	1.97	0.00

Table B.4: Same as Table B.1.

Appendix C

Converting from Standard

Astronomical Fluxes to νF_ν Fluxes

In multi-wavelength spectral analysis, it is often useful to plot spectral data from all wavebands on a single figure. So called νF_ν plots are used often in this regard. These plots give power radiated per logarithmic energy interval. νF_ν has (CGS) units of $\mathrm{erg\,cm^{-2}s^{-1}}$ As data from various analyses may have different units, converting each of these to a common system of units require care. In what follows, I outline the method used to convert each data set presented in this dissertation to νF_ν fluxes.

C.1 TeV γ-ray Fluxes

The spectral data points presented here from the Whipple 10m telescope were found using the Washington University Whipple data analysis framework, *wuparam*. They

119

are given as counts $m^{-2}s^{-1}TeV^{-1}$ at 1 TeV. The conversion is as follows:

$$F \, (\text{counts } m^{-2} \, s^{-1} \, TeV^{-1}) = 10^{-4} \, F \, (\text{counts } cm^{-2} \, s^{-1} \, TeV^{-1})$$

$$= (1/1.6) \times 10^{-4} \, F \, (\text{counts } cm^{-2} \, s^{-1} \, erg^{-1})$$

$$\rightarrow E^2 (1/1.6) \times 10^{-4} \, \text{counts } cm^{-2} \, s^{-1} \, erg^{-1}$$

$$= \left(\frac{E}{1TeV} \right)^2 (1.6 \, erg)^2 (1/1.6) \times 10^{-4} \, \text{counts } cm^{-2} \, s^{-1} \, erg^{-1}$$

$$= \left(\frac{E}{1TeV} \right)^2 1.6 \times 10^{-4} \, erg \, cm^{-2} \, s^{-1} \tag{C.1}$$

Here, E is the energy of the particular flux data point being converted, and is in units of TeV.

C.2   X-ray fluxes

Fluxes from the PCA instrument aboard RXTE are in counts $cm^{-2} \, s^{-1} \, keV^{-1}$ at 10 keV. Since all of the fluxes presented here are at 10 keV, the conversion is relatively simple:

$$F \, (\text{counts } cm^{-2} \, s^{-1} \, keV^{-1}) \rightarrow ((10 \, keV)^2 \, cm^{-2} \, s^{-1} \, keV^{-1}$$

$$= 100 \, keV \, cm^{-2} \, s^{-1}$$

$$= 10^2 \times (1.6 \times 10^{-9}) \, erg \, cm^{-2} \, s^{-1}$$

$$= 1.6 \times 10^{-7} \, erg \, cm^{-2} \, s^{-1} \tag{C.2}$$

120

Filter	λ_0 (Å)	f(0) $(\mathrm{erg\,cm^{-2}s^{-1}\mathring{A}^{-1}})$
U	3650	4.27×10^{-9}
B	4400	6.61×10^{-9}
V	5500	3.64×10^{-9}
R	7000	1.74×10^{-9}
I	9000	8.32×10^{-10}

Table C.1: Absolute spectral irradiances for common optical filters. Adapted from Allen (1973).

C.3 Optical Magnitudes

To convert from optical magnitudes in a particular filter band to νF_ν , one must first convert magnitudes to spectral irradiance $(\mathrm{erg\,cm^{-2}s^{-1}\mathring{A}^{-1}})$(Allen, 1973),

$$\log f(m_x) = -0.4m_x + \log f(0) . \tag{C.3}$$

Here, m_x is the magnitude in the particular filter band, $f(m_x)$ is the spectral irradiance for a given magnitude, and $f(0)$ is the absolute spectral irradiance for a magnitude 0 star. Table C.1 gives some common filter bands, and their respective absolute irradiances.

Once the spectral irradiance for a particular filter and magnitude is found, converting to a νF_ν flux requires multiplying by the wavelength of the filter used, in Å. For an R filter measurement, using the absolute spectral irradiance from table C.1,

$$f(m_x) = 1.22 \times 10^{-5-0.4m_x} \ \mathrm{erg\,cm^{-2}s^{-1}} \ . \tag{C.4}$$

C.4 Radio Fluxes

The Radio measurements that are given here are given in a standard unit of spectral irradiance, the Jansky, $1\mathrm{Jy} = 10^{-23}\mathrm{erg\,cm^{-2}s^{-1}Hz^{-1}}$. To convert to a $\nu\,F_\nu$ flux from power measured in Janskys, one must only use this definition, then multiply by the frequency at which the measurement was made,

$$f(1Jy) = \nu \times f\left(10^{-23}\mathrm{erg\,cm^{-2}s^{-1}}\right) \ . \tag{C.5}$$

Here ν is the frequency of the measurment, given in Hertz.

122

Appendix D

High quantum efficiency ultraviolet/blue AlGaN / InGaN photocathodes grown by molecular-beam epitaxy

The following is a paper by Leopold et al. (2005) regarding research by our group into growing high quantum efficiency photocathodes.

123

High quantum efficiency ultraviolet/blue AlGaN/InGaN photocathodes grown by molecular-beam epitaxy

D. J. Leopold
Department of Physics, Washington University, St. Louis, Missouri 63130 and Center for Molecular Electronics, University of Missouri-St. Louis, St. Louis, Missouri 63121

J. H. Buckley[a]
Department of Physics, Washington University, St. Louis, Missouri 63130

P. Rebillot
Department of Physics, Washington University, St. Louis, Missouri 63130

Enormous technological breakthroughs have been made in optoelectronic devices through the use of advanced heteroepitaxial-semiconductor crystal-growth techniques. This technology is being extended toward enhanced ultraviolet/blue single-photon detection through the design and fabrication of atomically tailored heteroepitaxial GaAlN/GaInN photocathode device structures. The AlGaN/InGaN system is ideal because the band gap can be tailored over an energy range from 0.8 to 6.2 eV and epitaxial thin-film layers can be grown directly on optically transparent sapphire substrates. Although a single *p*-type GaN layer activated with cesium can produce reasonably high quantum efficiency in the ultraviolet wave band, a more complex design is necessary to achieve high levels extending into the blue region. In the present work, band-gap engineering concepts have been utilized to design heterostructure photocathodes. The increased level of sophistication offered by this approach has been exploited in an attempt to precisely control photoelectron transport to the photocathode surface. Thin heterostructure layers designed for transmission-mode detection were fabricated by molecular-beam epitaxy. A quantum efficiency of 40% at 250 nm was achieved using a thin, compositionally graded GaN/InGaN layer, epitaxially grown on a sapphire substrate. Further improvements are anticipated through continued optimization, defect reduction, and more complex photocathode designs. © *2005 American Institute of Physics.* [DOI: 10.1063/1.1999026]

I. INTRODUCTION

Photocathode devices operating in the ultraviolet (UV) and blue wave band are important for detection of scintillation and Cherenkov radiation in high-energy physics and astrophysics experiments. These experiments often require plate scales of ~ 1 m^2 or more, nanosecond exposures, high gain, and single-photon counting. These requirements can only be met using vacuum tube electron multipliers. Enhancements in the device quantum efficiency would lead to enormous improvements in single-photon detection statistics. In addition, astronomical imaging applications in the UV could benefit by coupling large-area photocathodes with microchannel plate (MCP) photon counting and two-dimensional readout electronics. Devices such as this would have wide application in high-sensitivity, high-resolution imaging cameras or spectrographs, for observations requiring short integration times (where read noise dominates in non-intensified detectors), or extremely deep observations (where dark current dominates in non-photon-counting detectors). Medical x-ray imaging and positron emission tomography applications could also benefit from this technology. Thus there are real benefits to developing detectors capable of operating at room temperature and having a high single-photon counting quantum efficiency with a tunable spectral response

in the UV/blue range. For this work, wide-band-gap GaN-based materials have been selected over the more commonly used GaAs system for several reasons. The band gap of GaN (3.4 eV) has excellent overlap with the UV/blue spectral region and can be epitaxially grown on optically transparent single-crystal sapphire substrates, which can serve as the window on transmission-mode photocathode devices. Also, the larger band gap provides much lower thermal noise, possibly allowing for uncooled room-temperature single-photon detection operation. In addition to selecting the nitride materials we make use of band-gap engineering principles to design photocathode device heterostructures, where semiconductor valence- and conduction-band-edge energy spatial profiles are tailored to optimize photoelectron absorption and transport to the surface.

II. EXPERIMENTAL METHOD

Our photocathode research involves the design and fabrication of precisely tailored heteroepitaxial semiconductor structures that have peak sensitivity in the UV/blue spectral range. A molecular-beam epitaxy (MBE) system dedicated to GaAlN/GaInN heterostructure growth was adapted to allow *in situ* quantum efficiency measurements to be made without having to remove freshly fabricated photocathodes from ultrahigh-vacuum (UHV) conditions. A connected UHV chamber incorporating the necessary wafer translators and

---
[a]Electronic mail: buckley@wuphys.wustl.edu

positioners was designed and built for this purpose. Also incorporated in this chamber is a UV/visible optical fiber probe and seven-element hybrid phototube housing, as well as a cesium-ion source for activation of photocathode surfaces. A photocathode wafer can be transferred from the growth chamber to a carousel for Cs activation in the sample introduction chamber. Thereafter, the carousel can be translated back and forth between the activation chamber and the quantum efficiency chamber. This system makes possible *in situ* measurements of quantum efficiency and spectral response without breaking the vacuum, providing the best feedback for optimizing wafer growth and surface activation.

The use of MBE for crystal growth makes it possible to control film composition on an atomic scale and to fabricate abrupt heteroepitaxial interfaces. The system for GaAlN/GaInN growth is equipped with a rf plasma source for nitrogen. An oil-free magnetic bearing turbomolecular pump is used for removing excess molecular nitrogen from the ultrahigh-vacuum chamber. Standard MBE Knudsen cell sources are used for Ga, Al, and In, as well as the Mg p-type dopant. An electron-beam source is available for Si n-type doping if needed, although undoped GaN is intrinsically n type. All of the AlGaN/GaInN heterostructures reported in these studies were grown on (0001)-oriented single-crystal sapphire substrates. While other substrates might provide better lattice matching, the mechanical strength and UV/visible optical transparency of sapphire make it a good choice as a window material for photocathode structures.

A reflection high-energy electron diffraction (RHEED) system mounted inside the MBE vacuum chamber allows the surface crystal quality to be monitored and individual atomic layers to be counted during growth as they are added to the surface one at a time by examining surface reconstruction diffraction patterns. The RHEED pattern is very sensitive to the ratio of Ga to N flux during growth. Ga-rich conditions lead to a highly streaked pattern while N-rich conditions produce a more spotted pattern. Too high of a Ga/N flux ratio can also lead to Ga precipitation on the surface. Overall, the best epitaxial layers are produced when the ratio of Ga to N flux is close to 1. Also, during all of our GaN epitaxial growth the substrate surface is exposed to an In flux to increase the surface diffusion of Ga.[1] The 720 °C substrate temperature used for GaN is high enough to assure that essentially no In is incorporated. However, we have found that indium can be intentionally incorporated in an InGaN alloy layer by lowering the substrate temperature to around 620 °C while simultaneously reducing the Ga flux. One concern surrounding the addition of In as an alloy component in the InGaN epitaxial layer involves additional strain due to the lattice mismatch between GaN and InN. Such alloying can also lead to elemental phase segregation in the epitaxial layer. This puts some constraints on the growth parameters for producing good epitaxial layers. However, in spite of these limits the MBE process appears to work with little problem up to the 10% In currently used in our heterostructures.

The photon conversion efficiency and spectral response of a photocathode structure are determined using differential measurements with respect to a calibrated absolute reference.

A monochromatic, pulsed light source has been installed on a small optical bench near the quantum efficiency chamber. The optical setup consists of a pulsed Xe flash lamp followed by a monochromator under computer control. A custom-made bifurcated fiber bundle consisting of 14 interleaved UV transparent fused-silica fibers is formatted onto the output slit of the monochromator to evenly split the light into two paths, each consisting of a close-packed bundle of seven fibers. One fiber bundle transmits light to a UV-enhanced silicon photodiode reference detector located in a shielded enclosure on the optical bench. The other branch of the fiber bundle goes to a focusing beam probe held by an XY positioner above a window of the vacuum chamber, where light is focused on one end of an unclad fused-silica fiber mounted inside the vacuum chamber. The vacuum chamber fiber is terminated with a small collimating lens that illuminates the photocathode surface.

An XYZ positioner built into the quantum efficiency chamber allows the photocathode to be coupled to an electron multiplier device, which is actually a windowless version of a hybrid photomultiplier tube (HPMT). In this configuration, the photocathode is positioned as the entrance window of the hybrid photomultiplier anode structure. A high-voltage feedthrough provides a bias between the photocathode and a segmented array of seven photodiodes. The photocathode wafer is mounted on a molybdenum plate and held with stainless steel clips at the edges. High-voltage electrical contact is made to the photocathode layer by biasing the entire platform, allowing current to flow through the metal clips to the photocathode surface and preventing the buildup of any space charge resulting from photoemission. Photoelectrons emitted by the cathode are typically accelerated toward the photodiodes to an energy of 5 keV, liberating $\sim$1000 electrons in the photodiode. In this proximity-focused device, the field is sufficiently large that the electrons travel in a direct straight-line path from the photocathode to the corresponding segment of the photodiode array. The arrangement of photodiodes is such that a single central pixel is surrounded by a guard ring of six hexagonal-close-packed detectors. The outer ring is used to measure the spillover of charge outside of the central pixel to verify the alignment of the electron optics. Signals from these photodiodes pass through a vacuum feedthrough to the external preamplifiers. HPMT's of this variety are ideally suited for quantum efficiency measurements. The gain is linearly dependent on the bias voltage, unlike the dynode chains of photomultiplier tubes. These devices also have the capability to provide excellent single photoelectron resolution that allows an absolute gain calibration by identifying, e.g., the one-, two-, and three-photoelectron peaks. Traditionally, quantum efficiency is measured by exposing a device to a calibrated UV light source and measuring the current. This method more easily introduces space-charge effects which can be especially problematic for large-area, higher-resistivity device structures. Moreover, this method cannot separately measure intrinsic gain and detection efficiency.

Signals from the reference silicon detector and the HPMT detector are read out with low-noise Amptek A250 preamplifiers, then pass through shaping amplifiers and are
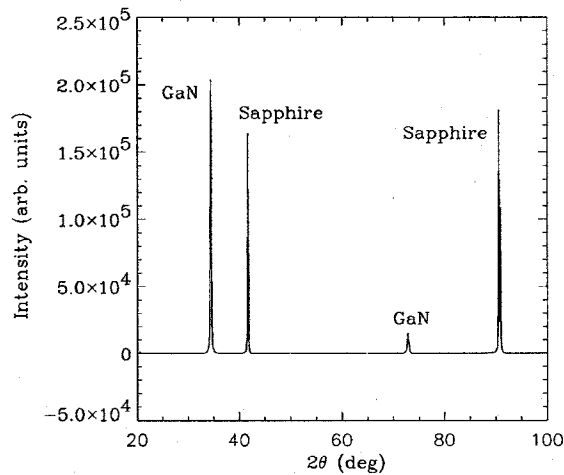
FIG. 1. X-ray-diffraction $\theta-2\theta$ scan of a GaN epitaxial layer grown by MBE on a sapphire substrate.

FIG. 2. Optical transmission as a function of wavelength for GaN and InGaN samples showing the band-gap shifting with higher In concentration.

digitized. A computer controls the light pulser, scans the monochromator, and simultaneously captures the wave forms from signals in the calibrated reference detector and from the photocathode/HPMT. The relative measurement corrects for drift and fluctuations in the light pulser. The system was calibrated for absolute measurements by placing a calibrated UV-enhanced photodiode (identical to the reference device) inside the vacuum chamber and performing a cross calibration. This procedure was used to renormalize the measurements in the reference arm to provide an absolute measurement of the number of photons per light pulse striking the photocathode. Thus, together with the HPMT gain, a complete absolute calibration of the system was obtained.

III. RESULTS

A series of atomically tailored GaN/InGaN photocathodes were fabricated on 2-inch diameter single-crystal sapphire wafer substrates. Experimental results on the structural, optical, and electronic properties of these epitaxial layers indicate reasonably high-quality material. X-ray diffraction and TEM lattice image studies show good registry of epitaxial GaN and InGaN layers with the c-plane-oriented, single-crystal sapphire substrates. A $\theta-2\theta$ x-ray-diffraction scan exhibiting GaN and sapphire substrate peaks is shown in Fig. 1. The full width at half maximum (FWHM) of the GaN (0002) x-ray peak is approximately 400 arc sec for the 0.5 -μm-thick film, indicative of high-quality epitaxial GaN considering the layer is thin and the substrate is sapphire. Figure 2 shows optical absorption measurements of GaN and two InGaN samples, confirming the expected band gap shift to longer wavelength with increasing In concentration. Although the band gap alone does not determine the total energy shift of the photoemission threshold, it is an important component along with the electron affinity of the material.

Another important component needed for the development of high quantum efficiency semiconductor photocathodes is the ability to achieve high p-type doping levels in the active layer. Typically Mg is used as the p-type dopant in GaN. It is difficult to obtain highly p-type GaN epitaxial
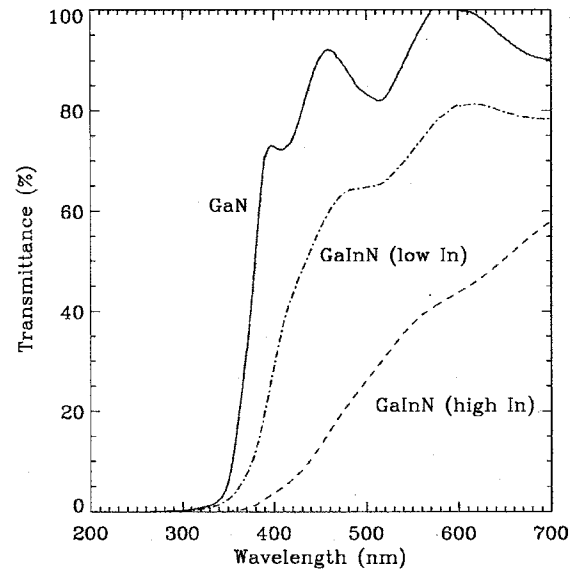
material in part due to the large intrinsic background n-type carrier concentration, as well as the large ionization energy of the Mg p-type acceptor level.[2] We had success with Mg by first reducing the n-type background. This was accomplished by growing under slightly N-rich conditions, and also by growing on the Ga face which is achieved by exposing the sapphire surface to a nitrogen plasma prior to growth.[3] Hall measurements, using the Van der Pauw technique, indicate p-type carrier concentrations up to 10^{18} cm^{-3}. This proved to be adequate for fabricating negative electron affinity (NEA) semiconducting photocathode layers after activating the surface with Cs.

A couple of key design features are incorporated in the heteroepitaxial photocathode layers to increase the quantum efficiency. An example of this is shown in Fig. 3, where conduction- and valence-band-edge energy spatial profiles are displayed for one of the photocathode designs. The diagram in Fig. 3 is a rough schematic plot of band gap versus
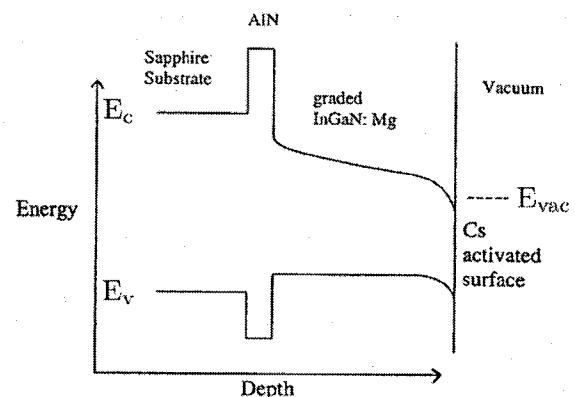

FIG. 3. Spatial profile of the conduction and valence band edges for a designed photocathode heterostructure showing an AlN barrier at the sapphire substrate interface, a graded GaN/InGaN region, and a Cs-activated surface.

depth into the photocathode structure. For purposes of clarity the thickness of the various layers are not drawn to scale. An AlN or AlGaN layer inserted between the sapphire and the GaN/GaInN photocathode region serves as a wide-band-gap barrier to prevent electronic back diffusion toward the substrate interface, where defect densities are expected to be higher and nonradiative recombination of photoexcited electrons larger. Inserting this wide band gap AlN or AlGaN buffer layer in the structure ensures that photoexcited electrons do not diffuse back toward the sapphire substrate interface, but rather are reflected toward the photocathode emission surface.

In our AlGaN/InGaN heterostructures the alloy composition in the photocathode region is graded to tailor the conduction- and valence-band profiles in a manner that will enhance photoelectron transport to the surface. An electric field induced by applying a voltage across a photocathode layer drives electrons toward the semiconductor surface/vacuum interface, and in so doing can increase the quantum efficiency by as much as a factor of 2.[4] This internal field can also be generated by grading the alloy composition, effectively tilting the conduction and valence band edges. An example of such alloy grading is shown in Fig. 3, where conduction- and valence-band-edge energy spatial profiles, E_c and E_v, are displayed for InGaN. The energy gap of GaN in the wurtzite crystal structure is 3.39 eV at room temperature.[5] The band gap can be continuously adjusted to lower energies by alloying with In. As the In content in the alloy layer increases the energy difference between the valence band and the conduction band decreases, resulting in a sloping of the band edges. Although the fractional change in the conduction and valence bands are different, the overall effect is to tilt the conduction band since the p-type dopant incorporated throughout the layer allows mobile hole charge carriers to diffuse in a manner that minimizes the energy, leaving the valence-band profile flat. The tilted conduction band is designed to drive photoelectrons toward the surface, increasing their escape probability and thus the quantum efficiency. Another reason for including the GaInN alloy layer is to extend the optical absorption to a longer wavelength to better match scintillator emission.[6] Finally, as shown in Fig. 3, an activation layer of Cs on the surface bends the bands to achieve a NEA condition, which is vital for having a high photoelectron escape probability.

AlGaN/GaN/GaInN:Mg photocathode surfaces have been activated with cesium. Figure 4 shows the recorded single-pulse output from an activated photocathode and from the reference detector obtained at 300 nm with our system. For this measurement the optical excitation pulse was attenuated by a factor of 100 using neutral density filters in both the reference detector and HPMT legs of the system. The measured photoelectron emission quantum efficiency spectral response for three different photocathodes is shown in Fig. 5. In each case the MBE-grown InGaN photocathode layers were graded to extend wavelength coverage into blue as well as to provide an internal field to drive photoelectrons toward the emitting surface. As seen in Fig. 5 the photocathode with a higher p-type doping ($\sim 10^{18}$ cm^{-3}) has a larger quantum efficiency (40% at 250 nm) throughout the mea-
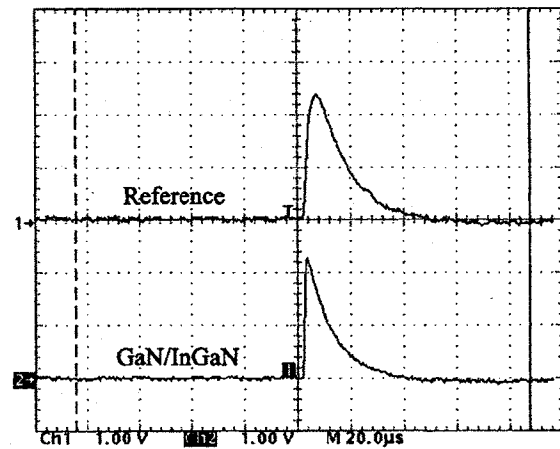

FIG. 4. *In situ* single-shot measurement of photoelectron emission from an MBE-grown GaN/InGaN photocathode compared to a reference detector in response to pulsed UV light excitation at 300 nm.

surement range. The sample with a lower doping ($\sim 10^{17}$ cm^{-3}) exhibits a slightly smaller quantum efficiency, consistent with earlier studies on GaN photocathodes and demonstrating the need for higher p-type doping.[7–9] The third set of quantum efficiency data displayed in Fig. 5 is from a photocathode that contains a thin AlGaN barrier layer at the substrate interface. No improvement over the highly doped GaN/InGaN photocathode was found, implying that the quantum efficiency is limited by crystalline defects contained in the active photocathode layer. In fact, in all three samples the falloff in quantum efficiency with increasing wavelength can be attributed primarily to crystal defects distributed throughout the epitaxial layers. Longer-wavelength optical photons have a smaller absorption coefficient, and thus a correspondingly larger penetration depth into the photocathode layer. The deeper optical penetration requires such photoelectrons to travel farther to reach the surface, making these charge carriers more likely to run into a defect where recombination can occur. Thus the quantum efficiency is range limited, controlled by the photoelectron mobility-lifetime product. The loss of photocarriers from this process results in a monotonic decrease in quantum efficiency with
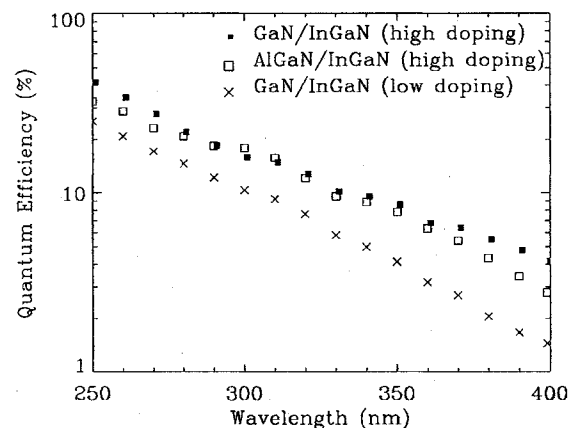

FIG. 5. Measured quantum efficiency for GaN/GaInN and AlGaN/GaN/InGaN photocathode heterostructures.

increasing wavelength as observed experimentally in Fig. 5. A thicker (0.5 μm) AlGaN buffer layer did not improve the overall quantum efficiency spectral response. Thus from the data displayed in Fig. 5 we can infer that the AlGaN buffer layer did not significantly alter the defect density in the active GaN and InGaN overgrown layers, since no appreciable difference was found between photocathodes with and without this layer.

IV. SUMMARY

The results presented demonstrate that a reasonably high quantum efficiency can be obtained from thin GaN/InGaN photocathode layers grown on sapphire substrates designed for transmission-mode detector devices. At the present time we have shown that the spectral response is primarily limited by defects in the epilayers. By varying other design parameters in these MBE-grown heterostructures we anticipate there is a potential for further improvement. Most importantly, photocathodes grown on other substrates such as single-crystal AlN wafers should result in an improvement by lowering the epitaxial layer defect density, since AlN provides a better lattice match to the GaN/GaInN layers. However, commercially available bulk AlN still exhibits some strong optical absorption in the UV-blue band from impurities or defects, making it impractical for transmission-mode photocathode devices at this time. If the epilayer defect density can be lowered the diffusion barrier would play a more important role toward enhancing the quantum efficiency spectral response by preventing photocarriers from reaching the substrate interface. Ultimately, further optimization of doping, alloy grading, and surface activation could then also be expected to enhance carrier transport and emission from the NEA surface resulting in an improved quantum efficiency.

[1]F. Widmann, B. Daudin, G. Feuillet, N. Pelekanos, and J. L. Rouviere, Appl. Phys. Lett. **73**, 2642 (1998).

[2]T. D. Moustakas and R. J. Molnar, Mater. Res. Soc. Symp. Proc. **281**, 753 (1993).

[3]L. K. Li, M. J. Jurkovic, W. I. Wang, J. M. V. Hove, and P. P. Chow, Appl. Phys. Lett. **76**, 1740 (2000).

[4]L. Guo, J. Li, and H. Xun, Semicond. Sci. Technol. **4**, 498 (1989).

[5]S. Strite, M. E. Lin, and H. Morkoc, Thin Solid Films **231**, 197 (1993).

[6]E. V. D. van Loef, P. Dorenbos, C. W. E. van Eijk, K. Kramer, and H. U. Gudel, Appl. Phys. Lett. **79**, 1573 (2001).

[7]M. P. Ulmer, B. W. Wessels, F. Shahedipour, R. Y. Korotkov, C. Joseph, and T. Nihashi, Proc. SPIE **4288**, 246 (2001).

[8]F. S. Shahedipour, M. P. Ulmer, B. W. Wessels, and C. L. J. T. Nihashi, IEEE J. Quantum Electron. **38**, 333 (2002).

[9]M. P. Ulmer, B. W. Wessels, and O. H. W. Siegmund, Proc. SPIE **4650**, 94 (2002).

Bibliography

Aharonian F., Akhperjanian A., Beilicke M., et al. ApJ, 614, 897, 2004.

Aharonian F., Akhperjanian A.G., Aye K.M., et al. A&A, 436, L17, 2005.

Aharonian F.A. New Astronomy, 5, 377, 2000.

Aharonian F.A. *Very high energy cosmic gamma radiation : a crucial window on the extreme Universe.* Very high energy cosmic gamma radiation : a crucial window on the extreme Universe, by F.A. Aharonian. River Edge, NJ: World Scientific Publishing, 2004, 2004.

Aharonian F.A., Akhperjanian A.G., Andronache M., et al. A&A, 350, 757, 1999.

Allen C.W. *Astrophysical quantities.* London: University of London, Athlone Press, —c1973, 3rd ed., 1973.

Aller H.D., Aller M.F., Latimer G.E., et al. ApJS, 59, 513, 1985.

Baars J.W.M., Genzel R., Pauliny-Toth I.I.K., et al. A&A, 61, 99, 1977.

Backus G.E. and Gilbert J.F. Royal Society of London Philosophical Transactions Series A, 266, 123, 1970.

Bednarek W. MNRAS, 285, 69, 1997.

Bednarek W. and Protheroe R. MNRAS, 310, 577, 1999.

Begelman M.C., Rees M.J., and Sikora M. ApJ, 429, L57, 1994.

Bernlohr K. http://www.mpi-hd.mpg.de/hfm/cosmicray/showers.html. WWW, 2005.

Blackett P. Phys. Abst, 34, 4347, 1949.

Blandford R.D. and Ostriker J.P. ApJL, 221, L29, 1978.

Blazejowski M., Blaylock G., Bond I.H., et al. ApJ, 630, 130, 2005.

Bottcher M., Mause H., and Schlickeiser R. A&A, 324, 395, 1997.

Buckley J.H. In S. Ritz, N. Gehrels, and C.R. Shrader, editors, *AIP Conf. Proc. 587: Gamma 2001: Gamma-Ray Astrophysics*, 235–+. 2001.

Buckley J.H., Akerlof C.W., Biller S., et al. ApJ, 472, L9+, 1996.

Chudakov A., Zatsepin V., Nesterova N., et al. J. Phys. Soc. Jpn., 17, no. A-III, 106, 1962.

Dingus B.L., Alexandreas D.E., Allen R.C., et al. Physical Review Letters, 61, 1906, 1988.

Drury L.O., Duffy P., Eichler D., et al. A&A, 347, 370, 1999.

Edelson R.A. and Krolik J.H. ApJ, 333, 646, 1988.

Fenimore E.E., Laros J.G., Klebesadel R.W., et al. In *AIP Conf. Proc. 77: Gamma Ray Transients and Related Astrophysical Phenomena*, 201–209. 1982.

Finley J.P., Badran H.M., Bond I.H., et al. In *International Cosmic Ray Conference*, 2827–+. 2001.

Fossati G., Celotti A., Chiaberge M., et al. ApJ, 541, 153, 2000.

Gaidos J.A., Akerlof C.W., Biller S.D., et al. Nature, 383, 319, 1996.

Galbraith W. and Jelley J. Nature, 171, 349, 1953.

Galbraith W. and Jelley J. J. Atmos. Terr. Phys, 6, 250, 1955.

Georganopoulos M. and Kazanas D. ApJ, 594, L27, 2003.

Ghisellini G., Tavecchio F., and Chiaberge M. A&A, 432, 401, 2005.

Gorham P.W., Cawley M.F., Fegan D.J., et al. ApJ, 309, 114, 1986.

Hartman R.C., Bertsch D.L., Bloom S.D., et al. ApJS, 123, 79, 1999.

Hartman R.C., Bertsch D.L., Fichtel C.E., et al. ApJ, 385, L1, 1992.

Hillas A.M. In *International Cosmic Ray Conference*, 445–448. 1985.

Hillas A.M., Akerlof C.W., Biller S.D., et al. ApJ, 503, 744, 1998.

Hinton J.A. New Astronomy Review, 48, 331, 2004.

Horan D. and Weekes T.C. New Astronomy Review, 48, 527, 2004.

Impey C. AJ, 112, 2667, 1996.

Inoue S. and Takahara F. ApJ, 463, 555, 1996.

Jackson J. *Classical Electrodynamics*. Wiley, 3rd edition, 1998.

Jahoda K., Swank J., Giles A., et al. In *Proc. SPIE Vol. 2808, p. 59-70, EUV, X-Ray, and Gamma-Ray Instrumentation for Astronomy VII, Oswald H. Siegmund; Mark A. Gummin; Eds.*, 59–70. 1996.

Jordan M. and The VERITAS Collaboration. In *International Cosmic Ray Conference*, 2691–+. 2001.

Kataoka J., Takahashi T., Makino F., et al. ApJ, 528, 243, 2000.

Kertzman M. and Sembroski G. Nucl. Instrum. Methods Phys. Res., A343, 629, 1994.

Kinney A.L., Schmitt H.R., Clarke C.J., et al. ApJ, 537, 152, 2000.

Kino M., Takahara F., and Kusunose M. ApJ, 564, 97, 2002.

Kirk J.G. and Mastichiadis A. Astroparticle Phys., 11, 45, 1999.

Kneiske T.M., Mannheim K., and Hartmann D.H. A&A, 386, 1, 2002.

Konopelko A., Mastichiadis A., Kirk J., et al. ApJ, 597, 851, 2003.

Kosack K. *Very High Energy Gamma Rays from the Galactic Center*. Ph.D. thesis, Washington University, 2005.

Kosack K., Badran H.M., Bond I.H., et al. ApJ, 608, L97, 2004.

Krawczynski H. New Astronomy Review, 48, 367, 2004.

Krawczynski H., Coppi P., Maccarone T., et al. A&A, 353, 97, 2000.

Krawczynski H., Coppi P.S., and Aharonian F. MNRAS, 336, 721, 2002.

Krawczynski H., Hughes S.B., Horan D., et al. ApJ, 601, 151, 2004.

Krawczynski H., Sambruna R., and Kohnle A. ApJ, 559, 187, 2001.

Krennrich F., Biller S.D., Bond I.H., et al. ApJ, 511, 149, 1999.

Kubo H., Asahara A., Bicknell G.V., et al. New Astronomy Review, 48, 323, 2004.

Leopold D., Buckley J., and P. R. J. Appl. Phys., 98, 043525, 2005.

Levine A.M., Bradt H., Cui W., et al. ApJ, 469, L33+, 1996.

Li T.P. and Ma Y.Q. ApJ, 272, 317, 1983.

Lloyd-Evans J., Coy R.N., Lambert A., et al. Nature, 305, 784, 1983.

Longair M. *High Energy Astrophysics*, volume 1. Cambridge Press, 2nd edition, 1992.

Loredo T.J. and Epstein R.I. ApJ, 336, 896, 1989.

Mücke A., Protheroe R.J., Engel R., et al. Astroparticle Phys., 18, 593, 2003.

Mannheim K. Science, 279, 684, 1998.

Maraschi L., Fossati G., Tavecchio F., et al. ApJ, 526, L81, 1999.

Mastichiadis A. and Kirk J. A&A, 320, 19, 1997.

Mirzoyan R., Kankanian R., Krennrich F., et al. Nuclear Instruments and Methods in Physics Research A, 351, 513, 1994.

Mirzoyan R.e. Nucl. Instrum. Methods Phys. Res., A351, 513, 1994.

Petry D., Bond I.H., Bradbury S.M., et al. ApJ, 580, 104, 2002.

Piner B.G. and Edwards P.G. ApJ, 622, 168, 2005.

Pohl M. and Schlickeiser R. A&A, 354, 395, 2000.

Press W.H., Teukolsky S.A., Vetterling W.T., et al. *Numerical recipes in C. The art of scientific computing*. Cambridge: University Press, —c1992, 2nd ed., 1992.

Protheroe R.J. and Stanev T. Astroparticle Physics, 10, 185, 1999.

Punch M., Akerlof C.W., Cawley M.F., et al. Nature, 358, 477, 1992.

Punch M. and Fegan D.J. In *AIP Conf. Proc. 220: High Energy Gamma Ray Astronomy*, 321–328. 1991.

Ramana Murthy P. and Wolfendale A. *Gamma-ray Astronomy*. Cambridge Press, 1st edition, 1986.

Rauterberg G. In *International Cosmic Ray Conference*, 460. 1995.

Rebillot P.F., Badran H., Blaylock G., et al. ApJ, 541, 74, 2006.

Reynolds P.T., Akerlof C.W., Cawley M.F., et al. ApJ, 404, 206, 1993.

Rohlfs K. and Wilson T. *Tools of Radio Astronomy*. Springer, 4th edition, 2004.

Rothchild R., Blanco P., Gruber D., et al. ApJ, 496, 538, 198.

Rybicki G. and Lightman A. *Radiative Processes in Astrophysics*. Wiley, 1979.

Samorski M. and Stamm W. ApJL, 268, L17, 1983.

Takahashi T., Tashiro M., Madejski G., et al. ApJ, 470, L89, 1996.

Tanihata C., Urry C., and Takahashi T. ApJ, 563, 569, 2001.

Tavecchio F. In *Proceedings of the 10th Marcel Grossman Meeting on General Relativity*. in press.

Tavecchio F., Maraschi L., and Ghisellini G. ApJ, 509, 608, 1998.

Turver K.E. and Weekes T.C. Royal Society of London Philosophical Transactions Series A, 301, 615, 1981.

Urry C. In *ASP Conf. Ser. 311: AGN Physics with the Sloan Digital Sky Survey*, 49–+. 2004.

Veilleux S. In *ASP Conf. Ser. 290: Active Galactic Nuclei: From Central Engine to Host Galaxy*, 11–+. 2003.

Villata M., Raiteri C.M., Lanteri L., et al. A&AS, 130, 305, 1998.

Weekes T. *Very High Energy Gamma-Ray Astronomy*. IoP, 1st edition, 2003.

Weekes T.C. Space Sci. Rev., 59, 315, 1992.

Weekes T.C. Space Sci. Rev., 75, 1, 1996.

Weekes T.C., Badran H., Biller S.D., et al. Astroparticle Physics, 17, 221, 2002.

Zweerink J.A., Akerlof C.W., Biller S.D., et al. ApJ, 490, L141, 1997.